Electronic Structure, Bonding and Reactivity of Zintl Clusters

Sourav Mondal
New College
University of Oxford

A thesis submitted for the degree of
Doctor of Philosophy

Michaelmas 2024

To my parents.

Acknowledgements

First and foremost, I would like to express my deepest gratitude to my supervisor, Professor John E. McGrady, whose unwavering guidance, insightful feedback, and constant support have been priceless throughout my DPhil journey. His expertise, knowledge, and encouragement have inspired me greatly, and I am sincerely grateful. The chitchat about cricket and Indian culture will be remembered.

I am thankful to Prof. Gopalan Rajaraman and his group who introduced computational chemistry to me and motivated me constantly.

I am so grateful to my family and friends for their constant support, love and belief. To my parents, thank you for your unconditional support, both emotionally and practically, throughout my academic journey. I am deeply grateful for your sacrifices, encouragement, and understanding.

My gratitude to the Ministry of Social Justice and Empowerment, Government of India for providing me with the scholarship (National Overseas Scholarship) to study abroad. Without this scholarship, I would not be able to fulfil my dreams.

I am so thankful to all the group members for their help and support, special thanks to Yao Zhao for sharing knowledge and helping me with projects and set-ups, Jahanzaib Nowsherwan for friendly arguments and new college lads for nice formal dinners and events.

A round of applause to my friends; Desi gang: Govind Gour, Naganand Sarvanan, Alok Singh and the group for being a constant support and never letting me feel away from home. Bengali boys: Souvik Giri, Riju Dey and Sujay Saha for all the special moments, cooking together, fun trips. Childhood friends: Dibyendu Das, Sanjay Das and Rima Samanta for always being on my side.

List of Publications

1. **Sourav Mondal**, Wei-Xing Chen, Zhong-Ming Sun, and John E. McGrady. Synthesis, structure and bonding in pentagonal bipyramidal cluster compounds containing a cyclo-Sn5 ring, $[(CO)_3MSn_5M(CO)_3]^{4-}$ (M = Cr, Mo). ***Inorganics***, 10(6), 75 (2022).[1]

2. Ya-Nan Yang, Zi-Sheng Li, **Sourav Mondal**, Lei Qiao, Cui-Cui Wang, Wen-Juan Tian, Zhong-Ming Sun, John E. McGrady. Metal-metal bonds in Zintl clusters: Synthesis, structure and bonding in $[Fe_2Sn_4Bi_8]^{3-}$ and $[Cr_2Sb_{12}]^{3-}$. ***Chinese Chemical Letters***, 35(8), 109048 (2024).[2]

Abstract

This thesis presents two aspects of computational studies on the endohedral transition metal-based Zintl clusters, polyanionic clusters formed by p-block metal/metalloid in combination with alkali or alkaline earth metals. The first focuses mainly on the fundamental questions of electronic structure, metal-metal bonding and geometry in Sn-containing Zintl ions. We consider how the interactions between the Sn and the transition metal vary as a function of metal and also of composition of the cage, and probe the interplay of metal-metal, metal-Sn and Sn-Sn bonding. The late transition metals typically have relatively inert d^{10} cores, and interactions with the cage are minimal. However, as the d orbitals become higher in energy in the middle of the periodic table, back-bonding causes a weakening and then, ultimately, cleavage of some of the Sn-Sn bonds in the cluster. All the work reported in this first aspect has been done in collaboration with experimental colleagues from Professor Zhong-Ming Sun's group at Nankai University in China.

The second component of the thesis is a study of the potential role of these endohedral clusters in catalysis. The $[Ru@Sn_9]^{6-}$ cluster has been shown to be an active catalyst for the reverse water-gas shift (rWGS) reaction when supported on CeO_2, but details of the exact structure of the supported species, or the mechanism, remain uncertain. The cluster appears not to survive intact on absorption - instead, it forms a $RuSn_9$ monolayer, maximising the number of Sn-O and Ru-O bonds. The junction between the Ru and Sn atoms in the monolayer proves to be highly oxophilic, and oxide ions in these bridging sites can be transferred to the bound CO in a low-barrier step, leading to effective catalysis. It seems, therefore, that the composition of the cluster is more important than its geometry in the context of catalysis.

Contents

List of Figures

Chapter 1

Introduction

This thesis describes a series of computational studies into Sn-containing Zintl ions. The precise composition of the clusters varies, but the common feature of all of them is the presence of tin atoms. A diverse family of these clusters has been synthesised over the years, and the relative abundance of the element makes it an attractive proposition for applications such as catalysis. The thesis is divided up into two distinct components. In Chapter 3, I will describe how I have used theory (primarily DFT) to explore the electronic structure of Zintl ions containing endohedral transition metals. Here endohedral refers to clusters where smaller atom(s) or molecule(s) are enclosed within a larger polyhedron. The emphasis here is on fundamental electronic structure, on relating structure to electron count, and understanding what the role of the transition metal is in stabilising the cluster. At one extreme, the metal may be electronically inert, simply filling a void in the main-group cluster, and at the other it may be engaged in covalent bonding to the atoms of the cage: understanding how the role of the metal varies across the periodic table is central to understanding the diverse structural chemistry that we observe. Chapter 3 is further divided into three separate case studies, all of which have been performed in collaboration with colleagues based in the research group of Professor Zhong-Ming Sun at Nankai University in Tianjin, China. Two of the case studies have been published as joint works and have reported the synthesis, spectroscopy, X-ray diffraction and bonding. In all cases, the synthesis, spectroscopy and structural work were done by others, my own contribution being the computational component. The specific contributions of co-workers are stated at the beginning of each sub-chapter. The second main results chapter (Chapter 4) discusses the possible role of Zintl clusters, and specifically a Ru-based cluster, $[Ru@Sn_9]^{6-}$ in catalysing the water-gas shift (WGS) and CO methanation reactions. This is again based on work done by the Nankai group, but the experimental work has been published separately in ACS Catalysis.[3]

This first introductory chapter provides a short review of the general field of cluster chemistry and the tools that have been used to interpret electronic structure in this context. Most important amongst these are the various electron-counting rules such as the Wade-Mingos rules, Jemmis' rules, and the Zintl-Klemm concept that have emerged over the years to relate structure to electron count. I will then present a brief overview of the use of clusters in catalysis. Detailed reviews of the relevant literature will then be presented at the start of each chapter.

1.1 Zintl Clusters

The exploration of Zintl phases and Zintl clusters over the past century has led to some fascinating developments in inorganic and materials chemistry. These classes of compounds have been identified as having unique structures, bonding, and electronic properties which have very often challenged conventional bonding models. Zintl phases, first described by the German chemist Eduard Zintl in the 1930s, are a class of solid-state compounds that typically contain a combination of alkali and alkaline earth metals with p-block elements. These phases are remarkable in their ability to form electrides or electron-rich anionic structures wherein the metal cations donate electrons to stabilise the p-block metal/metalloid clusters' structure. A classic example of Zintl phase is Na_4Pb_9 which was first reported by Zintl et al.[4] but the structure (Figure 1.1(b)) was only confirmed much later, in the 1970s, by Kummer et al.[5] using X-ray crystallography. Isolated polyanions can be extracted from the Zintl phases using crown ethers or cryptands to stabilise the alkali metal cation, and these small clusters are typically referred to as 'Zintl clusters' or 'Zintl ions'. The structures of these clusters can be described using electron counting rules that are familiar from the work of Wade, Mingos and others on boranes. Examples of homoatomic and heteroatomic Zintl clusters include $[P_4]^{2-}$, $[Si_4]^{4-}$, $[In_4]^{-}$, $[In_4Bi_5]^{3-}$, $[Sb@In_8Sb_{12}]^{3-}$ etc.[6–9] In this thesis, I will be mainly focusing on group 14 Zintl clusters, and specifically those that contain an encapsulated transition metal.

1.1.1 Group 14 Zintl Clusters

The homoatomic group 14 deltahedral Zintl clusters (polyhedral clusters with triangular faces, Δ) have general formula $[E_n]^{q-}$, where n is the number of vertices ($n = 4, 5, 9, 10, 12$) and q is the charge on the cluster, ranging between 2-4. The structures of representative clusters are shown in Figure 1.1. The smallest member

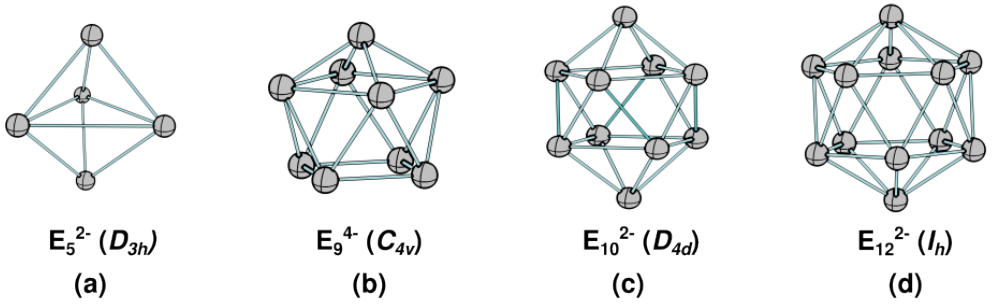

Figure 1.1: Deltahedral structures of group 14 (Ge, Sn, Pb) clusters $[E_n]^{q-}$ (n=5, 9, 10, 12 and q = 2, 3, 4).

of this family, tetrahedral $[E_4]^{4-}$, is found in the A_4E_4 (E= Si-Pb; A= Na-Cs) Zintl phases.[10,11] The clusters are isoelectronic to P_4.

The $[E_5]^{2-}$ clusters are D_{3h} symmetric trigonal bipyramids which can be extracted from Zintl phases with a higher proportion of the main-group element, E, than the 1:1 ratio found in A_4E_4. For example, $[Si_5]^{2-}$ anion was extracted from the $Rb_{12}Si_{17}$ phase.[12] Wade's electron counting rules (*vide infra*) predict that the 12 skeletal electrons should lead to a *closo* geometry. $[Ge_5]^{2-}$ is unique in the sense that it acts as a nucleophile through the lone pairs without a significant change in the structure.[13]

The 9-vertex $[E_9]^{x-}$ clusters are particularly interesting because the charge on the cluster can vary from 2- to 4-, leading to distinct changes in geometry and symmetry. For example, the *closo* dianion $[E_9]^{2-}$ (E = Si, Ge)[14,15] has a D_{3h} symmetric tricapped trigonal prismatic geometry while the 2-electron reduced analogues $[E_9]^{4-}$ preferentially adopt a C_{4v}-symmetric *nido*-monocapped square antiprismatic structure.[16] The paramagnetic $[E_9]^{3-}$ ion, with 21 skeletal electrons, falls between the D_{3h} and C_{4v} limits. The difference between C_{4v} and D_{3h} geometries is rather subtle, and so it is perhaps unsurprising that the two isomers are often close in energy. Sevov et al. proposed that all 3 different charge states of $[E_9]^{q-}$ (q = 2, 3, 4) can be in equilibrium in solution.[17] These 9-vertex clusters are sufficiently robust to be used as molecular building blocks for oligomers, polymers and mesoporous solid phases. The majority of studies of the $[E_{10}]^{2-}$ family have been conducted on Pb and Ge,[18,19] and only a few 10-vertex Sn_{10} clusters[20] have been reported to date, typically stabilised either by ligands or by encapsulated atoms. The most common structure is a D_{4d}-symmetric bicapped square antiprism with 22 skeletal electrons.

Finally, the most symmetric of the Zintl clusters is the 12-vertex icosahedral family, $[E_{12}]^{2-}$. Icosahedral $[Sn_{12}]^{2-}$ ("stannaspherene")[21] and $[Pb_{12}]^{2-}$ ("plumbaspherene")[22] have been reported in the gas phase, but $[Ge_{12}]^{2-}$ has not been isolated.

A computational study reveals that the I_h symmetric structure of $[Ge_{12}]^{2-}$ is in fact less stable than a C_{2v} symmetric *arachno*- tetra-capped cube.[23] The preference of this alternative structure in Ge is probably related to variations in *sp* hybridisation which favour localisation of *s* character in the lone pair in the heavier atoms. The major focus of this thesis is the incorporation of transition metal(s) into the clusters. In the next section, we will briefly discuss the developments and research that have been done in the field of TM-Zintl clusters.

1.1.2 Structure and Electron Counting Rules for Clusters

A number of different models have been developed that relate the structure of metal clusters to their valence electron count, perhaps the best known of which is the polyhedral skeleton electron pair theory (PSEPT), often known as 'Wade's rules'.[24] Kenneth Wade first formulated these electronic counting rules in the context of main-group clusters (boranes) and a further extension to transition-metal based clusters was done by Michael Mingos; the rules are known as Wade-Mingos rules.[25–27] The structures of boranes (B_nH_m) have fascinated chemists since their discovery by the German chemist Alfred Stock in the early 20^{th} century,[28] and another giant in the field, William Nunn Lipscomb, was awarded the Nobel Prize in 1976 for his studies on their structure. Furthermore, H.C. Brown shared the Nobel Prize in 1979 for synthetic work in organic chemistry utilising boranes:[29] back-to-back Nobel prizes in the same field highlight the importance of borane chemistry from the perspective of structure, chemical bonding, and applications.

The simplest borane is diborane B_2H_6, the bonding in which has been extensively studied for almost a century. B_2H_6 is also one of the most synthetically useful chemical intermediates, providing a precursor to many heavier boranes.[28,30] B_2H_6 is a classic example of a compound featuring a 3 centre- 2 electrons (3c-2e) bond, sometimes called a banana bond. The molecular orbital arrangement that leads to the stabilisation of B_2H_6 is illustrated in Figure 1.2: the two sp^3 hybridised BH_2 units overlap with the H *s* orbital.

An extensive family of larger borane compounds with n≤12 boron atoms at the vertices is also known, the general structural motif being based on polyhedra with triangular faces, often called deltahedra. These can, in turn, be categorised based on the number of missing vertices of the polyhedron. The IUPAC definition of boranes shown in Figure 1.3 identifies several different sub-classes: (i) *closo* - deltahedra of *n* boron atoms at *n* vertices; (ii) *nido* - *n*B atoms occupy *n* the vertices of an (n+1)-vertices polyhedron i.e., a *closo*-polyhedron with one missing vertex; (iii) *arachno* -

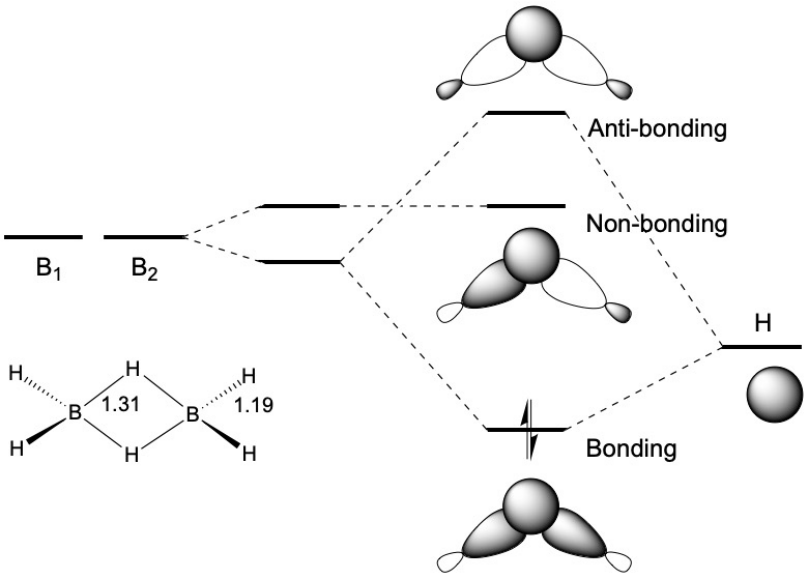

Figure 1.2: MO plot of a 3c-2e B-H-B bond. The low bond order (0.5) of the B-H bond length in the 3c-2e bond elongates the bond relative to the terminal analogue.

an $n+2$-vertex cluster with two vertices missing; (iv) *hypo-* and *klado-* are even more open clusters with $n+3$ and $n+4$ missing vertices respectively.

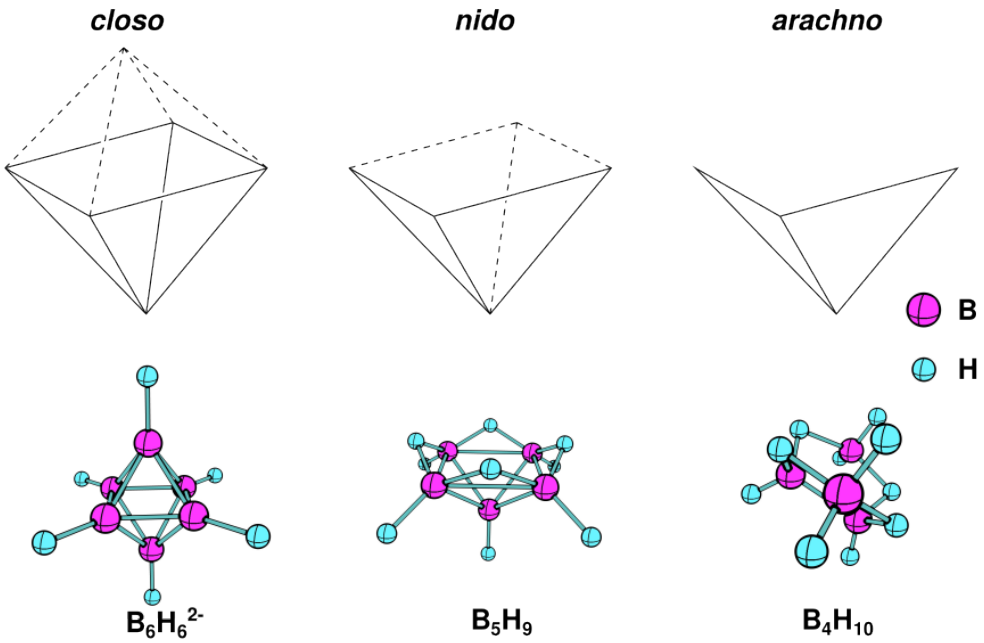

Figure 1.3: Structure of boranes with different numbers of vertices (n).

The Wade-Mingos rules are based on the number of skeletal electron pairs (SEP) available for bonding in the cluster. The SEP count can be calculated as follows:

1. Calculate the total valence electrons count (TVEC) from the chemical formula of the cluster.

2. Subtract 2 electrons for each B-H unit.

3. Divide the remaining number of electrons by 2 to get the number of SEPs.

4. The shape of the cluster is determined by the number of vertices (n) and the available SEPs are below:

   - $(n+1)$ - *closo*
   - $(n+2)$ - *nido*
   - $(n+3)$ - *arachno*
   - $(n+4)$ - *hypo*

For example, B_5H_9 consists of 24 TVEC and 5 B-H units, giving a SEP count of 7, two more than the vertex count of 5, so the cluster has a *nido*- structure (n+2). If a closed-shell (d^{10}) transition metal is present in the cluster, 10 electrons are subtracted from the total electron count. Jemmis has extended Wade's method to condensed polyhedral boranes where a large cluster is formed by the fusion of small subclusters through sharing a triangular face, an edge, a single vertex, or four vertices.[31,32] This electron counting method is called the 'mno' rules, which are invaluable in relating polyhedral boranes, condensed polyhedral boranes and β-rombohedral boron. The rule states that a macro-polyhedral system is stable when it has $m+n+o$ electron pairs where m is the number of polyhedra, n is the number of vertices and o is the number of condensed polyhedra that share only a single common atom. Wade's rule is a special case where $m=1$ and $n=0$. The relationships between clusters revealed by the mno rules are, in many ways, similar to the relationship between benzene, condensed benzenoid aromatics and graphite revealed by Hückel's $4n+2$ rule.[33,34]

The Wade-Mingos and Jemmis rules can be rationalised using frontier orbital theory, and are not restricted to boranes. Fragments, isolobal with the BH unit can replace the corners and a range of different types of clusters can be produced. For instance, the CH^+ fragment is isolobal with BH, and so the same set of rules can be applied to carboranes like $C_2B_4H_6$.[35] A BH or $M(CO)_3$ unit (M = Fe, Ru, Os) is also isoelectronic with group 14 elements (Sn, Pd), which is why the counting rules also apply to many Zintl clusters like *closo*-Pb_{12}^{2-},[22] and metal carbonyls such as *closo*-$[Os_6(CO)_{18}]^{2-}$.[36] For example, in case of Pb_{12}^{2-} Zintl cluster, the TVEC is $12\times4+2 = 50$ and has 12 Pb ($\equiv$ B-H) units, each Pb ($\equiv$ B-H) units consisting a lone pair which

are not involved in skeletal electron count, giving a SEP count of $(50-12\times2)/2 = 13$, one more than the vertex count of 12, so the cluster has a *closo-* structure (n+1), with icosahedral symmetry.

1.1.3 Transition-metal Encapsulation in Group 14 Zintl Clusters

Transition metal doping in the heavier group 14 Zintl clusters (tetrels) is now a well-established phenomenon. Ligand-free group 14 Zintl clusters with incorporated transition metals have the general formula of $[M@E_n]^{q-}$ (M = Si, Ge, Sn, Pb), and are known as endohedral Zintl ions and/or inter-metalloid clusters. The encapsulated metals are usually from the right side of the d-block series and the clusters contain the heavier (Ge, Sn, Pd) elements of the group because of the larger cavity of the cage. The most common way to synthesise endohedral Zintl clusters is to react an empty cage-cluster precursor, $[E_n]^{q-}$, with a low-valent organometallic complex. The transition metal will then either be encapsulated inside the cage, or added to the outside, increasing the number of vertices by one.

To date, the maximum number of vertices for monometallic endohedral clusters is 12. Some examples of 9-vertex clusters are $[Cu@E_9]^{3-}$ (E = Sn, Pb),[37] $[M@Sn_9]^{4-}$ (M = Co, Ni)[17,38] and $[Ni@E_9]^{3-}$ (E = Ge, Sn). Like empty E_9 clusters, the monometallic $M@E_9$ are highly flexible with a geometry somewhere between tri-capped trigonal prismatic (D_{3h}) and mono-capped square antiprismatic (C_{4v}). The $[Cu@E_9]^{4-}$ (E = Sn, Pb) cluster has almost perfect D_{3h} symmetry, but the nickel analogue $[Ni@Sn_9]^{4-}$ cluster[17] is slightly distorted from (C_{4v}) symmetry. These endohedrally filled clusters can act as ligands to transition metal atoms to form metal-centered and -capped species, known as "Rodolph's complexes". For example, $[Ni@Ge_9(NiL)]^{x-}$ (L = CO, C≡C-Ph, en), $[Pt@Sn_9Pt(PPh_3)]^{2-}$, $[Ni@Sn_9Ni(CO)]^{3-}$ etc.[39] All of these structures are well-described as neutral d^{10} transition metal atoms encapsulated within a ${E_9}^{4-}$ cage. The $[Ni@Sn_9]^{4-}$ system shows remarkably flexible redox activity between 3-/4- charge states. A very recent addition to this family, the $[Ru@Sn_9]^{6-}$ cluster, has been reported by Fässler and co-workers, and has been used as a CO_2 reduction catalyst on CeO_2 support. This cluster will be the focus of the work described in Chapter 4.

Like their empty counterparts, 10-vertex endohedral clusters commonly adopt bi-capped square antiprismatic deltahedral structures, as for example in $[Ni@Pb_{10}]^{2-}$, but non-deltahedral pentagonal prismatic structures are also found in $[M@Ge_{10}]^{3-}$ (M = Co, Fe).[40–42] The C_{2v} symmetric $[Fe@Sn_{10}]^{3-}$, can be viewed as an intermediate between these two limits.[43] DFT studies reveal that the Ni^0 (d^{10}) remain inert and that

the negative charge is localised on the cage in the case of $[Ni@Pb_{10}]^{2-}$,[44,45] whereas, significant Co-Ge bonding is present in D_{5h}-symmetric $[Co@Ge_{10}]^{3-}$. Ligand-free 12-vertex Zintl clusters can also adopt different structures, depending on the identity of the transition metal, the main group element and the charge of the system. Icosahedra dominate for heavier elements of group 14 (Sn, Pb) and for transition metals from the right-hand side elements of the d block. Examples of icosahedral $[M@E_{12}]^{q-}$ include M = Rh, Ir: E = Sn, q = 3; M = Ni, Pd, Pt: E = Pb: q = 2; M = Co, Rh, Ir: E = Pb: q=3.[17,45–49] All of the above can be viewed as containing a d^{10} atom/ion inside a $E_{12}{}^{2-}$ cage, and the cages are almost perfectly icosahedral. In other cases, however, the icosahedron can be strongly distorted. For example, $[Mn@Pb_{12}]^{3-}$ is elongated along one 2-fold axis, leading to D_{2h} point symmetry,[50] while $[Au@Pb_{12}]^{3-}$ is elongated along a 3-fold axis to a quasi-D_{3d} symmetry.[51,52] DFT studies show that in both cases there is significant charge transfer to the cage, which is more reduced than the 2- charge state characteristic of a *closo* geometry. Even when the cage is formally in the 2- charge state, distortions can occur if the metal is particularly electron-rich, as for example in $[Co@Ge_{12}]^{3-}$ (D_{5d}) and $[Rh@Sn_{12}]^{3-}$, which crystallises in two isomeric forms, one icosahedral and one slightly distorted to D_{3d} symmetric structure.[48] In the first part of Chapter 3, we will explore the origins of these distortions in the context of a newly synthesised cluster, $[Ru@Sn_{12}]^{4-}$. In that context, it is noteworthy that the closely related $[Ru@Ge_{12}]^{3-}$ cluster reported by Goicoechea and co-workers[53] adopts a completely different non-deltahedral 'fullerene-like' D_{2d}-symmetric structure: we have previously argued that this reflects string back-bonding from the metal to the cage. An additional isomeric form of the 12-vertex cage is the hexagonal prism with D_{6h} symmetry. This has not yet been reported in the crystalline phase, but there is compelling evidence that this structure is the stable form of silicon clusters like $[Cr@Si_{12}]$ and $[Mn@Si_{12}]^{+}$.[54–56] Finally, we note a different structural motif wherein the 12-vertex cage adopts a structure based on two square antiprisms stacked on top of each other: this motif can encapsulate either one two metals inside the cage(s), as shown in Figure 1.4(b). Some examples are $[Ni_2@Sn_7Sb_5]^{3-}$, $[Ni_2@Pb_7Bi_5]^{3-}$, $[Co_2@Sn_6Sb_6]^{3-}$ etc.[57–59] We will discuss new clusters of this type, $[Fe_2@Sn_4Bi_8]^{3-}$ and $[Cr_2@Sb_{12}]^{3-}$, in the second section of Chapter 3.[2]

The monomeric E_{12} cages discussed in the previous paragraph can accommodate a single (or a maximum of two in triple-decker architecture) transition metal. A number of recent studies have been devoted to encapsulating more metal atoms in the cage, which naturally demands an increase in the nuclearity of the main-group component. The fusion of deltahedral cages is one possible route to a larger cluster

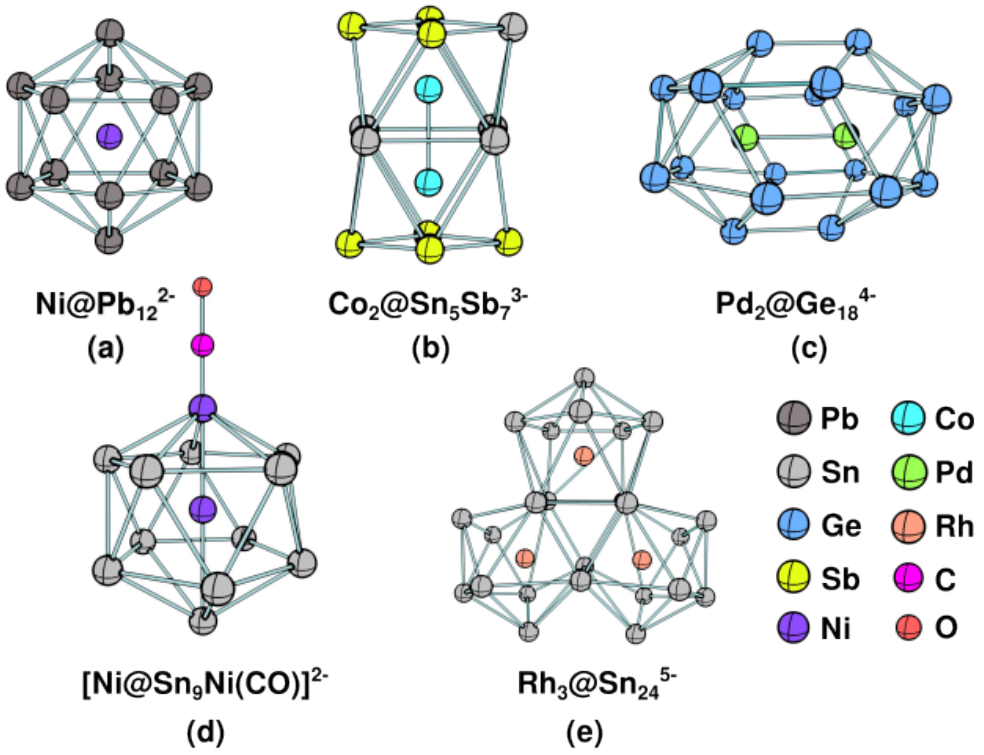

Figure 1.4: Endohedral Zintl clusters containing one or two transition metal ions.

and there is a clear analogy to the conjugation of several borane units to form a bigger cage, as set out in Jemmis' mno rules. This can be done by sharing a single vertex such as $[M_2Sn_{17}]^{q-}$ where, M= Ni, Pt: q=4; M= Co: q=5,[60,61] sharing edges as in $[Rh_3Sn_{24}]^{5-}$,[48] or complete polyhedral fusion to form a continuous large cage such as in $[Pd_2Ge_{18}]^{4-}$.[62] The important question here is whether any direct interactions are present between the metal ions. Structural parameters (M-M bond lengths) are not always the best index of the presence of bonding, simply because the positions of the metal ions are tightly constrained by the structures of the main-group cage. The presence or absence of metal-metal bonds is the central question that we address in sections 2 and 3 of Chapter 3.

The ambiguous role of the endohedral metal in these clusters will be emphasised throughout in Chapter 3. At one extreme, the metal may simply be a closed-shell ion (d^0 or d^{10}), filling the endohedral cavity without forming covalent bonds to the atoms of the E_{12} shell. At the opposite limit, mixing the d orbitals of the metal with those of the shell may lead to strong covalent bonding, with implications for structure and reactivity. The varying role of the metal d orbitals is a common thread that links the various chapters of this thesis. The key characteristics of transition

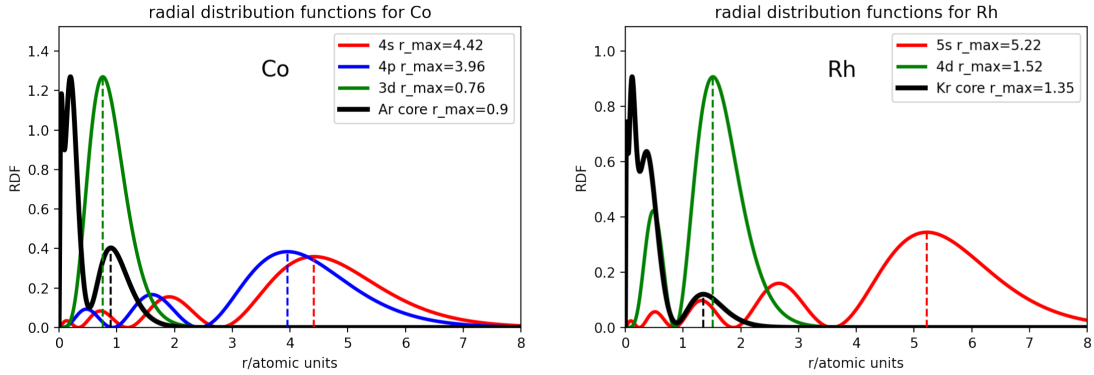

Figure 1.5: Radial distribution functions for the core and valence orbitals of Co and Rh.

metals which make them unique and versatile are (i) variable oxidation states (ii) formation of coordination compounds, with implications for spin state, spectroscopy and magnetism (iii) metallic bonding between d orbitals. The flexible oxidation state displayed by transition metal ions is particularly relevant to catalysis, and they are of vital importance in metalloenzymes. The electronic structure of the transition metals does, however, present a very substantial challenge to theory. The reason for this is that the nd electrons experience very strong repulsions from other nd electrons, but also from the ns- and np-'semi-core' electrons, which are more stable but have their radial maxima in the same region of space (see Figure 1.5). Particularly for the first-row metals, where the $3d$ orbital lacks radial nodes, the $d-d$ repulsion is extreme, placing a high premium on an accurate treatment of exchange and correlation effects. For the heavier transition metals, relativistic effects also become important, leading to the strong contraction of inner s orbitals and the expansion of outer orbitals of higher angular momentum. This complexity is intrinsically linked to the remarkably diverse chemistry of the transition elements, but it presents a challenge to theory.

1.2 Cluster Catalysis

The 'cluster-surface analogy' is a well-established principle in catalytic chemistry.[63] The simple idea is that a cluster of metal atoms somehow replicates the properties of a metal surface (vacant coordination sites, metal-metal bonding), and is, therefore, a potential locus for catalytic activity. Metal nanoparticles (MNPs) have been used for several decades to catalyse different chemical reactions and their cost-effectiveness, activity, efficiency and durability are active areas of research. Noble metals have

found extensive use in this area due to their durability, but the high-cost implications have driven the search for alternatives. It is well known that decreasing the dimension and size of nanoparticles can increase the catalytic performance.[64] This last observation points naturally to the concept of single-, double and triple-atom catalysis (SACs, DACs and TACs) where the 'nanoparticle' is reduced to its smallest conceivable dimensions. The chemistry of single-atom catalysts (SACs) is now relatively well established and many reviews have been devoted to their synthesis and activity.[65–67] SACs have obvious potential because they offer 100% active atomic utilisation which naturally leads to high catalytic performance, high selectivity and adsorption of reactants at the unique active atomic centre. However, it has some drawbacks, especially for reactions with many intermediates which might demand more flexibility than can be provided by a single metal site. In this context, double- and triple-atom catalysts (DACs and TACs) offer more options, and the logical extension to this is to consider heterogeneous single-cluster catalysts (SCCs) consisting of atomically precise and isolated clusters on a supported surface.[63] SCCs bridge the gap between heterogeneous SACs and MNCs.[68,69] In the sub-nanometer regime, the single clusters typically consist of 2-20 atoms and may be homoatomic, heteroatomic and may incorporate a mixture of non-metallic atoms as promoters or ligands. The synthesis of SCCs with well-defined atomic compositions and structures is a challenging task because under-coordinated metal ions are rather unstable, but progress with physical methods such as gas-phase condensation, ion implantation and laser ablation suggests that these experimental challenges will, ultimately, be surmountable.[70,71] More precise techniques like atomic layer deposition[72,73] may also present opportunities to control the size and composition of deposited clusters on the supports. The choice of support material and reaction conditions (temperature, pressure, duration and post-treatment procedures) is also crucial to achieving the desired size and shape of the cluster.

Computational studies have been central to our understanding of structure-property-performance relationships in SCCs, which often show fascinating quantum phenomena due to electronic confinement.[74,75] The properties of SCCs are influenced not just by the size and the identity of the metal, but also by the metal-support interactions.[76] The catalytic activity of SCCs depends critically on the interactions between the active sites and the reactive intermediates, and the larger number of atoms compared to a SAC, DAC or TAC offers greater flexibility to tailor the adsorption sites and electronic structures of the catalysts, improving the potential of catalysing complex reactions compared to the SACs. For example, Pd-based SACs are unable to catalyse

the methane to methanol conversion reaction because of weak interaction between Pd and CH_4, whereas a Pd_2 cluster can provide the multiple adsorption sites required to activate both CH_4 and O_2.[77] The incorporation of heteroatoms, size-dependent electronic properties, and the nature of the support in SCCs provides a valuable strategy for adapting catalytic efficiency and selectivity. A schematic model of challenges and future directions in the synthesis, characterisation and application of SCCs is shown in Figure 1.6.[63]

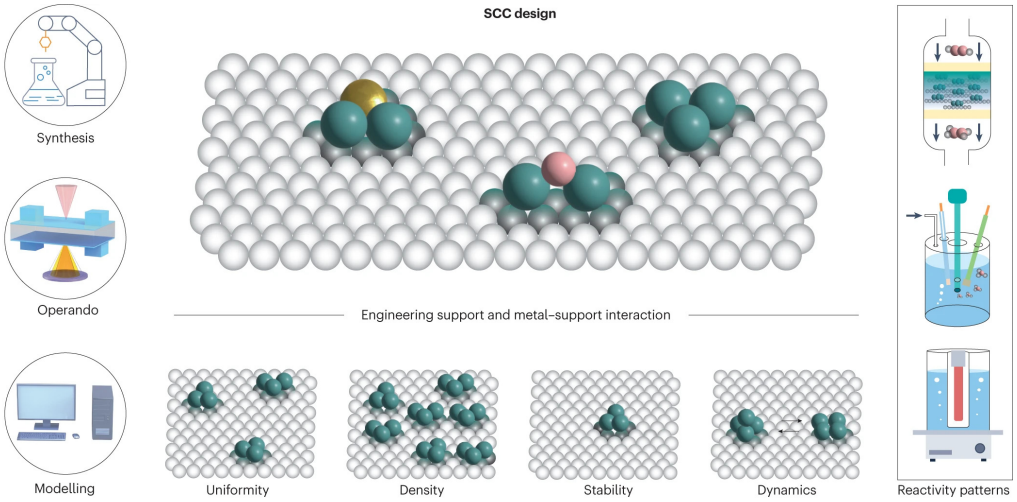

Figure 1.6: Schematic model of challenges and future directions in the synthesis, characterisation and application of SCCs. Adapted with permission from Reference.[63] Copyright 2023 Nature Publishing Group UK London.

In the case of heteroatomic clusters, the synergy between the different metal atoms provides a further handle to tune the properties, and a number of heterometallic SCCs have been used for reactions such as the hydrogen evolution reaction (HER), the oxygen evolution reaction (OER), the oxygen reduction reaction (ORR), CO_2/CO reduction reaction, N_2 reduction reaction, (reverse) water gas shift reaction (WGSR) etc.[78–80] In our work, reported in Chapter 4, I will emphasise the importance of the Ru-Sn junction in this context. The metal clusters are typically anchored to the support through covalent bonds and/or electrostatic interactions,[81] allowing the support to modulate the geometric, electronic and catalytic properties of the nanoclusters. The most common supports are oxides (CeO_2, Al_2O_3, Fe_2O_3, MgO, SiO_2), 2D materials (graphene, MoC, MoS_2 and some porous materials (graphdiyne, carbon-nitride compounds, MOFs), and we can make a clear distinction between those which are redox active (CeO_2, TiO_2, Fe_2O_3) and those which are not. For example, the Pt_4 cluster retains the gas-phase tetrahedral structure when deposited on a MgO support

surface but changes to a square-planar geometry when deposited on $TiO_2(110)$ as a result of significant charge transfer from metal to the Ti^{4+} ions.[82]

Looking ahead, the diverse range of SCCs offers huge potential for designing advanced catalysts with tailored performance in various thermocatalytic, electrocatalytic and photocatalytic reactions. Zintl clusters have recently been shown to have potential as homogeneous catalysts for organic transformations, although it is not clear yet whether the cluster is active in the reaction or merely acts as a support.[83,84] Some metal-free Zintl clusters have, however, been reported to be effective catalysts for organic reactions: for example, Mehta and co-workers have pioneered metal-free $[P_7]^{n-}$ clusters that are very effective for CO_2 reduction to methanol.[85–87] Only a few Zintl clusters have been deposited on supports most notably the work by Sun and co-workers where the $[Ru@Sn_9]^{6-}$ Zintl cluster supported on a $CeO_2(111)$ surface proves to be highly efficient and tunable for CO_2 reduction via the reverse water gas shift reaction.[3] This experimental work provides the motivation for Chapter 4, where a full review of the key findings will be presented.

Chapter 2

Theoretical Background

In this chapter, we introduce the fundamental principles of quantum theory essential in chemistry and electronic structure theory based on modern computational methods, which are utilised in several projects. We also discuss some fundamental models used to analyse the results such as chemical bonding and density of states.

2.1 Schrödinger Equation

Fundamental studies of quantum mechanics start with the Schrödinger equation which describes how the quantum state of a physical system changes with time. Most of the computational chemistry studies are mainly concerned with the time-independent Schrödinger equation to find the solutions for electronic systems:

$$\hat{H}\psi = E\psi \tag{2.1.1}$$

$\hat{H}$ is the total energy Hamiltonian, ψ is the wavefunction.

$$\hat{H} = \hat{T}_e + \hat{T}_N + \hat{V}_{ee} + \hat{V}_{Ne} + \hat{V}_{NN} \tag{2.1.2}$$

where,

- $\hat{T}_e$ is the kinetic energy of electrons
- $\hat{T}_N$ is the kinetic energy of nuclei
- $\hat{V}_{ee}$ is the potential energy of electron-electron interaction
- $\hat{V}_{Ne}$ is the potential energy of electron nucleus interaction
- $\hat{V}_{NN}$ is the potential energy of nucleus-nucleus interaction

Electrons are negatively charged particles whereas nuclei are positively charged. There is Coulomb repulsion between electron-electron ($\hat{V}_{ee}$) and nucleus-nucleus ($\hat{V}_{NN}$), on the other hand, there is attraction force between electron and nucleus ($\hat{V}_{Ne}$). The Hamiltonian operator for a molecular system with M nuclei and n electrons can be written as (in atomic units)

$$\hat{H} = -\frac{1}{2}\sum_{i=1}^{N}\nabla_i^2 - \frac{1}{2}\sum_{A=1}^{M}\frac{1}{M_A}\nabla_A^2 - \sum_{i=1}^{N}\sum_{A=1}^{M}\frac{Z_A}{r_{iA}} + \sum_{i=1}^{N}\sum_{j>i}^{N}\frac{1}{r_{ij}} + \sum_{A=1}^{M}\sum_{B>A}^{M}\frac{1}{R_{AB}} \quad (2.1.3)$$

where ∇^2 is the Laplacian operator for the kinetic term, M_A is the mass and Z_A is atomic number of the nucleus A, $r_{ij} = |r_i - r_j|$, $r_{iA} = |r_i - r_A|$ and $R_{AB} = |R_A - R_B|$.

To make this equation simpler and easier to handle in quantum mechanics the first approximation is considered, called *Born-Oppenheimer Approximation*. Based on the fact that the nucleus is much heavier than the electrons, the wave functions of an atomic nucleus and electrons can be approximated to treat them separately. This allows us to neglect the nuclear kinetic term $\hat{T}_N$ and the internuclear potential term $\hat{V}_{NN}$, and define the electronic hamiltonian as:

$$\hat{H}_e = \hat{T}_e + \hat{V}_{Ne} + \hat{V}_{ee} \quad (2.1.4)$$

or,

$$\hat{H}_e = -\frac{1}{2}\sum_{i=1}^{N}\nabla_i^2 - \sum_{i=1}^{N}\sum_{A=1}^{M}\frac{Z_A}{r_{iA}} + \sum_{i=1}^{N}\sum_{j>i}^{N}\frac{1}{r_{ij}} \quad (2.1.5)$$

The observable energy E of the system can be obtained from the expectation value of the Hamiltonian $\hat{H}$ operating on a wavefunction $\psi(\tau)$:

$$E = \frac{\langle\psi|\,\hat{H}\,|\psi\rangle}{\langle\psi|\psi\rangle} = \frac{\int \psi^*\hat{H}\psi\delta\tau}{\int \psi^*\psi\delta\tau} \quad (2.1.6)$$

The Schrödinger equation is difficult to solve exactly (except for the simplest case, one-electron systems), so we are interested in finding the solution of the eigenvalue equation as close as possible. The theorem, known as the Variation Principle, allows us to systematically approach the ground state wavefunction. This states that the energy associated with a trial wavefunction ψ' is always greater than the ground-state energy. The equal energy is only achievable when the trial wavefunction is the true wavefunction of the system.

$$E' = \frac{\langle\psi'|\,\hat{H}\,|\psi'\rangle}{\langle\psi'|\psi'\rangle} \geq E_0 = \frac{\langle\psi_0|\,\hat{H}\,|\psi_0\rangle}{\langle\psi_0|\psi_0\rangle} \quad (2.1.7)$$

2.2 Hartree-Fock Theory

2.2.1 Slater Determinant

The next step is to formulate the wavefunction in such a way that it is consistent with the Pauli exclusion principle, which demands that the total wavefunction has to be antisymmetric with respect to the exchange of any two particles. A simple product of individual wavefunctions (called orbitals) does not satisfy these antisymmetry requirements, but a Slater determinant, shown below, does.

An N-electron Slater determinant can be defined as:

$$\Psi_{HF}(\mathbf{x}_1, \mathbf{x}_2, ..., \mathbf{x}_N) = \frac{1}{\sqrt{N!}} \begin{vmatrix} \chi_1(\mathbf{x}_1) & \chi_2(\mathbf{x}_1) & \cdots & \chi_N(\mathbf{x}_1) \\ \chi_1(\mathbf{x}_2) & \chi_2(\mathbf{x}_2) & \cdots & \chi_N(\mathbf{x}_2) \\ \vdots & \vdots & & \vdots \\ \chi_1(\mathbf{x}_N) & \chi_2(\mathbf{x}_N) & \cdots & \chi_N(\mathbf{x}_N) \end{vmatrix} \tag{2.2.1}$$

where Ψ_{HF} is the total wavefunction, $\chi_i(\mathbf{x}_i)$ is the spin-orbital (product of spatial wavefunction and spin function) of the i-th electron and the variable $\mathbf{x}$ include the spatial and spin part. If any two rows (representing two electrons) are swapped (exchanging particles), the determinant changes sign.

2.2.2 Hartree-Fock Equation

The next step is to simplify the Hamiltonian from equation 2.1.5. We can define an one-electron operator h as follows

$$h(i) = -\frac{1}{2}\nabla_i^2 - \sum_{A=1} \frac{Z_A}{r_{iA}} \tag{2.2.2}$$

and a two-electron operator $v(i,j)$ as

$$v(i,j) = \frac{1}{r_{ij}} \tag{2.2.3}$$

Now, the electronic Hamiltonian can be written as

$$\hat{H}_e = \sum_i h(i) + \sum_{i<j} v(i,j) \tag{2.2.4}$$

The Hartree-Fock energy expression from the Hartree-Fock wavefunction and the Hamiltonian is:

$$\begin{aligned} E_{HF} &= \langle \Psi | \, \hat{H}_e \, | \Psi \rangle \\ &= \sum_i \langle \chi_i | \, \hat{h} \, | \chi_i \rangle + \frac{1}{2} \sum_{ij} \langle \chi_i \chi_j | \chi_i \chi_j \rangle - \langle \chi_i \chi_j | \chi_j \chi_i \rangle \\ &\equiv \sum_i \langle \chi_i | \, \hat{h} \, | \chi_i \rangle + \frac{1}{2} \sum_{ij} \langle \chi_i \chi_j | \, | \chi_i \chi_j \rangle \end{aligned} \tag{2.2.5}$$

where the one electron integral is

$$\langle \chi_i | \, \hat{h} \, | \chi_j \rangle = \int d\mathbf{x}_i \chi_i^*(\mathbf{x}_i) h(i) \chi_j(\mathbf{x}_i) \tag{2.2.6}$$

and the two-electron integral is

$$\langle \chi_i \chi_j | \chi_i \chi_j \rangle = \int \mathrm{d}\mathbf{x}_i \mathrm{d}\mathbf{x}_j \chi_i^*(\mathbf{x}_i) \chi_j^*(\mathbf{x}_j) \frac{1}{r_{ij}} \chi_k(\mathbf{x}_i) \chi_j(\mathbf{x}_j) \tag{2.2.7}$$

The orbitals χ_i should be normalised and the overlap integral between two orbitals χ_i and χ_j can be constrained as:

$$\langle \chi_i | \chi_j \rangle = \delta_{ij} \tag{2.2.8}$$

To enforce this constraint while minimising the total energy functional, Lagrange multipliers are introduced. The Lagrangian, $\mathcal{L}$, that is used to incorporate the normalisation condition into the variational principle, is given by:

$$\mathcal{L} = E[\chi_i] - \sum \lambda_i (\langle \chi_i | \chi_i \rangle - 1) \tag{2.2.9}$$

where λ_i is the Lagrange multiplier associated with the normalisation constraint for each orbital and ensures that the orbitals remain normalised during the optimisation of the energy functional.

To minimise the energy expression, we apply the variational principle with the help of Lagrange's multiplier and eventually arrive at the Hartree-Fock equation:

$$\hat{h}(\mathbf{x}_i)\chi_i(\mathbf{x}_i) + \sum_{j \neq i} \left[\int d\mathbf{x}_j |\chi_j(\mathbf{x}_j)|^2 r_{ij}^{-1} \right] \chi_i(\mathbf{x}_i) - \sum_{j \neq i} \left[\int d\mathbf{x}_j \chi_j^*(\mathbf{x}_j) \chi_i(\mathbf{x}_j) r_{ij}^{-1} \right] \chi_j(\mathbf{x}_i) = \epsilon_i \chi_i(\mathbf{x}_i) \tag{2.2.10}$$

The first term in the square bracket gives the Coulomb interaction of an electron in spin-orbital χ_i with the average charge distribution of the other electrons, called the *Coulomb* term ($\hat{J}_j(\mathbf{x}_i)$). The term in the second square bracket does not have a simple classical analogue, but instead arises from the antisymmetry of the wavefunction. It is superficially similar to the coulomb term, except that the spin orbitals χ_i and χ_j are swapped, and this term is called the 'exchange term' ($\hat{K}_j(\mathbf{x}_i)$).

Now, this equation becomes considerably more compact.

$$\left[\hat{h}(\mathbf{x}_i) + \sum_{j \neq i} \hat{J}_j(\mathbf{x}_i) - \sum_{j \neq i} \hat{K}_j(\mathbf{x}_i) \right] \chi_i(\mathbf{x}_i) = \epsilon_i \chi_i(\mathbf{x}_i) \tag{2.2.11}$$

We can introduce a new operator, the Fock operator as,

$$f(\mathbf{x}_i) = \hat{h}(\mathbf{x}_i) + \sum_j \hat{J}_j(\mathbf{x}_i) - \hat{K}_j(\mathbf{x}_i) \tag{2.2.12}$$

Note that the exchange term enters the equation with the opposite sign to the Coulomb term, and so the role of exchange interaction is to reduce the repulsion between like-spin electrons.

Finally, the Hartree-Fock equation in the simplest form can be written as,

$$f(\mathbf{x}_i)\chi_i(\mathbf{x}_i) = \epsilon_i\chi_i(\mathbf{x}_i) \tag{2.2.13}$$

2.2.3 Self-Consistent Field (SCF)

The Hartree-Fock equation can be solved by introducing a finite number of M known basis functions ϕ_α to form a spin-orbital χ_i, known as a molecular orbital (MO) which is constructed by the linear combination of atomic orbitals (LCAO) belonging to the basis ϕ_α with coefficient C_α. Now,

$$\chi_i(\mathbf{x}_i) = \sum_{\alpha=1}^{M} C_{\alpha i}\phi_\alpha(\mathbf{x}_i) \tag{2.2.14}$$

The Hartree-Fock equation looks like;

$$f(\mathbf{x}_i)\sum_{\alpha=1}^{M} C_{\alpha i}\phi_\alpha(\mathbf{x}_i) = \epsilon_i \sum_{\alpha=1}^{M} C_{\alpha i}\phi_\alpha(\mathbf{x}_i) \tag{2.2.15}$$

This can be represented in a matrix form and is called the Roothan-Hall equation;

$$FC = \epsilon SC \tag{2.2.16}$$

where F is the matrix of the Fock operator, $F_{\alpha\beta} = \langle\phi_\alpha| f |\phi_\beta\rangle$, C is the coefficient vector, ϵ is the diagonal matrix of the orbital energies ϵ_i and S is the overlap matrix, $S_{\alpha\beta} = \langle\phi_\alpha|\phi_\beta\rangle$. The HF equation can be solved by using an iterative process. This process is called the '*S*elf-*C*onsistent *F*ield' (*SCF*) method, which takes a set of guessed spin orbitals and iteratively improves them, as shown in a schematic plot in Figure 2.1.

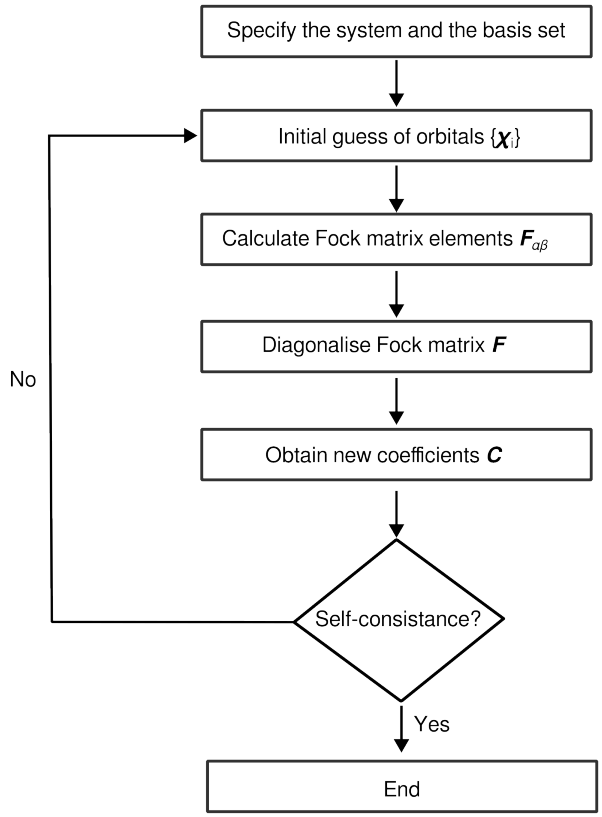

Figure 2.1: Flow diagram of the SCF cycle.

2.3 Density Functional Theory

Density Functional Theory is an approach to solving the Schrödinger equation by utilising the particle density instead of the wavefunction. The Hartree-Fock N-electron wavefunction (Ψ_{HF}) depends on 3N spatial and N spin variables, making the equation complicated for larger systems. In DFT, the wavefunction is replaced with the electron density which depends on only 3 dimensions of space and still can capture most of the properties like ground state energy, charge density, molecular orbitals etc. efficiently. The electron density $n(\mathbf{r})$, with the normalised wavefunction, Ψ can be written as

$$n(\mathbf{r}) = N \int d^3\mathbf{r}_2 \cdots \int d^3\mathbf{r}_N \Psi^*(\mathbf{r}, \mathbf{r}_2, ..., \mathbf{r}_N)\Psi(\mathbf{r}, \mathbf{r}_2, ..., \mathbf{r}_N) \tag{2.3.1}$$

This relation can be reversed; if we know the ground state density $n_0(\mathbf{r})$, it is possible to extract the ground state wavefunction $\Psi_0(\mathbf{r}_1, ..., \mathbf{r}_N)$. Ψ is a unique functional of

n_0

$$\Psi_0 = \Psi[n_0] \tag{2.3.2}$$

The theoretical basis of DFT lies in two key theorems proposed by Hohenberg and Kohn[88] in 1964:

1. The first Hohenberg-Kohn theorem states that the ground-state properties of a many-electron system are uniquely determined by its electron density $n(\mathbf{r})$.

2. The second theorem establishes that there exists a functional $E[n]$ of the electron density which gives the ground state energy of the system. The functional obeys the variational theorem, i.e. it gives the lowest energy if and only if the input density is the true ground state density.

While the Hohenberg-Kohn theorems establish the theoretical basis for DFT, they do not provide a practical method to compute the functional $E[n]$. Indeed, even before density functional theory was legitimised by Hohenberg and Kohn, there were many attempts to utilise the density to approximate the Hartree-Fock theory and find the electronic ground state. The earliest of these was by Thomas and Fermi, who proposed a solution in 1927 based on a statistical distribution of electrons in atoms and has the simple form:

$$E^{TF}[n(\mathbf{r})] = C_1 \int d\mathbf{r} n^{\frac{5}{3}}(\mathbf{r}) - C_2 \int d\mathbf{r} \frac{n(\mathbf{r})}{r} + \frac{1}{2} \int d\mathbf{r}_1 d\mathbf{r}_2 \frac{n(\mathbf{r}_1) n(\mathbf{r}_2)}{|r_1 - r_2|} \tag{2.3.3}$$

The first term is an approximation to the kinetic energy, the second term is electron-nucleus interaction and the last term is electron-electron interactions. The main contribution of total energy comes from the kinetic term and it is here that the Thomas-Fermi kinetic energy proves to be very inaccurate, often failing to predict the presence of bonds. In 1965, Kohn and Sham realised that the kinetic energy could be calculated accurately using a set of orbitals (Kohn-Sham orbitals) which reproduced the density. The *Kohn-Sham* equation[89] which is a non-interacting Schrödinger equation of a fictitious system where particles don't interact with each other, can generate the same density as in an interacting system. The Kohn-Sham approach allowed for the calculation of properties of matter at the atomic and molecular scale at a level of accuracy that was previously unavailable. The Kohn-Sham theory also introduces a non-interacting kinetic energy functional T_s and Kohn-Sham potential $v_{eff}(\mathbf{r})$. The KS wavefunction is a single Slater determinant constructed from a set of KS orbitals, χ_i that are the lowest energy solution to

$$\left[-\frac{\hbar}{2m} \nabla^2 + v_{eff}(\mathbf{r}) \right] \chi_i(\mathbf{r}) = \epsilon_i \chi_i(\mathbf{r}) \tag{2.3.4}$$

ϵ_i is the orbital energy of the corresponding KS orbital χ_i and the density of N particle system is

$$n(\mathbf{r}) = \sum_{i}^{N} |\chi_i(\mathbf{r})|^2 \tag{2.3.5}$$

In Kohn-Sham density functional theory, the total energy of the system can be written as a functional of charge density and the total energy expression is

$$E[n] = T_s[n] + \int d\mathbf{r} v_{ext}(\mathbf{r}) n(\mathbf{r}) + E_H[n] + E_{xc}[n] \tag{2.3.6}$$

where T_s is the KS kinetic energy which can be expressed as

$$T_s[n] = \sum_{i}^{N} \int d\mathbf{r} \chi_i^*(\mathbf{r}) \left(-\frac{\hbar}{2m} \nabla^2 \right) \chi_i(\mathbf{r}) \tag{2.3.7}$$

v_{ext} is the potential acting on the interacting system (electron-nucleus interaction), E_H is the Hartree (or Coulomb) energy and E_{xc} is the exchange-correlation energy

$$E_H[n] = \frac{1}{2} \int d\mathbf{r}_1 d\mathbf{r}_2 \frac{n(\mathbf{r}_1) n(\mathbf{r}_2)}{|r_1 - r_2|} \tag{2.3.8}$$

and,

$$v_{xc}(\mathbf{r}) \equiv \frac{\delta E_{xc}[n]}{\delta n(\mathbf{r})} \tag{2.3.9}$$

is the exchange-correlation potential. The E_{xc} is complicated to solve numerically, as the exact electron-electron interaction is hard to calculate.

2.3.1 Exchange-Correlation Functionals

Different exchange-correlation terms have been proposed mainly fitting to some particular small electronic systems. The simplest formalism is the Local Density Approximation (LDA) which assumes that the E_{xc} depends on the density at a point $\mathbf{r}$:

$$E_{xc}^{LDA}[n] = \int d\mathbf{r} n(\mathbf{r}) \epsilon_{xc}[n(\mathbf{r})] \tag{2.3.10}$$

Under the LDA, the exchange-correlation energy is decomposed into exchange and correlation terms linearly,

$$E_{xc} = \epsilon_x + \epsilon_c \tag{2.3.11}$$

The exchange term is analytic and can be calculated at each point using the equation

$$\epsilon_x = -\frac{3}{4} \left(\frac{3}{\pi} \right)^{1/3} \int n(\mathbf{r})^{4/3} d\mathbf{r} \tag{2.3.12}$$

The most successful LDA approaches are based on a uniform electron gas model in which the total number of electrons (N) and the volume of gas (V) approach infinity, but the electron density (n =N/V) is finite and constant everywhere. The exact form of the correlation term ϵ_c is unknown and numerous different approximations have been proposed. The local density approximation by itself does not give a significant accuracy in a real system as it relates to a homogeneous electron density, whereas the electron density in a real molecular system is very inhomogeneous. Therefore, we need to take into account the gradient of the electron density at that point. This is known as the 'gradient corrected' or 'generalised gradient approximation' (GGA) method and the function can be expressed as:

$$E_{xc}^{GGA}[n] = \int d\mathbf{r} n(\mathbf{r}) \epsilon_{xc}[n(\mathbf{r}), \nabla n(\mathbf{r})] \tag{2.3.13}$$

Most of the GGA functionals modify the expression for ϵ_x (or ϵ_c) by adding a correction term to the LDA exchange (or correlation) term,

$$\epsilon_x = \epsilon_x^{LDA} + \Delta\epsilon_x \left[\frac{|\nabla n(\mathbf{r})|}{n^{\frac{4}{3}}(\mathbf{r})} \right] \tag{2.3.14}$$

This class of functions is widely used because of its good compromise between computational cost and accuracy. The first popular GGA exchange functional was pioneered by Becke[90] in 1988 and other exchange functionals are FT97, OPTX, PW fitting different empirical parameters.[91] Alternative GGA exchange functionals have been developed based on rational function expansion of the reduced functional, which does not contain empirical parameters, including B86, PBE and mPBE.[92,93] In terms of GGA correlation functionals, a popular one is P86 which fits one empirical parameter to the correlation energy of the neon gas atom. Another popular functional is LYP, developed by Lee, Yang and Parr which contains four empirical parameters for a helium atom. A combination of exchange and correlation corrected GGA functional resulted in some popular functionals such as BLYP, BP86, and BPW91 to try to describe the whole system.[90]

Particularly in the case of transition metals, HF theory tends to over-stabilise high-spin ground states, whereas GGA functionals favour low-spin states. A good strategy is to combine two methods called 'hybrid functional' in which the exchange functional is partially described as in Hartree-Fock theory, and the correlation functional is the default of GGA. The most commonly used hybrid functional for molecular DFT especially in organic chemistry is B3LYP.[94,95] The simplest way to represent a hybrid functional is:

$$E_{xc}^{hybrid} = \alpha E_x^{GGA} + (1-\alpha)E_x^{HF} + E_c^{GGA} \tag{2.3.15}$$

For example, PBE0 uses PBE as its GGA basis and $\alpha = \frac{1}{4}$.[92,93] Another hybrid functional HSE06 is increasing in popularity especially in solid state calculations as it is computationally cheap and uses the PBE0 hybrid functional for short range and PBE at long range, with hlthe error function to interpolate smoothly between two.[96] Adding the Hubbard correction term (U) for electronic repulsion with GGA functional can predict the energy fairly correctly with significantly low cost compared to the hybrid functional.[97,98] The Hubbard U correction, also known as the DFT+U method, introduces an additional term to the DFT functional to account for the on-site Coulomb interaction between localised electrons. The idea behind the Hubbard U correction is to modify the effective electron-electron interaction to better treat localised electron correlations, especially on transition metal ions or lanthanide elements where d or f orbitals are strongly correlated.

2.4 Basis Sets

In HF, DFT and post-HF methods we compute the electronic structure of chemical systems by solving the Schrödinger equation where the Hamiltonian operator operates on the wavefunction. In order to calculate the various matrix elements required in the SCF procedure, we require a basis set - a set of functions that describe the spatial properties of the electrons. Localised atomic-orbital-like functions are typically used as a basis in molecular systems whereas a plane wave basis is more appropriate to the periodic boundary conditions of a periodic solid-state calculation. A complete basis set would have an infinite number of independent basis functions, but of course, this is not achievable in practice and so pragmatic choices need to be made.

2.4.1 Atomic Orbital Basis Sets

Atom-centred basis functions can be classified into two categories, Slater-type orbitals (STOs) and Gaussian-type orbitals (GTOs). The STOs can be mathematically written as:

$$\chi^{STO}(\mathbf{r}) = NY_{l,m}(\theta,\phi)r^{n-1}e^{-\zeta r} \tag{2.4.1}$$

where N is the normalisation constant, ζ is the orbital exponent. r, θ, ϕ are spherical coordinates and $Y_{l,m}$ is the angular momentum part, which describes the shape of the orbitals. n, l and m are the principal, angular and magnetic quantum numbers

respectively. The e^{-r} dependence of STOs is exactly what is found in hydrogen-like systems, but STOs are mathematically inconvenient, particularly when it comes to the analytical calculation of the two-electron integrals noted above. Gaussian-type orbitals provide an alternative to the STOs. The GTOs can be expressed as:

$$\chi^{GTO}(\mathbf{r}) = NY_{l,m}(\theta, \phi)r^{2n-2-l}e^{-\zeta r^2} \tag{2.4.2}$$

And the key difference is that they have an e^{-r^2} dependence. This is a less accurate depiction of atomic wavefunctions - GTOs decay too rapidly away from the nucleus and they fail to reproduce the cusp at the nucleus. However, there are some advantages to GTOs over STOs as basis functions. The first one is that the basis functions are separable in x, y, z directions and the other is that the product of two GTOs is a GTO (The Gaussian product theorem). These two features combine to make the calculation for the two-electron integrals much easier and more feasible. The practical solution is then to use a linear combination of many Gaussian functions to represent a single Slater orbital, thereby avoiding most of the problematic properties of a single Gaussian function. GTO basis sets are extensively used in HF and post-HF methods, where the calculation of the 2-electron integrals is unavoidable. In the non-hybrid KS-DFT method, in contrast, the two-electron integrals are not required and so STO basis functions become a viable alternative: the Amsterdam Density Functional (ADF) package, which is used extensively in this thesis, is a case in point and all calculations reported here utilising ADF package, use Slater-type functions.

The Slater-type basis is conceptually easy to understand as it is similar to the hydrogenic orbital. In STOs, the hierarchy to improve the accuracy to represent correct atomic orbital (AO) is by:
(i) gradually increasing the number of STOs of the same symmetry but a different exponent of ζ for each AO. This is known as "split valence" because mainly each valence orbital is separated into multiple basis functions.
(ii) adding a number of sets of polarization functions, which correspond to higher angular momentum. This effect allows the orbital to distort from the original symmetry and provide a better description of the molecular environment. For example, in H electron is likely to be in the s orbital but the addition of a p function allows polarisation.
A minimal basis set would be described as a "single zeta" (SZ), where there is no split valence. Whereas, "DZ" uses two STOs (two split valences) to describe an AO. A triple-zeta basis with one polarisation can be represented as "TZP". The naming of basis sets in ADF follows this convention closely, with TZP and TZ2P, for example,

representing triple-zeta basis sets with one and two sets of polarisation functions, respectively.

GTO basis sets are more complex to describe, simply because many primitives can be used and so many types of basis sets are developed. A well-known example of a minimal basis is STO-3G, developed by Pople and co-workers. The STO-3G basis is constructed by 3 GTOs to represent the STO (SZ). The general representation of this type of basis set could be STO-nG, where each STO is modelled by n Gaussians. The valence electrons are most important to capturing all the properties of the molecular system, there it is important to include more accurate descriptions of the valence electrons like split-valence, polarisation and diffusion. Diffuse functions are necessary for a correct description of anions, excited states and diffused electron clouds in second and third-row transition metals. A common example of a Pople-type split-valence basis set is 6-31G, where each core orbitals are represented by 6 primitive GTOs, where valence orbitals are described by 2 basis functions (DZ), the first one consists of 3 primitive and the second one consists of 1 primitive GTOs. The general expression could be W-XYZG where each core orbital is modelled with W primitive GTOs, and each valence orbital is described by 3 basis functions composed of X, Y and Z primitives respectively.[99] If we include a polarisation function, denoted as * and a diffuse function, denoted as + in the basis set then it could be represented as W-XYZ+G*. For example, the 6-31+G* basis set is a double-zeta basis set with one polarisation function and one diffusion function. Several basis sets have been developed over the last few decades and they do not necessarily have to be Pople-style basis sets. The nomenclatures of those basis sets are given uniquely by the developers. One example is the Karlsruhe "def2" sets which is a development of the "double-zeta" concept to improve the accuracy. The basis sets of "def2" family are usually found as def2-SV (SV= split-valence), def2-TZV (triple-zeta) and so on. Adding polarisation functions as P and diffusion function D to the TZ basis set, we can write it as def2-TZVPD.[100] Generally, the largest basis set will give better results compared to the smaller one.

2.4.2 Plane Wave Basis Sets

Both STOs and GTOs are constructed considering that all the basis functions are atom-centered. However, a completely different approach has been used to construct wavefunctions for periodic systems of solids, which is a plane wave basis. Plane-wave basis functions take the form of 'near free electron' wavefunctions and oscillate in one spatial direction (remain constant in the other two directions). From Bloch's

theorem, the eigenstates of an electron in a potential with translational symmetry (e.g. in a crystal) can be described by Bloch wave:[101]

$$\psi_{n,\mathbf{k}}(\mathbf{r}) = e^{i\mathbf{kr}} f_{n,\mathbf{k}}(\mathbf{r}) \tag{2.4.3}$$

where $\mathbf{k}$ is the wavevector in reciprocal space, n is the electron band index (the concept of band is discussed in detail later, in section 2.6) and $f_{n,\mathbf{k}}(\mathbf{r})$ has the periodicity of the system, i.e.,

$$f_{n,\mathbf{k}}(\mathbf{r}) = f_{n,\mathbf{k}}(\mathbf{r} + \mathbf{R}) \tag{2.4.4}$$

$\mathbf{R}$ is the lattice vector. The Block wave $\psi_{n,\mathbf{k}}(\mathbf{r})$ can be simplified by splitting it into two parts. The exponential part is called the 'phase' part and the other part is called the 'cell-periodic' part i.e. $f_{n,\mathbf{k}}(\mathbf{r})$ as it represents the periodicity of an infinite cell. The cell-periodic part can be written as a linear combination of plane waves

$$f_{n,\mathbf{k}}(\mathbf{r}) = \sum_{\mathbf{G}} c_{\mathbf{G},n,\mathbf{k}} e^{i\mathbf{Gr}} \tag{2.4.5}$$

where $\mathbf{G}$ is the reciprocal lattice vector. Now the wavefunction $\psi_{n,\mathbf{k}}(\mathbf{r})$ can be expanded as

$$\psi_{n,\mathbf{k}}(\mathbf{r}) = \sum_{\mathbf{G}} c_{\mathbf{G},n,\mathbf{k}} e^{i(\mathbf{G}+\mathbf{k})\mathbf{r}} \tag{2.4.6}$$

This equation is analogous to a linear combination of atomic orbitals, but the localised orbitals have been replaced by delocalised waves. Again, it's not feasible to work with an infinite basis set. A finite basis set could be described by, firstly, rather than taking infinite numbers of k-points and sampling only a special set of k-points in the first Brillouin zone. Secondly, by setting an energy cutoff value E_{cutoff} in the calculation. For a specific $\mathbf{k}$, the place wave basis function which satisfies the criteria of $\frac{\hbar}{2m}|\mathbf{G}+\mathbf{k}|^2 \leq E_{cutoff}$ will be considered. The unit of E_{cutoff} is the unit of energy, therefore the cutoff condition can be viewed as the kinetic energy of the plane wave $e^{i(\mathbf{G}+\mathbf{k})\mathbf{r}}$.

2.4.3 Core electrons and Pseudopotential

Atomic orbitals close to the nuclei (core orbitals) usually oscillate rapidly and do not generally contribute to bonding, rather atomic orbitals oscillate smoothly in the outer region (valence orbitals) and capture most of the useful information of the system. The full electron basis sets described above are computationally expensive, especially for translational metals and heavier elements for a larger system. Therefore, we can consider only the valence orbitals in the equation, treating the core approximately.

Implementing an 'effective core potential' (ECP) or 'frozen core' approximation to the core electrons of heavier atoms can be more economical without compromising accuracy.[102] The SCF procedure runs only on the valence electrons, where the core orbitals' energy is already given, and the relativistic effect is also considered. For solid-state periodic systems where we use a plane wave basis set, the common way to represent the core is to account for 'pseudopotential'.[103] In this model, the nucleus and core are represented by an electrostatic potential and the valence electrons interact with the electrostatic potential (pseudopotential). An advanced pseudopotential method that combines the benefits of pseudopotentials and full wavefunction methods is the Projector Augmented-Wave (PAW) method.[104] Using a projector technique allows for a more accurate description of the core and valence electrons.

2.5 Analysis: Qualitative Models of Chemical Bonding

Chemical bonding is one of the fundamentals of chemistry that helps us understand the structures, properties, and reactions of molecules and solids. The presence or absence of a bond is not uniquely defined, and it has long been a challenge in inorganic chemistry to decide how best to describe a structure. In this section, I will review some of the quantum chemical approaches which have been developed to explore the nature of chemical bonds, from Lewis's localised pair of electrons to the delocalised models.

2.5.1 Foundations

Though speculation about the nature of chemical bonding started several centuries ago, major developments in the field only occurred in the early 20th century after Rutherford's discovery of an atomic nucleus surrounded by electrons and Bohr's model. Niels Bohr proposed the electronic orbitals as a basis of the theory that atoms interact with each other through their electrons.[105] In 1916, chemist Gilbert N. Lewis proposed a bonding model by the concept of electron pairing, in which two atoms may share a pair of electrons to form a bond.[106] He also highlighted that more electron sharing (one to six) could effectively contribute to forming multiple bonds between two atoms. This model treats bonds as primarily two kinds, covalent bonds and ionic bonds. In an ionic bond, the electron pairs are mostly localised on the more electron-negative atom whereas in a covalent bond, the electron pairs are shared equally between two atoms. This concept has been utilised in the octet rule

which states that electron sharing or transfer proceeds until an atom acquires an octet (eight electrons) configuration on the valence shell, equivalent to a noble gas atom. This simple model has been very effective in predicting the structure and formula of stable compounds, which are represented in modern chemistry by 'Lewis structure' or 'dot-cross diagram'. The role of the electron pair and the quantitative description of bonding must be based on the Schrödinger equation and the Pauli exclusion principle, which reconciles covalent bonding with wavefunction-based descriptions of electrons. Two sophisticated theories are (i) valence bond theory (VBT) which includes orbital hybridisation and resonance, and (ii) molecular orbital (MO) theory which is based on the linear combination of atomic orbitals (LCAO). We will mainly focus on the MO theory as it is now far more prevalent in quantum chemistry. Molecular Orbital (MO) theory provides a quantum mechanical description of the formation of bonds and the electronic structure of molecules by considering the linear combination of atomic orbitals (LCAO) into molecular orbitals that are not associated with any single atom but rather on the entire molecule. In this model, when two atoms are significantly close to each other, their atomic orbitals combine in a constructive way (in-phase) to give a "bonding" molecular orbital that has lower energy and in a destructive manner (out-of-phase) to give an "antibonding" molecular orbital of higher energy. A "non-bonding" orbital can be associated with atomic orbitals that do not interact positively or negatively with one another and don't contribute to the bond strength. The MOs will be filled by electrons which have lower energy first, obeying the Pauli exclusion principle. Since we will have the total number of molecular orbitals as the sum of the atomic orbitals, every bonding combination must have a corresponding anti-bonding combination. The total number of electrons determines the stability of the molecule through the "bond order", defined as half of the difference between the number of electrons in bonding orbitals and antibonding orbitals ($BO = \frac{1}{2}[n_b - n_a]$). Bond order also provides information about how strong the bond is: bond order zero suggests no bond, whereas a positive bond order confirms that the bond is stable. MO Theory also offers a straightforward explanation for the existence of paramagnetic molecules such as O_2, where unpaired electrons populate degenerate orbitals. MO Theory can also be extended readily to polyatomic molecules, taking full advantage of molecular symmetry.

2.5.2 Modern Methods

Density Functional Theory (DFT) is used to investigate the electronic structure of molecules and solids. The molecular orbitals (MOs) obtained from DFT calculations

provide detailed information about the distribution and interactions of electrons in a system. Extracting bonding information from DFT molecular orbitals is essential for understanding the nature of chemical bonds, electron delocalisation, and molecular stability. In this context, several analytical methods can be employed to interpret the bonding characteristics, including visualisation of molecular orbitals, Natural Bond Orbital (NBO) analysis, bond order calculations (like Mayer's analysis), and topological analysis via the Quantum Theory of Atoms in Molecules (QTAIM). These methods offer different perspectives on bonding and provide complementary insights into the bonding structure of molecules.

Mayer's bond order is a numerical measure that quantifies the strength and type of bonding between two atoms based on the overlap of their molecular orbitals as the overlap integral derived from the DFT wavefunction. For a bond between two atoms A and B, the bond order is computed from the density matrix elements of the occupied orbitals of A and B. On the other hand, NBO theory transforms the molecular orbitals into a set of real-space orbitals that more accurately describe chemical bonding by partitioning the electron density, which can be interpreted as the "localised" representation of bonding interactions. NBO analysis provides information about natural population analysis (NPA), which quantifies the electron density of each atom and helps to identify the bond order. These methods could not be precise for more complicated systems where the number of atoms is large, delocalised and correlated. An advanced technique is the QTAIM, developed by Richard Bader, which analyses the electron density distribution within a molecule by studying its topological properties. It divides a molecule into several distinct regions corresponding to atomic regions and bonds. These regions are derived from the critical points in the electron density, providing a more accurate and physically meaningful description of bonding interactions than traditional approaches like molecular orbital theory alone. The most important critical point is the bond critical point (BCP) for bonding analysis between two atoms and the electron density at the BCP capture most of the information. A high electron density at the BCP means a strong covalent bond and vice versa. The Laplacian of the electron density, $\nabla^2 n(r)$ is another important quantity to get information about the nature of the nature of the chemical bond. If the $\nabla^2 n(r)(BCP) < 0$, then it is a covalent bond and if the value is positive then there is an ionic or non-covalent interaction. QTAIM analysis also helps to study the electron delocalisation (resonance or conjugation), charge distribution, non-covalent interaction (hydrogen bonding, van der Waals forces) etc. in a molecular system.

2.6 Electronic Structure in Solids

In molecular systems, we describe the electronic configuration and properties by analysing the discrete energy levels of the system based on MO theory. However, the crystals possess translational symmetry in crystalline solids and describe a range of energy levels (bands) based on the electronic band structure. This can be derived by solving quantum mechanical wavefunctions for an electron in a large, periodic lattice of atoms or molecules, called band theory. Two complementary models have emerged to describe the formation of electronic bands and band gaps in periodic solids. The first one is the 'nearly free electron model', where the electrons are assumed to move freely and delocalise in the lattice and this model has been utilised in Bloch's theorem. The other is the 'tight-binding model' where electrons are localised in atomic orbitals. In a crystal lattice, the overlap of a large number (N $\approx 10^{22}$) of such orbitals turns each discrete energy level into a band: for example, in diamond (Figure 2.2), the s and p orbitals form separate bands which merge into sp hybrids at short interatomic distances.

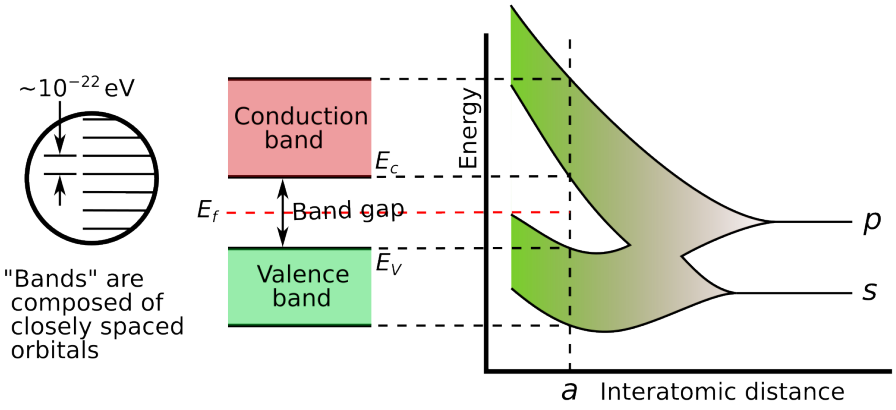

Figure 2.2: A hypothetical example of band formation for a large number of carbon lattices for diamond crystal. Adopted from Wikipedia, *Electronic band structure*, retrieved from `https://en.wikipedia.org/wiki/Electronic_band_structure`, accessed on 14 January 2025.

Roald Hoffmann has described in detail how chemistry and physics connect in the solid state. It's relatively easy to understand the chemical bonding and energy levels for molecular systems, but it is not easy in solids. The 'tight binding model' could describe the bonding in a solid, similar to the linear combination of atomic orbitals (LCAO) approach to construct the molecular orbital. The simplest example to understand the band structure in terms of atomic orbital is by considering the extended Hückel theory on a hydrogen polymer, shown in Figure 2.3.

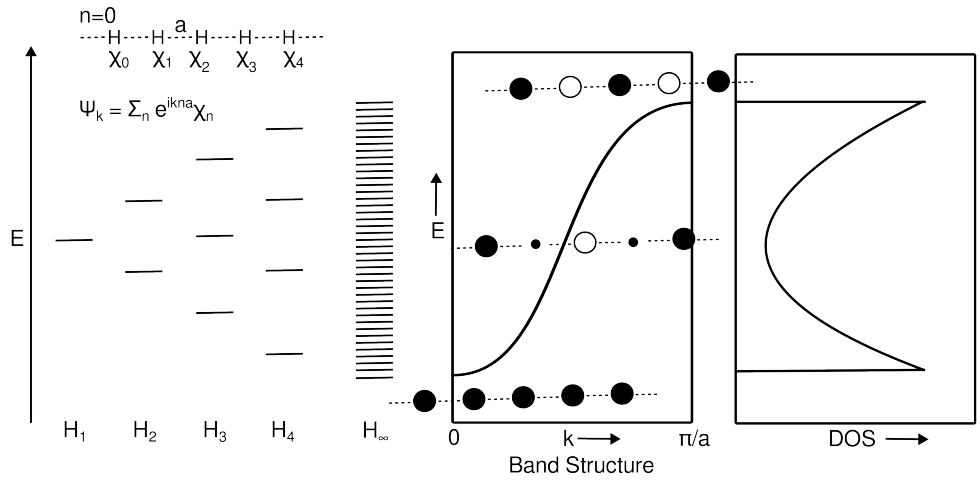

Figure 2.3: The band structure and DOS of the H atom chain.

The in-phase combination of 1s orbitals ($k = 0$) lies at the bottom of the band while the out-of-phase combination ($k = \frac{\pi}{a}$) is at the top.
The Density of States (DOS) is a useful concept for understanding the electronic structure of crystalline materials. The DOS describes the number of one-electron states in an infinitesimal energy interval dE;

$$DOS(E)dE = \text{ number of levels between } E \text{ and } E + dE \tag{2.6.1}$$

In general, $DOS(E)$ is proportional to the inverse of the slope of $E(k)$ vs k (band), the flatter the band, the greater the DOS at that energy. In the region of k-space where the band energy $E(k)$ varies slowly (in this case, near the edge of the Brillouin zone), there are many electronic states in small energy intervals (dE), therefore large peaks in DOS, whereas in the middle it is the opposite. The density-of-states curve counts levels and the integral of DOS up to the Fermi level is the total number of occupied MOs, multiplied by two gives the total number of electrons. Therefore, the DOS curve plots the distribution of electrons in energy and represents the return from reciprocal space (k) to real space. The DOS is an average over the Brillouin zone, over all k that might give molecular orbitals at the specified energy. Therefore, both MOs and DOS are interconnected. In periodic calculations, the wavefunction is constructed from delocalised plane wave basis functions. This wavefunction describes delocalised electrons interacting with ionic centres, formed of nuclei and their core electrons. To understand the chemical behaviour and trends, we need to extract the properties of individual atoms from our calculation. Common examples include charge and spin densities, and the "projected density of states" (PDOS) which is the

DOS arising from a particular atom or atomic orbital. There is no single correct way to define an atom in a crystal, in quantum mechanical terms, so we must select a method for projecting the delocalised wavefunction onto the atoms.

2.7 Summary

In this section, I have summarised several methodologies and approximations, utilised throughout this thesis to calculate the energies of electronic wavefunctions. It started with the Born-Oppenheimer approximation, followed by the Slater determinant for many-body systems and the Hartree-Fock Theory. The density functional theory has been discussed briefly with different functionals. Both atomic and plane wave basis sets have been introduced, and analytical methods are discussed for chemical bonding. Finally, a brief discussion about the electronic band structure and DOS in solids has been introduced.

Chapter 3

Fundamental Studies of Electronic Structure and Bonding: Competition Between Metal-Metal and Metal-Sn Interactions in Zintl Clusters

In this chapter, I discuss three quite distinct but related studies of the structure and bonding of Sn-based Zintl clusters that contain one or more endohedral transition metals. The work described in sections 3.2 and 3.3 has been published in the '*Chinese Chemical Letters*' and '*Inorganics*' journals, respectively.[1,2]

The work in section 3.1 has been submitted for consideration in the '*Dalton Transactions*' journal. All sections of this chapter have been carried out in collaboration with the group of Professor Zhong-Ming Sun at Nankai University, and all experimental work (synthesis, spectroscopy and crystallography) was carried out there. The computational work described was performed by the author. The experimental work is described in as much detail as is necessary to explain the context of the calculations, but the author claims no credit for these aspects. In addition, the work in section 3.2 was carried out with a colleague in Oxford, Zisheng Li. In the initial stages, the author carried out the calculations on $[Fe_2Sn_4Bi_8]^{3-}$ while ZL independently did the work on $[Cr_2Sb_{12}]^{3-}$. Only whilst writing up this work we realised that the two clusters are, in fact, very closely related through their shared valence electron count, and it is for this reason that they are reported together.

3.1 Electronic Structure and Bonding in an Endohedral Zintl Cluster: $[RuSn_{12}]^{4-}$

3.1.1 Introduction

The family of endohedral Zintl clusters is already quite diverse. The inclusion of the *d*-block elements,[107,108] the lanthanides and the actinides[109–111] makes it more diverse and unique to apply in several fields of material science and catalysis.[112,113] But it is fascinating to study the fundamentals of the nature of the chemical bond between the metal and the cage.[114,115] These clusters are unique because of their electronic flexibility. Although strong bonding interactions between the cage and the endohedral atom are possible, they are not essential to the stability of the cluster. It is, therefore, possible to find a wide range of bond types within a closely related family of clusters. Numerous studies have been performed on their electronic structure using density functional theory as well as other wavefunction-based methods.[107,114,116–118]

Earlier endohedral Zintl ions contained metal ions with a closed-shell d^{10} configuration. Classic examples are the icosahedral $[Ni/Pd/Pt@Pb_{12}]^{2-}$ and bi-capped square antiprismatic $[Pt@Pb_{10}]^{2-}$, shown in the right column of Figure 3.1.[45] These deltahedra are based on triangular faces and highly connected vertices, and their geometries are straightforward to rationalise in terms of Wade's rules.[24] Each cluster has a total valence electron count of $4n + 12$ (60 and 52, respectively) where n is the number of vertices. Of these electrons, 10 can be assigned to the metal nd shell and the remaining $4n + 2$ electrons can belong to the cage with a *closo* structure.[24] The clusters are therefore straightforwardly formulated as $M^0@{Pb_{10/12}}^{2-}$. The distribution of electrons into metal- and cage-based sets becomes complicated when we move to the left in the *d* block, where the metal atom typically has fewer nd electrons and higher energy. In some cases, transfer of charge density from the metal into the vacant orbitals of the cage can cause subtle distortions to the deltahedral structure. For example, $[Mn@Pb_{12}]^{3-}$ cluster adopts D_{2h}-symmetry,[50] $[Rh@Sn_{12}]^{3-}$ is D_{3d}-symmetric[48] and $[Fe@Sn_{10}]^{3-}$ is C_{2v}-symmetric.[119] (Figure 3.1, central column). At the same time, in more extreme cases it can favour the adoption of entirely different, 3-connected architectures such as pentagonal prismatic $[M@Ge_{10}]^{3-}$ (M = Fe, Co),[41,120] and bi-capped pentagonal pyramids, $[Ru@Ge_{12}]^{3-}$,[121] and $[Ta@Ge_4As_8]^{3-}$[122] (Figure 3.1, left column). These 3-connected 'fullerene-like' architectures are typically associated with electron-precise counts. Electron-precise here means a total valence electron count at the cage of $5n$, according to the $5n$ rule. This can only be reached if we assume that some or all of the metal *d* electrons also contribute to the count at the cluster.

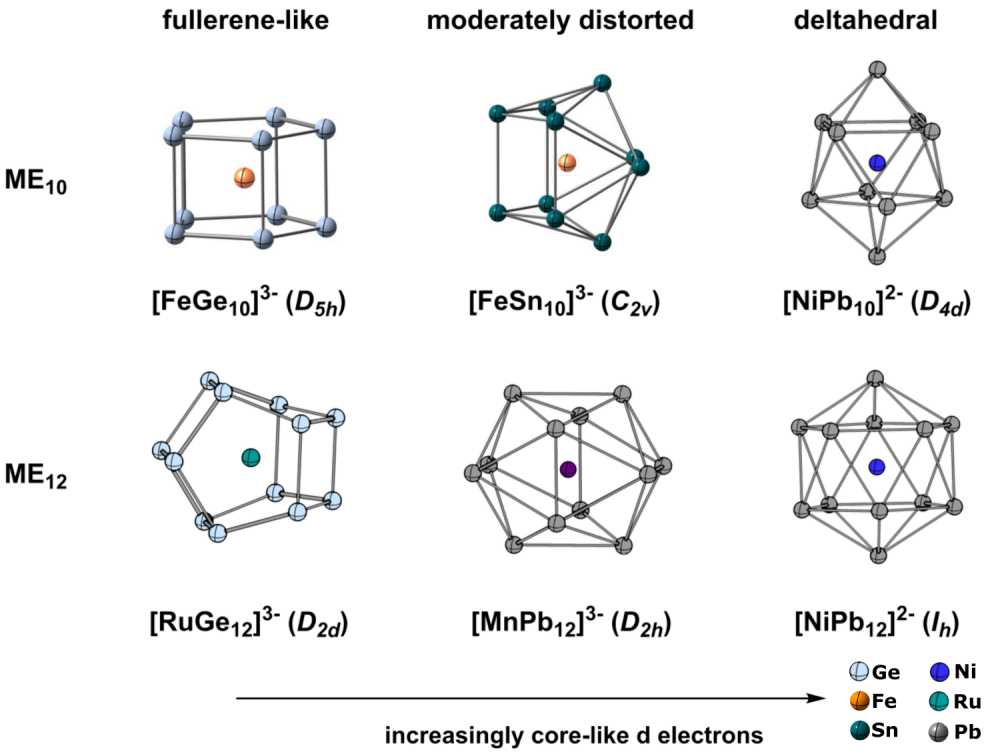

Figure 3.1: Structural trends within the $M@E_{10}$ and $M@E_{12}$ families.

This is slightly different from the deltahedral case, where the metal d electron contribution may not need to reach the characteristic $4n+2$ electron counting rule. For $[Ta@Ge_8As_4]^{3-}$, for example, the count for the $[Ge_8As_4]^{3-}$ unit is $8\times4+4\times5+3=55$, with the 5 valence electrons of Ta raising the total count to $5n=60$. This represents a marked departure from deltahedral cases such as $[Ni@Pb_{12}]^{2-}$ where the characteristic $4n+2$ electron count is reached without any contribution from the d electrons on the metal. The varying structural chemistry shown in Figure 3.1 indicates the different roles of metal d electrons that dictate the structure of the cluster, from a core-like inert deltahedron to a fullerene-like analogue.

In this section, we investigate the electronic structure and bonding of a new member of this family, $[Ru@Sn_{12}]^{4-}$, isoelectronic with both $[Rh@Sn_{12}]^{3-}$ and $[Pd@Sn_{12}]^{2-}$. Like its Rh counterpart, it is approximately icosahedral but with distinct low-symmetry distortions that reflect the lower effective nuclear charge of Ru compared to Rh and Pd. The structure is also strikingly different from that of $[Ru@Ge_{12}]^{3-}$, which adopts a fullerene-like architecture. We use density functional theory (DFT) to explore the origins of the structural trends in this intriguing family of clusters.

3.1.2 Computational Details

All DFT calculations were performed using the Amsterdam density functional (ADF) package, version 2021.104.[123] The exchange-correlation functional, proposed by Perdew, Burke and Ernzerhof (PBE)[124] was considered in all the calculations which are open-shell and the scalar relativistic effects were incorporated using the zeroth order relativistic approximation (ZORA).[125] Slater-type basis sets of polarised triple-zeta (TZ2P) were chosen, considering all electrons for all the atoms.[126] Given the flatness of the potential energy surface (*vide infra*), we have used a very fine numerical integration grid and applied convergence criteria on energies and forces that are a factor of 10 smaller than the defaults. The confining effect of the cation in a crystalline environment was approximated using a conductor-like screening model (COSMO, $\epsilon = 79.38$).[127] The choice of methods, basis sets, other parameters and solvation models are adopted from several previous studies conducted on Zintl clusters, mainly by our group.[2,48,128]

3.1.3 Results and Discussion

3.1.3.1 Structural Characterisation

Zhong-Ming Sun and co-workers have recently synthesised $[Ru@Sn_{12}]^{4-}$ Zintl ion stabilised by 4 $[K(2.2.2-crypt)]^+$ cations in ethylenediamine (en) solution. The crystal structure of the compound was analysed by using single-crystal X-ray diffraction. The asymmetric unit of $[K(2.2.2-crypt)]_4[Ru@Sn_{12}]$, **1**, and the structure of the $[Ru@Sn_{12}]^{4-}$ anion are shown in Figure 3.2, and key bond lengths are summarised in Table 3.1. The unit cell contains one cluster anion, four $[K(2.2.2)\,crypt]^+$ cations and two ethylenediamine (en) molecules, with the shortest K^+-Sn contacts in excess of 6.5 Å. The anion adopts an approximately I_h-symmetric architecture, very similar to those of the isoelectronic clusters $[Rh@Sn_{12}]^{3-}$ and $[Pt@Pb_{12}]^{2-}$.[48,49] The average Ru–Sn bond length of 2.90 Å is considerably longer than those in the other known binary Ru/Sn cluster, $[Ru@Sn_9]^{6-}$ (2.64–2.70 Å), probably a consequence of the intrinsically smaller radius of the Sn_9 cage, but also longer than those in binary alloy phases (2.60–2.80 Å) and in clusters where the Ru is *exo*-, rather than endohedral, with respect to a Sn_n clusters such as $[Sn_{19}\{Ru(COD)(en)\}_2]^{4-}$ (2.678–2.794 Å),[129] $[Sn_{20}\{Ru(COD)\}_2]^{6-}$ (2.683–2.767 Å).[130] There are, however, some striking distortions of the icosahedron in $[Ru@Sn_{12}]^{4-}$ that lower the point symmetry from I_h to C_i. The 12 Ru-Sn bonds separate into six symmetry-distinct, mutually *trans*, pairs, the shortest of which is 2.79 Å, the longest 3.03 Å and the bond distance varies over a

range of 0.24 Å. The 20 Sn-Sn bonds are similarly separated into 10 symmetry-related pairs with bond lengths spanning 0.18 Å from the shortest (2.94 Å) to the longest (3.12 Å). Distortions from perfect I_h symmetry are also apparent in $[Rh@Sn_{12}]^{3-}$, but they are much less pronounced: the Rh-Sn bond lengths vary over a range of 0.08 Å, from 2.87 Å to 2.95 Å, while the bonded Sn-Sn distances vary between 3.04 Å and 3.13 Å. The group 10 clusters, $[Ni@Pb_{12}]^{2-}$, $[Pd@Pb_{12}]^{2-}$ and $[Pt@Pb_{12}]^{2-}$, are also closer to perfect icosahedral symmetry, with the M-Pb and Pb-Pb bonds distributed over 0.11 Å and 0.07 Å, respectively.

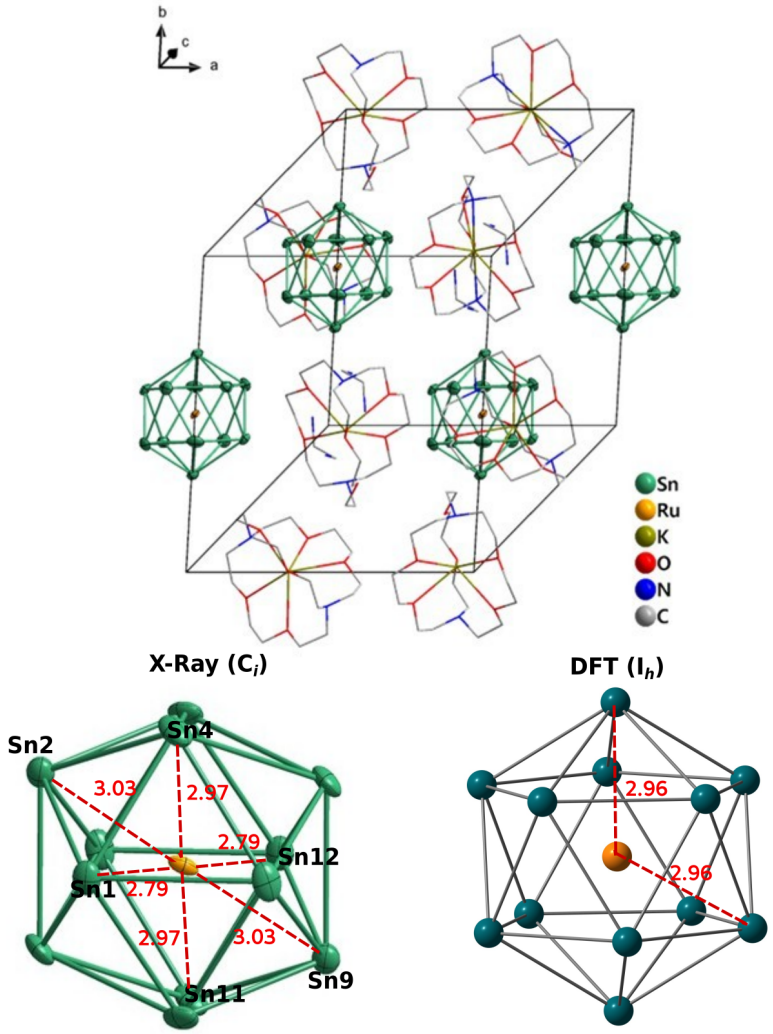

Figure 3.2: Unit cell of $[K(2.2.2-crypt)]_4[Ru@Sn_{12}]$, **1** and the structure (both X-ray and DFT) of the anion $[Ru@Sn_{12}]^{4-}$

Table 3.1: Crystallographic and DFT-optimised bond lengths (all values in Å), relative energies (E_{rel} against the respective I_h symmetric geometry and number of imaginary frequency (N_{imag}) for members of the M@E_{12} family .

		M-E	**E-E**	N_{imag}	E_{rel}(eV)	**ref**
$[\mathbf{Ru@Sn_{12}}]^{\mathbf{4-}}$	X-ray (C_i)	2.79-3.03	2.94-3.12			This work
	DFT (I_h)	2.96	3.11	0	0.0	
	DFT (D_{2d})	3.04-3.12	2.85-2.96	0	+1.07	
$[\mathbf{Rh@Sn_{12}}]^{\mathbf{3-}}$	X-ray (D_{3d})	2.87-2.95	3.04-3.13			[48]
	DFT (I_h)	2.96	3.12	0	0	
	DFT (D_{2d})	3.01-3.14	2.83-2.99	0	+1.79	
$[\mathbf{Pd@Pb_{12}}]^{\mathbf{2-}}$	X-ray	2.98-3.09	3.13-3.20			[45]
	DFT (I_h)	3.09	3.25	0	0.0	
	DFT (D_{2d})	3.12-3.32	2.97-3.14	2	+3.71	
$[\mathbf{Pt@Pb_{12}}]^{\mathbf{2-}}$	X-ray	3.06(av.)	3.05-3.22			[49]
	DFT (I_h)	3.09	3.25	0	0	
$[\mathbf{Ru@Ge_{12}}]^{\mathbf{3-}}$	X-ray (D_{2d})	2.67-2.77	2.44-2.60			[53]
	DFT (I_h)	2.66	2.80	2	0	
	DFT (D_{2d})	2.71-2.78	2.48-2.62	0	-1.27	
$[\mathbf{Ru@Ge_{12}}]^{\mathbf{4-}}$	DFT (I_h)	2.66	2.80	5	0	
	DFT (D_{2d})	2.73-2.75	2.49-2.65	0	-0.95	
$[\mathbf{Mn@Pb_{12}}]^{\mathbf{3-}}$	X-ray (D_{2h})	2.87-3.30	3.10-3.74			[50]
	DFT (I_h)	3.09	3.25	0	0	
	DFT (D_{2h})	2.90-3.20	3.15-3.42	0	-0.65	
	DFT (D_{2d})	3.22-3.40	2.98-3.10	5	+2.38	
$[\mathbf{Au@Pb_{12}}]^{\mathbf{3-}}$	X-ray (D_{3d})	2.84-3.09	3.10-3.25			[52]
	DFT (I_h)	3.15	3.31	0	0	
	DFT (D_{3d})	1.54-1.73	3.14-3.60	0	-0.66	
	DFT (D_{2d})	3.06-3.55	3.16-3.82	3	+0.25	

3.1.3.2 Electronic Structure

In surveying the singlet potential energy surface of $[Ru@Sn_{12}]^{4-}$, we have started from a perfectly icosahedral geometry and also from a range of similar structures with small distortions imposed along the C_5, C_3 and C_2 axes. We have also initialised calculations from the X-ray geometry (C_i point symmetry). In anticipation of a rather flat potential energy surface, we have imposed tight geometry convergence criteria, and have used a very fine integration grid to avoid artifacts due to numerical noise. All of the above calculations, however, converged on the same perfectly icosahedral structure, indicating that the distortions observed in the crystallographic data must be a consequence of the periodic lattice (the averaged effect of which is modelled by a high dielectric continuum in our calculations) rather than an intrinsic electronic driving force. In the previous study of isoelectronic $[Rh@Sn_{12}]^{3-}$, it was concluded that the crystallographic data show distortions of the icosahedron (in this case approximately D_{3d}-symmetric) despite the presence of only a single, perfectly icosahedral, minimum on the potential energy surface. Bürgi and Dunitz have established the principle of structural correlation, wherein a molecule can be deformed by the lattice along low-frequency modes.[131] In both $[Ru@Sn_{12}]^{4-}$ and $[Rh@Sn_{12}]^{3-}$, the preferred distortion coordinate appears to reflect the arrangement of cations in the unit cell: in the title compound **1**, for example, the $P\bar{1}$ space group imposes a centre of symmetry at the Ru center, and the 16 nearest neighbour K^+ ions are distributed in pairs around this center (Figure 3.3). In $[Rh@Sn_{12}]^{3-}$, in contrast, the 12 nearest neighbour K^+ ions have approximate trigonal symmetry, and the anion is distorted to an approximately D_{3d}-symmetric geometry. These observations suggest that the icosahedra have several low-frequency modes along which the cluster can distort, according to the particular arrangement of cations in the lattice.

The computed vibrational spectrum of $[Ru@Sn_{12}]^{4-}$ shows two allowed t_{1u} symmetric modes at 117 cm^{-1} and 155 cm^{-1} which correspond to the bands at 74 cm^{-1} and 102 cm^{-1} computed for $[Pt@Pb_{12}]^{2-}$ by Cetin and co-workers.[132] The 74 cm^{-1} mode has been observed in the experimental FTIR spectrum, while the 102 cm^{-1} mode has been tentatively assigned to a shoulder at 118 cm^{-1}. Of more direct relevance to the low-symmetry distortions in $[Ru@Sn_{12}]^{4-}$ are the low-frequency modes which have gerade symmetry (h_g), meaning that the inversion center is retained during the displacement. The distortions to D_{3d} and C_i symmetry observed in the crystal structures of $[Rh@Sn_{12}]^{3-}$ and $[Ru@Sn_{12}]^{4-}$, respectively, both retain the inversion center, and can be reached by distortion along the soft h_g mode. The frequency of this h_g mode decreases in the order $Sn_{12}{}^{2-}$ (68 cm^{-1}) > $[Rh@Sn_{12}]^{3-}$ (45 cm^{-1})

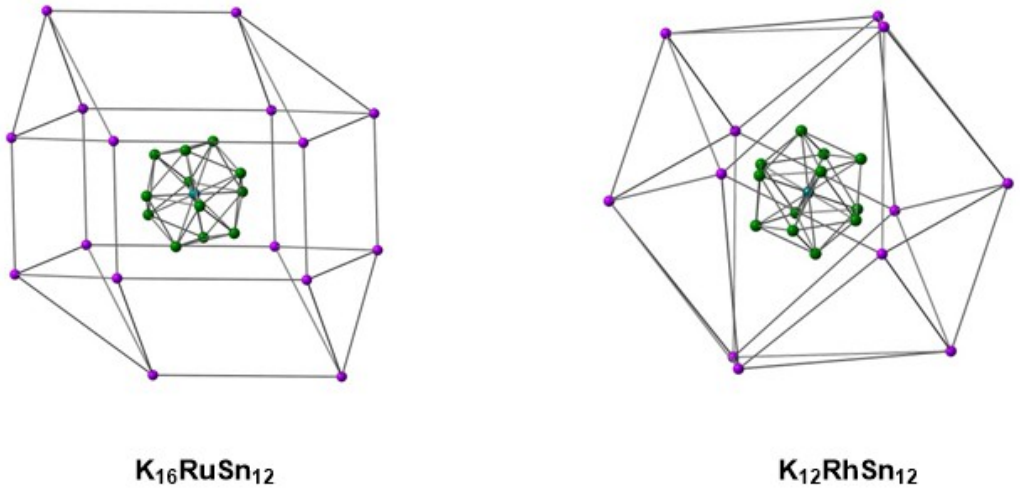

Figure 3.3: Disposition of the $[Ru@Sn_{12}]^{4-}$ and $[Rh@Sn_{12}]^{3-}$ anions in relation to the surrounding K^+ ions in the lattice.

> $[Ru@Sn_{12}]^{4-}$ (16 cm^{-1}), and the very soft mode in the latter clearly allows for a stronger response to the asymmetric cation environment. The trend in vibrational frequencies correlates with the increasing ability of the transition metal to donate electron density into the vacant orbitals of the Sn_{12} cage. In strict I_h symmetry the $4d$ orbitals of the transition metal have h_g symmetry so the acceptor orbital on the cage must be the h_g-symmetric LUMO+1, and the projected DOS and overlap-population based DOS for $[Ru@Sn_{12}]^{4-}$ in Figure 3.4 shows a small amount of Ru $4d$ character (orange colour) in this orbital, $\sim$ 2 eV above the Fermi level. Distorting to the C_i-symmetric geometry allows mixing of the components of the g_g symmetric LUMO and the h_g-symmetric LUMO+1, and a small amount of $4d$ character begins to accumulate in the LUMO at $\sim$ 0.5 eV. The distortions from I_h symmetry make the Sn_{12} cage a more effective electron-acceptor by allowing the LUMO, rather than the LUMO+1, to participate in back-bonding.

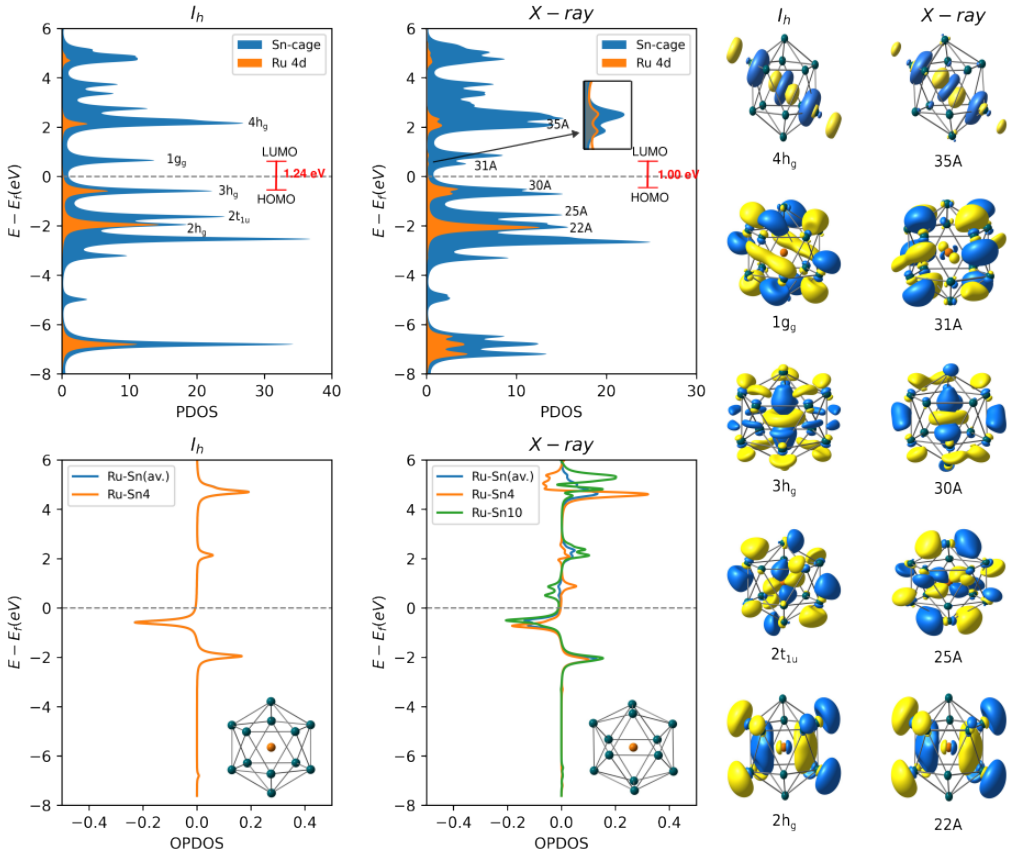

Figure 3.4: Projected Density of States (PDOS) and Overlap Population Density of States (OPDOS) and for the spin-α manifold of $[Ru@Sn_{12}]^{4-}$ in I_h (left) and at the C_i-symmetric geometry of the X-ray structure. The Fermi level, E_f, is defined as the mid-point between the HOMO and the LUMO.

The very low value of the h_g-symmetric mode for $[Ru@Sn_{12}]^{4-}$ indicates that the anion lies on the cusp of structural instability, even in the absence of a low-symmetry lattice. It is, therefore, instructive to compare it to the Ge cluster, $[Ru@Ge_{12}]^{3-}$, which adopts an entirely different D_{2d}-symmetric architecture where the vertices of the Ge_{12} cage are 3-connected. It was argued that this 'fullerene-like' architecture reflects the presence of greater electron density on the E_{12} unit (compared to the alternative icosahedral arrangement), and so we anticipate that the stability of the D_{2d} structure should also correlate with the tendency of the icosahedra to distort discussed in the previous paragraph. A plot of the relative energies of the I_h- and D_{2d}-symmetric isomer is shown in Figure 3.5 confirms this prediction: the D_{2d}-symmetric structure is less stable than I_h for all the Sn clusters, but the gap narrows as the metal becomes more electron-rich, and $[Ru@Sn_{12}]^{4-}$ lies only 1 eV below the crossover point. Extrapolating further, the next member of the isoelectronic series, $[Tc@Sn_{12}]^{5-}$ sits

almost exactly on the intersection of the I_h and D_{2d} curves, and the h_g-symmetric mode of the icosahedron is now imaginary ($52i$ cm^{-1}). It is likely, therefore, that this cluster will exhibit dynamic behaviour as a result of the accidental degeneracy of different structural types.

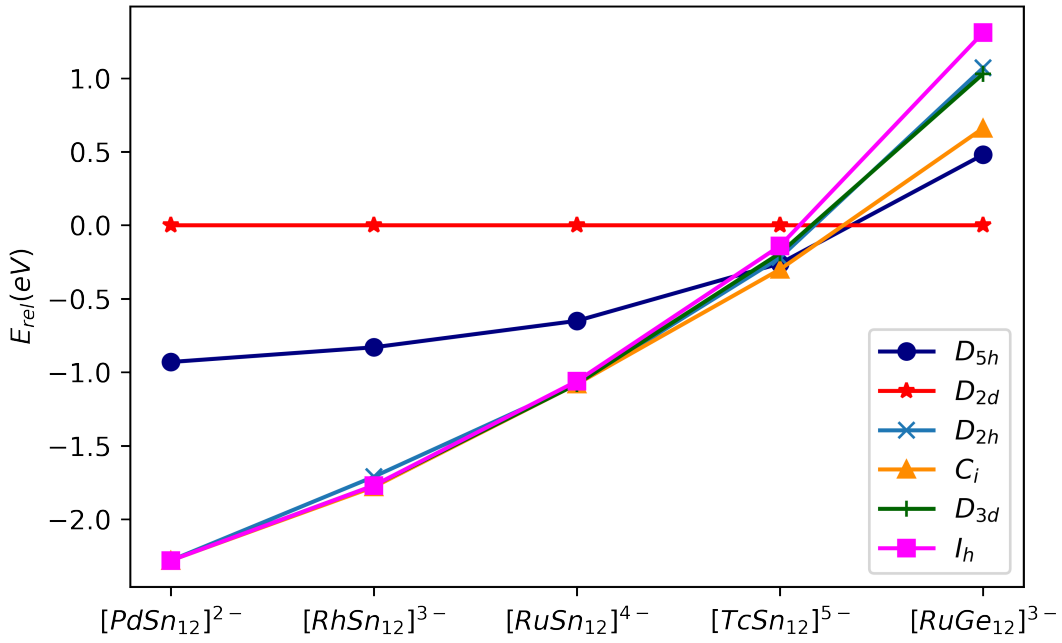

Figure 3.5: Relative energies of the I_h-symmetric (with sub-groups), D_{5h}-symmetric and D_{2d}-symmetric isomers of M@E$_{12}$ family.

3.1.4 Conclusions

In this work, we have explored the structure of a new member of the endohedral icosahedral family, [Ru@Sn$_{12}$]$^{4-}$. Analogues containing group 9 or group 10 metals (Rh, Ni, Pd, Pt) are well known, but this work represents the first encapsulation of a group 8 metal into a [Sn$_{12}$] cage. The more electron-rich metal is better able to engage in back-bonding to the cage, which softens the lowest frequency h_g-symmetric vibrational mode, to the point where it is only 16 cm^{-1} in [Ru@Sn$_{12}$]$^{4-}$. This softness makes the cluster anion very susceptible to low-symmetry deformations in response to the arrangement of cations in the lattice, and indeed the X-ray structure shows very pronounced distortions to a C_i symmetric geometry. The rhodium analogue, [Rh@Sn$_{12}$]$^{3-}$, is also distorted, but to a lesser extent due to the greater effective

nuclear charge of the metal. In the following section, I move on to a system where the transfer of electron density from metal to Sn is much more pronounced.

3.2 Electronic Structure and Metal-Metal Bonds in Zintl Clusters: $[Fe_2Sn_4Bi_8]^{3-}$ and $[Cr_2Sb_{12}]^{3-}$

3.2.1 Introduction

The families of $M@E_{10}$ and $M@E_{12}$ clusters are well established in contrast to the relatively small number of examples in the literature of clusters containing dimeric units, $M_2@E_n$, or even larger metal fragments, $M_3@E_n$ or $M_4@E_n$.[133] We have briefly discussed about the electron counting rules for different families of clusters in Chapter 1. The possibilities of metal-metal bonding in these clusters introduce a further dimension to the problem. The covalent bonds between the metal centers may promote the release of electron density from M-M antibonding states onto the cage and *vice versa*. The electronic structure of silicon- and germanium-based clusters such as Mn_2Si_{12},[134–137] may be easy to compute but experimental characterisations are restricted, especially the neutral or cationic clusters.[138–142] Several attempts have been made by researchers to note the general pattern of structural trends for the endohedral clusters $M@E_{12}$ and $M@E_{10}$ and the role of the transition metal atom. Metal-metal bonding plays a crucial role in the extended family of endohedral M_2 clusters, equivalent to the $M@E_{12}$ and $M@E_{10}$ clusters in single-metal analogues. Some of the examples of the triple-decker E_{12} architectural clusters are $[Ni_2Bi_{12}]^{4+}$,[143] and also the mixed Sn/Pb/Sb/Bi clusters $[Ni_2Sn_7Sb_5]^{3-}$, $[Ni_2Sn_7Bi_5]^{3-}$, $[Ni_2Pb_7Bi_5]^{3-}$ and $[Co_2Sn_5Sb_7]^{3-}$.[57–59] These might have the potential to fill this void because the prolate architecture is ideally suited to accommodate an M_2 dimer, just as the icosahedron is ideally suited for a single metal atom. All of the Ni and Co clusters mentioned above are rather similar, in terms of the geometry and the valence electron counts. They share a common valence electron count of 76, and all show approximate D_{4h} point symmetry (in some cases, with slight distortion) and similar M-M distances of ~ 2.45 Å.

In this section, we report the electronic structure characterisation of two new open-shell members of the $M_2@E_{12}$ family, $[Fe_2Sn_4Bi_8]^{3-}$ and $[Cr_2Sb_{12}]^{3-}$, (Figure 3.6) both of which have a valence electron count of 75, one fewer than the Ni/Co clusters described above. Both of the clusters have been experimentally synthesised and characterised by our experimental collaborator Z.M-Sun and co-workers from China. $[Fe_2Sn_4Bi_8]^{3-}$ retains the D_{4h}-symmetric geometry, the same as the 76-electron clusters but $[Cr_2Sb_{12}]^{3-}$ has a very different C_{4v}-symmetric geometry where some of the Sb-Sb bonds are substantially elongated. We use density functional theory to place the diverse structural chemistry of this family into context and argue

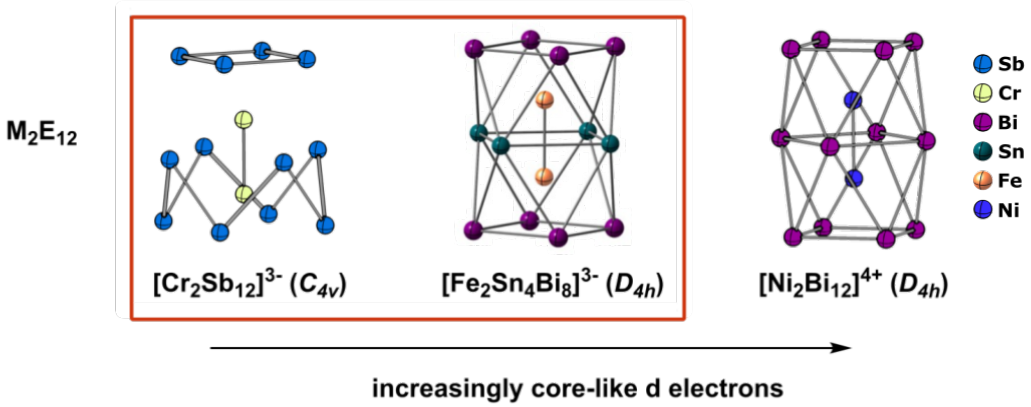

Figure 3.6: Structural trends within M_2E_{12} families. The two new clusters reported in this section are highlighted in the box.

that $[Fe_2Sn_4Bi_8]^{3-}$ and $[Cr_2Sb_{12}]^{3-}$ are the dimeric analogues of slightly distorted $[MnPb_{12}]^{3-}$ and fullerene-like $[RuGe_{12}]^{3-}$, respectively, just as the 76-electron Ni and Co clusters are analogues of $[PtPb_{12}]^{2-}$.

3.2.2 Computational Details

All calculations described in this section were performed with the Amsterdam Density Functional (ADF) package, version 2021.104.[123] The exchange-correlation functional proposed by Perdew, Burke and Ernzerhof (PBE)[124] was used throughout, and scalar relativistic effects were introduced using the Zeroth Order Regular Approximation (ZORA).[125] The sensitivity of the results to the choice of functional was tested by also performing calculations using the M06-L[144] and hybrid PBE0 functionals.[93] For all geometry optimisations, a triple-zeta quality basis set of Slater-type orbitals was used, supplemented by two sets of polarisation functions ('TZ2P').[126] All electrons were included in the basis set. A 'good' setting of the numerical grid was used in all calculations.[145] The Conductor-like Screening Model (COSMO, ϵ= 78.39) was applied to simulate the confined effects of the crystalline environment.[127] All SCF procedures were conducted using the default setting of ADF: at convergence, the commutator of the Fock matrix and the density matrix is less than 10^{-6}.

3.2.3 Results and Discussion

3.2.3.1 Structural Characterisation

From the X-ray crystallographic data (received from the experimental collaborator as mentioned above) we extract the asymmetric unit of $[K(2.2.2-crypt)]_3[Fe_2Sn_4Bi_8]$

(**2**) and the structure of the $[Fe_2Sn_4Bi_8]^{3-}$ anion, shown in Figure 3.7. The key bond lengths of both X-ray structures and calculated geometries are summarised in Table 3.2. The asymmetric unit contains a single $[Fe_2Sn_4Bi_8]^{3-}$ anion along with three $[K(2.2.2-crypt)]^+$ cations, with the shortest K^+-Bi distance of 6.5 Å. The anion adopts a D_{4h}-symmetric triple-decker architecture, very similar to those of the 76-electron Ni_2 and Co_2 clusters described in the introduction. The Fe-Fe separation of 2.395 Å is marginally shorter than the Co-Co and Ni-Ni analogues ($\sim$ 2.45Å).[57–59,143] The average Sn-Sn bond length in the equatorial plane is 3.373 Å, somewhat longer than the corresponding values of 3.264, 3.290 and 3.298 Å for $[Ni_2Sn_7Sb_5]^{3-}$, $[Ni_2Sn_7Bi_5]^{3-}$ and $[Co_2Sn_5Sb_7]^{3-}$, respectively. The average Fe-Sn bond length of 2.669 Å is also $\sim$0.03 Å longer than the corresponding values for three 76-electron clusters. The Fe-Bi and Bi-Bi bond lengths (average 2.697 Å and 3.095 Å, respectively) are marginally longer than those in $[Ni_2Bi_{12}]^{4+}$ (2.678 Å and 3.045 Å, respectively).

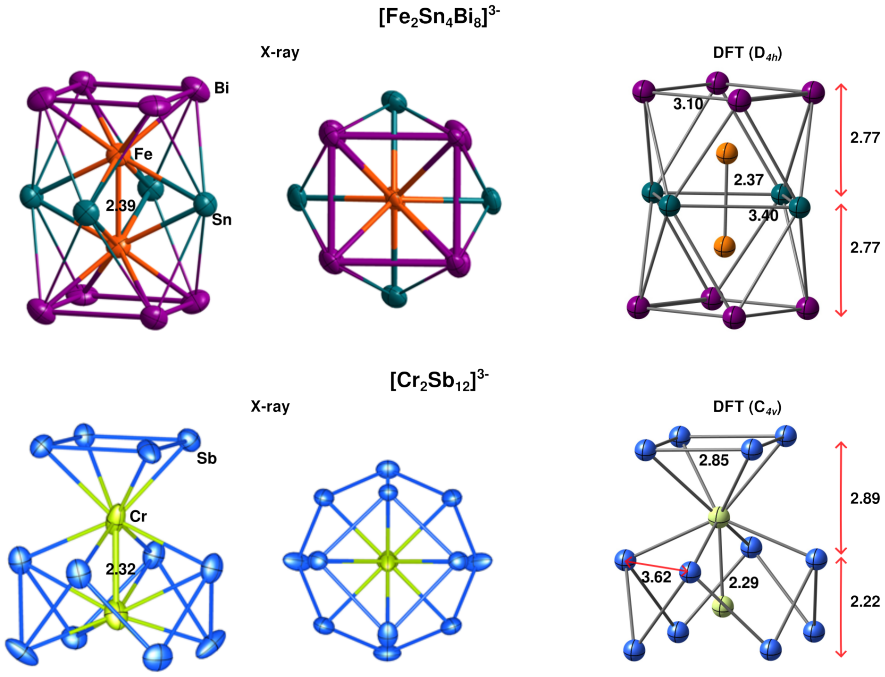

Figure 3.7: X-ray and DFT structures of the 75-electron anions $[Fe_2Sn_4Bi_8]^{3-}$ and $[Cr_2Sb_{12}]^{3-}$ (side and top views).

Similarly, the asymmetric unit of $[K(18\text{-crown}-6)]_4[Cr_2Sb_{12}] \cdot Cp$, **3**, contains one $[Cr_2Sb_{12}]^{3-}$ anion along with a single Cp^- unit and four $[K(18\text{-crown}-6)]^+$ cations. The bond lengths are summarised in Table 3.2. The cluster anion in **3** is significantly distorted from D_{4h} to C_{4v}-symmetry and can be considered as separate $CrSb_8$ and

Table 3.2: Total valence-electron count (VE) and crystallographic and DFT-optimised bond lengths for members of the $M_2E_4E'_8$ family (all values in Å).

	VE		M-M	M-E	M-E′	E-E	E′-E′	E-E′	ref
$[\mathbf{Fe_2Sn_4Bi_8}]^{\mathbf{3-}}$	75	X-ray	2.39	2.67	2.69	3.37	3.09	3.29	This work
		DFT (D_{4h})	2.37	2.68	2.71	3.40	3.10	3.30	
$[\mathbf{Cr_2Sb_{12}}]^{\mathbf{3-}}$	75	X-ray	2.32	2.78	2.757	3.61	2.75	3.55	This work
				2.83	2.74		3.72	2.80	
		DFT (D_{4h})	2.16	2.79	2.64	3.64	3.19	3.09	
		DFT (C_{4v})	2.29	2.78	2.77	3.62	2.85	3.51	
				2.83	2.73		3.65	2.87	
$[\mathbf{Ni_2Bi_{12}}]^{\mathbf{4+}}$	76	X-ray	2.43	2.68	2.74	3.37	3.04	3.39	[143]
		DFT (D_{4h})	2.45	2.69	2.75	3.39	3.06	3.416	
$[\mathbf{Ni_2Sn_7Bi_5}]^{\mathbf{3-}}$	76	X-ray	2.44	2.63	2.66	3.29	3.01	3.30	[58]
$[\mathbf{Ni_2Pb_7Bi_5}]^{\mathbf{3-}}$	76	X-ray	2.49	2.71	2.71	3.40	3.06	3.35	[57]
$[\mathbf{Ni_2Sn_7Sb_5}]^{\mathbf{3-}}$	76	X-ray	2.43	2.61	2.59	3.26	2.89	3.27	[59]
$[\mathbf{Co_2Sn_5Sb_7}]^{\mathbf{3-}}$	76	X-ray	2.41	2.62	2.57	3.29	2.88	3.25	[59]

$CrSb_4$ fragments (Figure 3.7, in the first instance. Although the Sb-Sb distance of only 3.549 Å between the atoms of the Sb_4 and Sb_8 units suggests that this separation is not entirely clearcut. The $CrSb_8$ unit is similar to the $[MAs_8]^{q-}$ and $[MSb_8]^{q-}$ anions (M = Nb, Ta, Cr, Mo) which have the same crown-like E_8 motif.[146] The Cr-Cr bond length is 2.319 Å, even shorter than the Fe-Fe bond in $[Fe_2Sn_4Bi_8]^{3-}$. The average Sb-Sb bond length within the Sb_8 crown is 2.801 Å, typical of Sb-Sb single bonds, while the remaining Sb_4 unit is a distorted square with bond lengths between 2.75 and 2.76 Å (average 2.755 Å). For comparison, the computed Sb-Sb distance for gas-phase *cyclo*-Sb_4^{2-} is 2.82 Å, in sandwich complexes of Sb_4^{2-} reported by S. Li and co-workers.[147] The $[Cr_2Sb_{12}]^{3-}$ anion is sandwiched between two of the $[K(18\text{-crown}-6)]^+$ cations which are aligned along the approximate 4-fold rotation axis, with K-Sb distances in the range 3.23-3.72 Å (to $CrSb_4$) and 4.26-4.66 Å (to the lower face of $CrSb_8$). The alignment of cations along the principal axis is similar to the packing in the one-dimensional $^1_\infty[RbNbAs_8]^{2-}$ chains in Rb_3NbAs_8.[148] The other two cations sandwich the Cp^- anion. The absence of bonds between the central and upper Sb_4 units in the Cr_2 system emphasises the differences between the two clusters. Their structures are in fact closely related, the Sb-Sb distances between the upper and central Sb_4 units are only 0.75 Å longer than those between the central and lower Sb_4 units (3.549 Å *vs* 2.801 Å).

3.2.3.2 Electronic Structure

We have encompassed the electronic structure of the two new clusters along with the whole family of closely related examples set out in Table 3.2 where we have highlighted the total valence electron count, including the transition metal 3*d* electrons, as a central variable. Interestingly, these two new 75-electron clusters **1**,**2** are clearly

more electron-deficient than their 76-electron analogues. The reason could be that an orbital does not have stability in the earlier transition metals and the electron density on the M_2 fragment is more accessible to the cage for Fe and particularly for Cr, than for Ni. The effect of changing the transition metal from Fe to Cr is combined with the change in *p*-block element from a group 14 element (Sn) in **1** to a more electronegative group 15 element (Sb) in **2** on the equatorial plane, might also have the effect of drawing electron density away from the metal. A good starting point for our analysis is therefore to consider the 76-electron Ni_2 clusters, $[Ni_2Bi_{12}]^{4+}$, $[Ni_2Sn_7Bi_5]^{3-}$, $[Ni_2Pb_7Bi_5]^{3-}$ and $[Ni_2Sn_7Sb_5]^{3-}$, where the 3*d* electrons are the most core-like, in the same way that we have used $[NiPb_{12}]^{2-}$ as a reference point in the icosahedral family.[50,118,149] We choose $[Ni_2Bi_{12}]^{4+}$ to illustrate the key points, simply because it has the same point symmetry as $[Fe_2Sn_4Bi_8]^{3-}$ (D_{4h}), and therefore it would be easy to understand and make a fair comparison.

3.2.3.3 76-electron $[Ni_2Bi_{12}]^{4+}$: A Natural Reference Point

The ground state of $[Ni_2Bi_{12}]^{4+}$ is a spin-singlet with DFT-optimised structural parameters in close correspondence with the X-ray data and also the computational work reported in reference[143] (Table 3.2). Figure 3.8 shows three complementary perspectives on the electronic structure of this cluster: (a) the Kohn-Sham molecular orbital array, (b) the density of states (PDOS), projected onto Ni 3*d*, Bi 6*s* and Bi 6*p*, and, finally, (c) the Overlap Population-based Density of States (OPDOS), sometimes referred to as the Crystal Orbital Overlap Population (COOP) in a solid-state context.

The OPDOS indicates whether states at a given energy have bonding (positive OPDOS) or anti-bonding (negative OPDOS) character with respect to specific pairs of atoms. The PDOS shows that almost all the Ni 3*d* characters (green) accumulate below the Fermi level, and the Ni-Ni OPDOS shows that these levels range from π bonding ($3e_u$ with positive OPDOS) at the bottom to σ antibonding ($4a_{2u}$) near the top, and the computed Mayer bond order of 0.452 confirms the absence of significant Ni-Ni bonding, as noted by Ruck et al. in their original report of this cluster.[143] All the above is consistent with a formulation as $Ni_2{}^0@Bi_{12}{}^{4+}$, the analogue $Ni^0@Pt_{12}{}^{2-}$.

The HOMO-LUMO gap in $[Ni_2Bi_{12}]^{4+}$ is significantly large (1.77 eV) and we find a large gap in the isolated $Bi_{12}{}^{4+}$ cation as well (1.44 eV). This observation indicates that the triple-decker geometry is suited to accommodate precisely 56 valence electrons. Dehnen and co-workers have noted that capping the two square faces of $[Sn_7Bi_5]^{3-}$ (isoelectronic with $Bi_{12}{}^{4+}$) would generate an approximately deltahedral

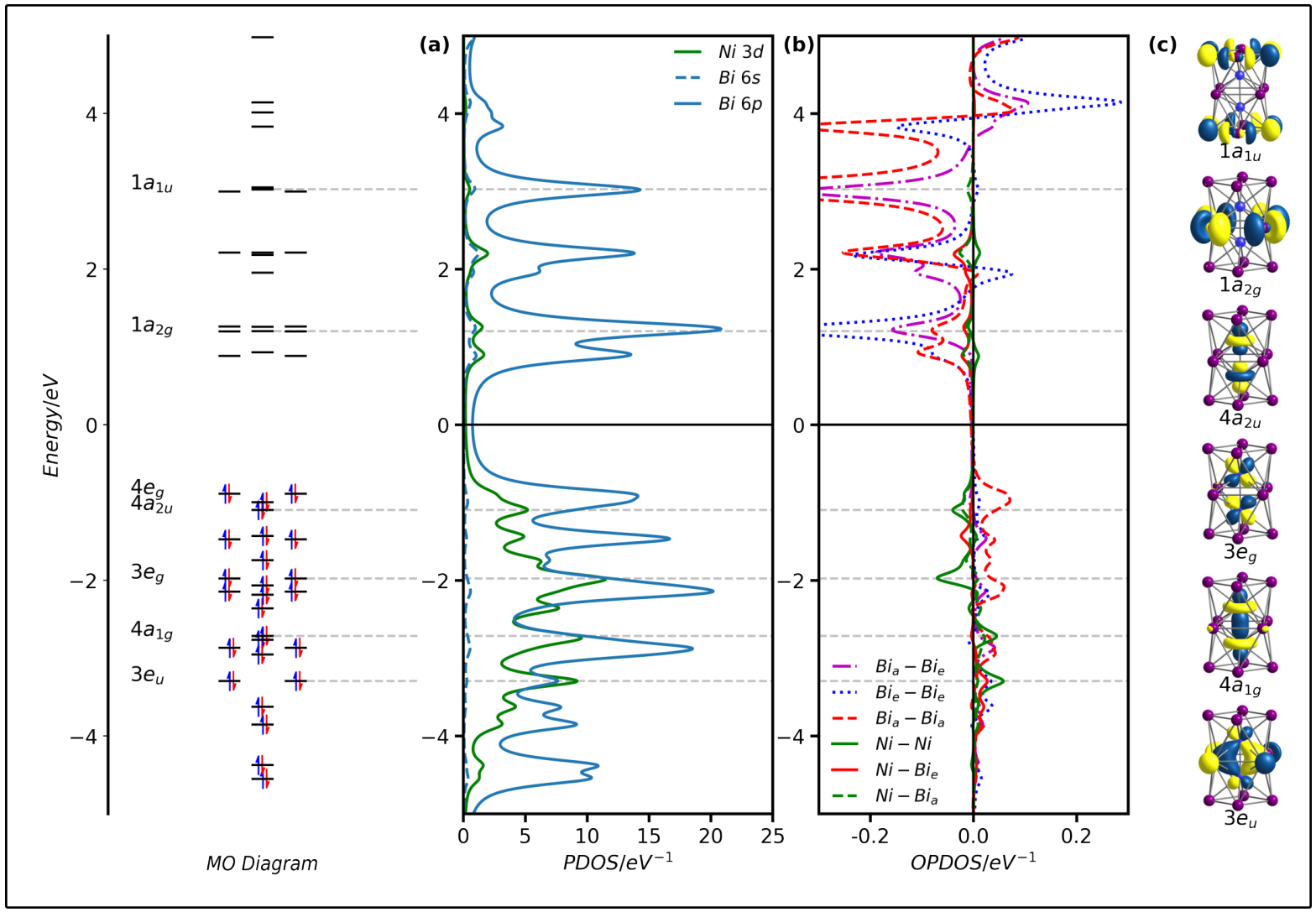

Figure 3.8: Kohn-Sham orbitals, Projected Density of States (PDOS) and Overlap Population Density of States (OPDOS) of $[Ni_2Bi_{12}]^{4+}$. The Fermi level, E_f, is defined as the mid-point between the HOMO and the LUMO. Bi_a and Bi_e indicate axial and equatorial Bi atoms, respectively.

14-vertex structure, in which case the E_{12} geometry should be classed as *arachno* with a natural electron count of $4n + 6 = 54$, not 56.[24,58] Jemmis' 'mno' rules[31] offer a different perspective. If the cluster is viewed as two square antiprisms fused *via* a shared square face (rather than a single 12-vertex polyhedron), the predicted count is $4n + 2m + 2o = 48 + 4 + 4 = 56$, where m, n and o are the number of fused polyhedra (2), the number of vertices (12) and the number of open faces (2), respectively. The difference of 2 in the two electron-counting schemes arises from the assumed presence of 2 strongly bonding internally directed hybrids (1 per polyhedron) in the Jemmis scheme but only 1 in the single polyhedron according to the Wade scheme. The deviation from Wade's rules is therefore a natural consequence of the prolate rather than spherical structure of the cluster. No matter how we choose to rationalise the 56-electron count, the important point is that it is the 'natural' one for triple-decker E_{12} clusters because it generates a large HOMO-LUMO gap, just as $4n + 2 = 50$ is the 'natural' count for the icosahedral geometry and $5n = 60$ is the 'natural' count for the fullerene-like geometry in $[TaGe_4As_8]^{3-}$.[121,122]

3.2.3.4 75-electron $[Fe_2Sn_4Bi_8]^{3-}$.

The ground state of the 75-electron $[Fe_2Sn_4Bi_8]^{3-}$ cluster is a doublet ($^2A_{2u}$) with optimised Fe-Fe, Sn-Sn, Sn-Bi and Bi-Bi bond lengths that are within 0.03 Å of the crystallographically-determined values (Table 3.2). The spin-α and spin-β Kohn-Sham eigenvalues, PDOS and OPDOS plots are shown in Figure 3.9.

Compared to the $[Ni_2Bi_{12}]^{4+}$ reference, one electron has been removed from the spin-β component of the Fe-Fe σ^* orbital, $4a_{2u}$, which now lies above the Fermi level. This results in a formal Fe-Fe bond order of 0.5, consistent with the contraction of the M-M bond from 2.429 Å in $[Ni_2Bi_{12}]^{4+}$ to 2.395 Å in $[Fe_2Sn_4Bi_8]^{3-}$. The PDOS and OPDOS plots in Figure 3.9 indicate that a substantial amount of Fe π^* character (green) is now found above the Fermi level, mixed with antibonding states on the cage in $5e_g$ (the negative peak in the Fe-Fe OPDOS at $\sim$+1.0 eV). The Fe-Fe π character remains largely below the Fermi level (in $5e_u$ at -1.8 eV), conferring a degree of Fe-Fe π character on the bond and indeed the calculated Fe-Fe Mayer bond order is 0.923, somewhat higher than the formal value. The π component to the Fe-Fe bond reflects that there is a higher tendency of back-bonding with the vacant levels of the E_{12} cage compared to the Ni_2 analogues. This change is captured in the difference density plots shown in Figure 3.10 (the difference between the self-consistent density and the sum of the pre-formed fragments).

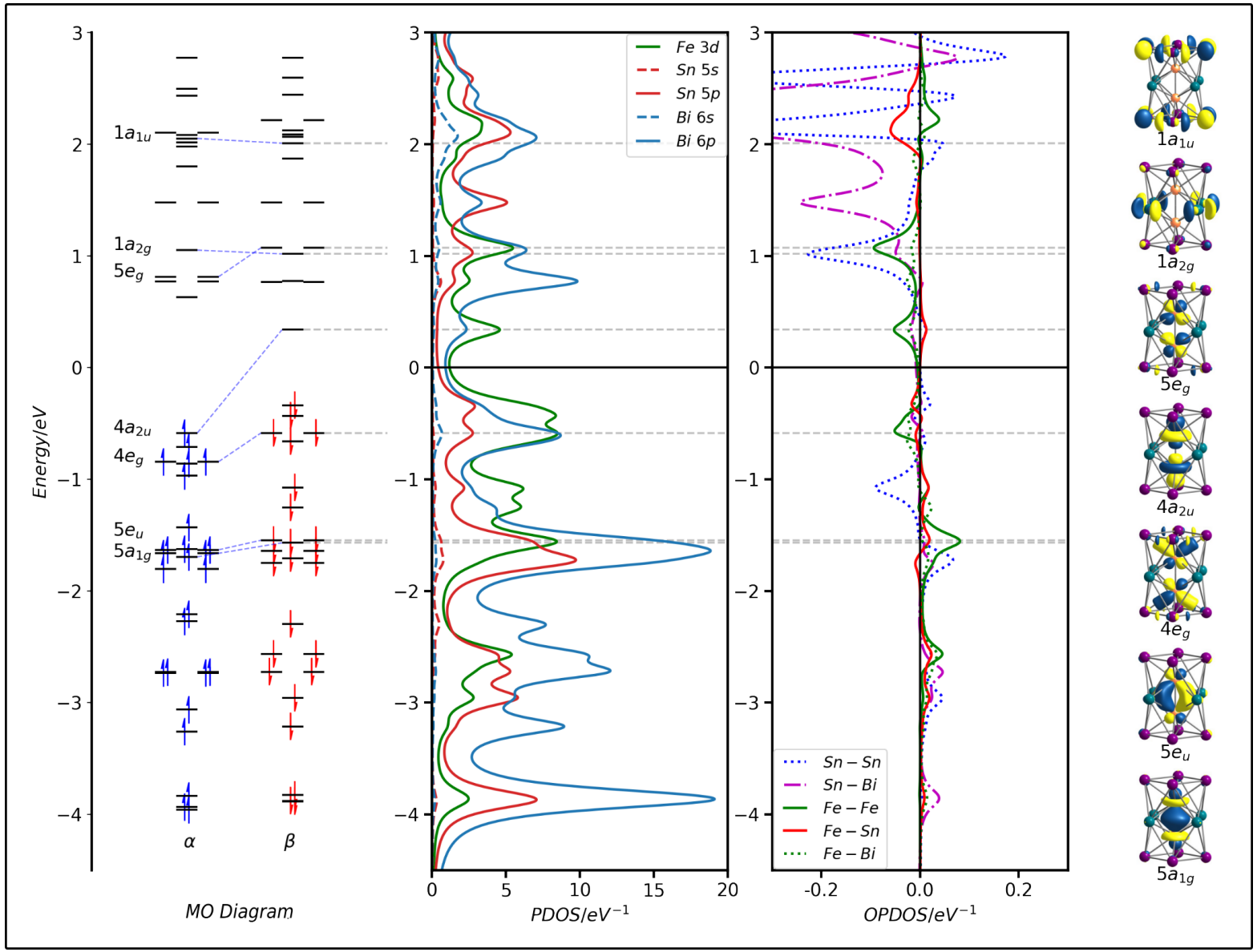

Figure 3.9: Kohn-Sham orbitals (α and β spins), Projected Density of States (PDOS) and Overlap-Projected Density of States (OPDOS) for the spin-β manifold of $[Fe_2Sn_4Bi_8]^{3-}$. The Fermi level, E_f, is defined as the mid-point between the HOMO and the LUMO of the spin-β set.

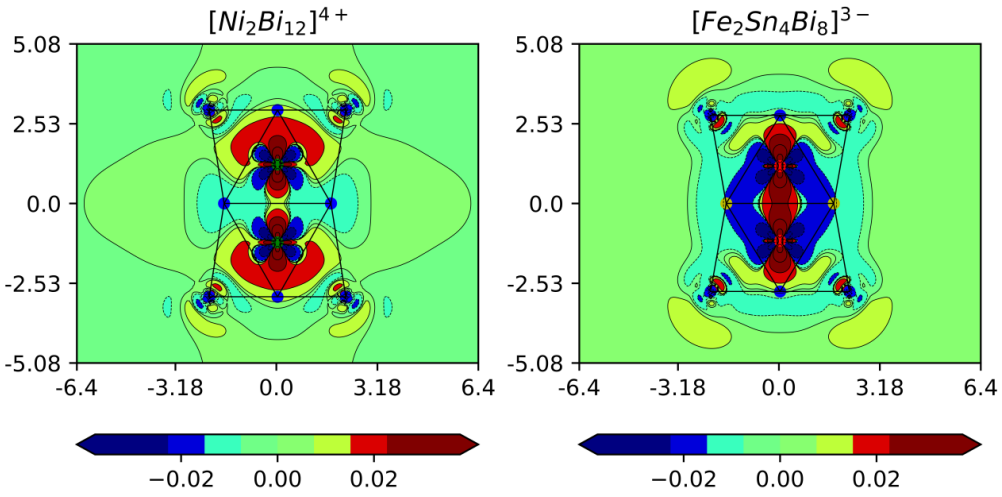

Figure 3.10: Difference density plots for $[Ni_2Bi_{12}]^{4+}$ and $[Fe_2Sn_4Bi_8]^{3-}$, showing the difference in electron density between the self-consistent solution and the sum of two separated fragments (Ni_2 + $Bi_{12}{}^{4+}$ or $Fe_2{}^{3-}$ + Sn_4Bi_8, respectively). Contours range from -3×10^{-3} to 3×10^{-3} e au^{-3}, and values on the x and y axes are in Å.

In both cases, a 56-electron configuration is imposed on the E_{12} cluster ($Bi_{12}{}^{4+}$ and $Sn_4Bi_8{}^0$, respectively), with 20 and 19-electron configurations on $Ni_2{}^0$ and $Fe_2{}^{3-}$, respectively. The plot on the left (Figure 3.10) shows that redistribution of electron density upon formation of $[Ni_2Bi_{12}]^{4+}$ from $Ni_2{}^0$ and $Bi_{12}{}^{4+}$ which is limited to a redistribution of electron density between the $3d_{z^2}$ and $4s$ orbitals on the $Ni_2{}^0$ core. In contrast, the charge transfer from the filled orbitals of the $Fe_2{}^{3-}$ fragment to the vacant levels of Sn_4Bi_8 is substantial, with charge accumulating at the poles of the cluster in $[Fe_2Sn_4Bi_8]^{3-}$ (red regions just inside the top and bottom Bi_4 rings) and a blue region of depletion around the Fe atoms, both of which carry the fingerprint of the Fe-Fe π^* orbital $5e_g$.

The experimentalists were unable to collect strong evidence to prove the paramagnetism of **1**, therefore it is plausible that the crystal may contain a mixture of $[Fe_2Sn_4Bi_8]^{2-}$ and $[Fe_2Sn_4Bi_8]^{4-}$ rather than $[Fe_2Sn_4Bi_8]^{3-}$, as proposed by Corbett and co-workers for the $Ge_9{}^{2-/4-}$ pair. To explore this use, we report the optimised structures of clusters **1** in their 2-, 3- and 4- states in Table 3.3. The most striking feature of the data in the table is the insensitivity of the geometry to charge. The 4- anion is diamagnetic, with the vacancy in the Fe-Fe σ^* orbital in Figure 3.9 filled, while the most stable state of the 2- analogue is a triplet with a second electron removed from the Fe-Fe δ^* orbital of b_{1u} symmetry. Despite the variations in formal Fe-Fe bond order from 1.0 (2-) to 0.0 (4-), the bond lengths vary by less than 0.08 Å,

reflecting the rigidity of the triple-decker E_{12} cage.

Table 3.3: Comparison of the optimised geometries of $[Fe_2Sn_4Bi_8]^{2-}$, $[Fe_2Sn_4Bi_8]^{3-}$ and $[Fe_2Sn_4Bi_8]^{4-}$ (all distances in Å).

		Fe-Fe	**Fe-Sn**	**Fe-Bi**	**Sn-Sn**	**Sn-Bi**	**Bi-Bi**
$[Fe_2Sn_4Bi_8]^{2-}$	$S = 1$	2.34	2.74	2.74	3.51	3.32	3.14
$[Fe_2Sn_4Bi_8]^{3-}$	$S = \frac{1}{2}$	2.37	2.68	2.71	3.40	3.30	3.10
$[Fe_2Sn_4Bi_8]^{4-}$	$S = 0$	2.42	2.67	2.75	3.37	3.35	3.11

3.2.3.5 75-electron $[Cr_2Sb_{12}]^{3-}$

The ground state of $[Cr_2Sb_{12}]^{3-}$ is also a spin doublet, with C_{4v} symmetry and an optimised Cr-Cr distance of 2.29 Å, shorter than the X-ray value (2.319 Å).

The symmetry of the ground state, $^2B_2$, is also different from the isoelectronic $[Fe_2Sn_4Bi_8]^{3-}$ cluster, with the unpaired electron now residing in the $5b_2$ orbital (Figure 3.11 left), a linear combination of Cr $d_{x^2-y^2}$ orbitals with local Cr-Cr δ^* symmetry. The Cr-Cr σ^* orbital, $10a_1$, is vacant in both α and β-spin components, indicating a formal σ bonding with bond order 1.0 compared to the $[Fe_2Sn_4Bi_8]^{3-}$ where bond order is 0.5. The corresponding Mayer Bond order is larger, 1.38, a direct measure of stronger Cr-Cr bonding.

To understand the relationship between $[Cr_2Sb_{12}]^{3-}$ and $[Fe_2Sn_4Bi_8]^{3-}$ in terms of different structures and electronic configurations, we need to establish the origins of the distortion from D_{4h} to C_{4v} symmetry in the former. To do so, we first constrain $[Cr_2Sb_{12}]^{3-}$ to the D_{4h}-symmetric potential energy surface, where we again find a doublet ground state, and the unpaired electron again resides in an orbital with Cr-Cr δ^* character ($2b_{2u}$) (Figure 3.12, left). The Cr-Cr separation is even shorter, at 2.161 Å, and the equatorial Sb_4 unit is very substantially expanded (Sb-Sb = 3.636 Å compared to Sn-Sn = 3.40 Å in $[Fe_2Sn_4Bi_8]^{3-}$). These structural differences can be reflected in changes in the electronic configuration. The $1a_{2g}$ orbital that was vacant in both $[Ni_2Bi_{12}]^{4+}$ and $[Fe_2Sn_4Bi_8]^{3-}$ is occupied in $[Cr_2Sb_{12}]^{3-}$, and the Sb-Sb antibonding character of the orbital drives the expansion of the equatorial plane. At the same time two metal-based spin orbitals, $4a_{2u}\alpha$ and $2b_{1u}\beta$ are depopulated and the M-M antibonding nature of the former leads to the large Mayer bond order (1.382) and the contraction of the Cr-Cr bond. The Cr_2 unit is oxidised to a much higher degree than the Fe_2 unit in $[Fe_2Sn_4Bi_8]^{3-}$. In short, the Cr_2 unit transfers two electrons from its uppermost, antibonding levels into an Sb-Sb antibonding level localised on the equatorial ring, simultaneously strengthening the Cr-Cr bond while

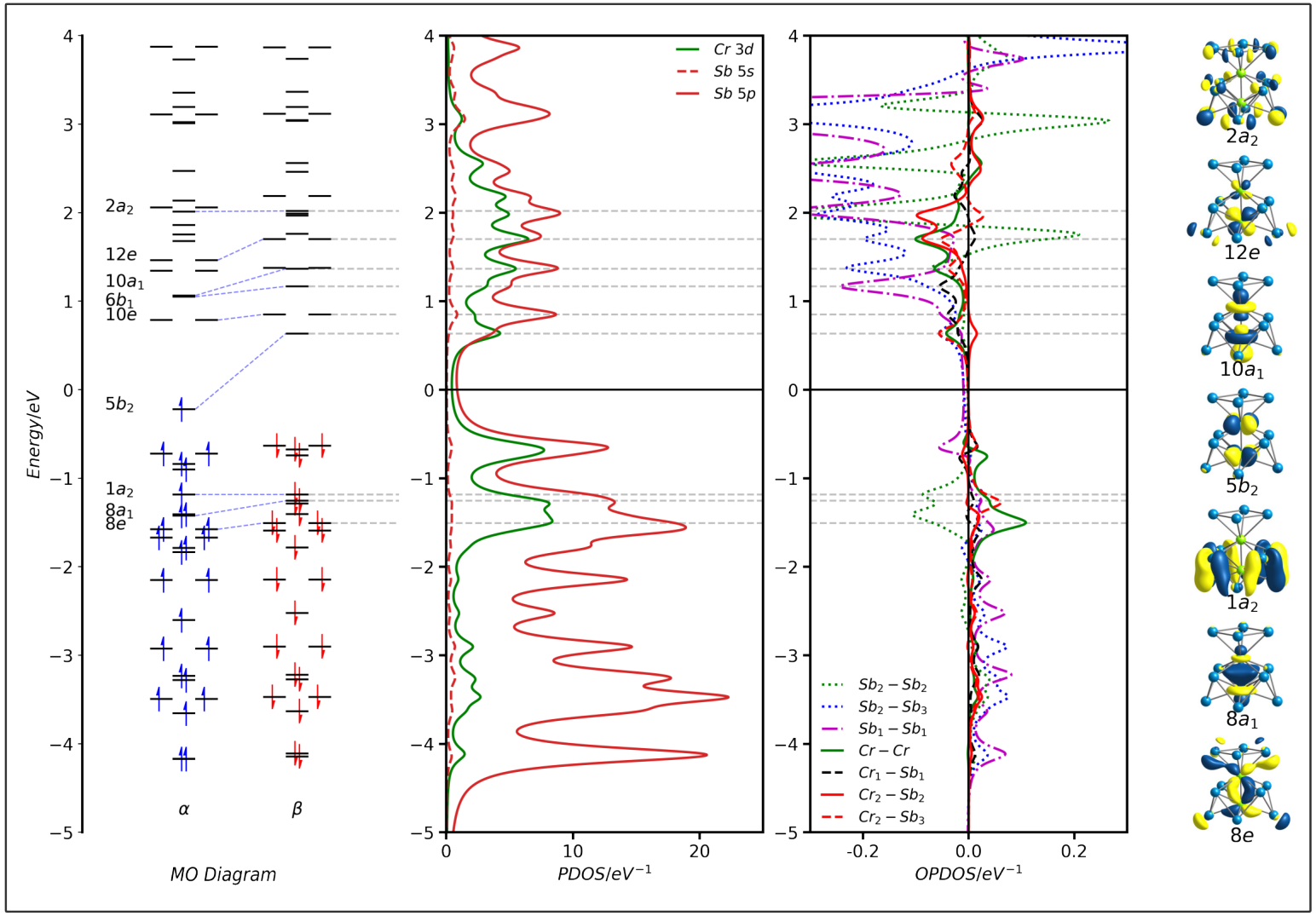

Figure 3.11: Kohn-Sham eigenvalue spectrum (α and β spins), Projected Density of States (PDOS) and Overlap-Projected Density of States (OPDOS) for the spin-β manifold of $[Cr_2Sb_{12}]^{3-}$.

weakening the Sb-Sb bonds. The D_{4h} symmetric structure is, however, 0.86 eV less stable than the C_{4v} global minimum. The driving force for the distortion comes from the energetic proximity of the now-occupied $1a_{2g}$ orbital and the vacant $1a_{1u}$ orbital, which is a similar linear combination of Sb $5p$ orbitals, but localised on the terminal Sb_4 units.

A distortion to C_{4v} point symmetry allows mixing between $1a_{2g}$ and $1a_{1u}$, both of which transform as a_2 in the lower symmetry - a second-order Jahn-Teller distortion. The evolution of the valence orbitals along a distortion coordinate linking the D_{4h} and C_{4v} structures is shown in the Walsh diagram in Figure 3.12 where the stabilisation of $1a_2$ and the destabilisation of $2a_2$ are shown in blue. The $1a_2$ orbital becomes bonding between the lower and middle Sb_4 planes (Sb_2 and Sb_3 in Figure 3.11) while $2a_2$ is Sb-Sb antibonding. Note that when both $1a_{2g}$ and $1a_{1u}$ are vacant, as they are in $[Fe_2Sn_4Bi_8]^{3-}$, there is no equivalent driving force and therefore no distortion. The differences between $[Fe_2Sn_4Bi_8]^{3-}$ and $[Cr_2Sb_{12}]^{3-}$ originate from a combination of two factors: (i) the higher energy of the $3d$ orbitals in Cr *vs* Fe and (ii) the lower energy of the $5p$ orbitals on Sb *vs* Sn, which controls the energy and hence the occupation of the $1a_{2g}$ orbital.

3.2.4 Conclusions

We have structurally characterised two new members of the M_2E_{12} family, $[Fe_2Sn_4Bi_8]^{3-}$ and $[Cr_2Sb_{12}]^{3-}$, both of which have 75 valence electrons. Despite having same electron count, the clusters have quite different structures, $[Fe_2Sn_4Bi_8]^{3-}$ is approximately D_{4h}-symmetric, very similar to the 76-electron analogues $[Ni_2Bi_{12}]^{4+}$, but $[Cr_2Sb_{12}]^{3-}$ has C_{4v} symmetry, with a $CrSb_8$ crown capped by a $CrSb_4$ fragment. The structural landscape can be understood in terms of a progressive upward shift in the energies of the metal d orbitals relative to those on the cage as we move from Ni to Fe and then to Cr (Figure 3.13). This leads to increased back-bonding in $[Fe_2Sn_4Bi_8]^{3-}$ and $[Cr_2Sb_{12}]^{3-}$, to an orbital crossing that shifts two electrons from Cr-Cr antibonding states into the Sb-Sb antibonding $1a_{2g}$ orbital. This then triggers a second-order Jahn-Teller distortion, leading to the observed C_{4v}-symmetric structure.

The trends in electronic structure and geometry for the M_2E_{12} family can be analogous to the chemistry of their counterparts ME_{12} and/or ME_{10} family. Like, $[Ni_2Bi_{12}]^{4+}$ is the direct analogue of $[NiPb_{12}]^{2-}$ and $[PtPb_{10}]^{2-}$, $[Fe_2Sn_4Bi_8]^{3-}$ is the analogue of $[MnPb_{12}]^{3-}$ and $[FeSn_{10}]^{3-}$ while $[Cr_2Sb_{12}]^{3-}$ is the analogue of $[RuGe_{12}]^{3-}$ and $[FeGe_{10}]^{3-}$. In the sense that the nd electrons shift from being structurally inert in the first group (Ni_2) to being a minor perturbation to the core deltahedral structure

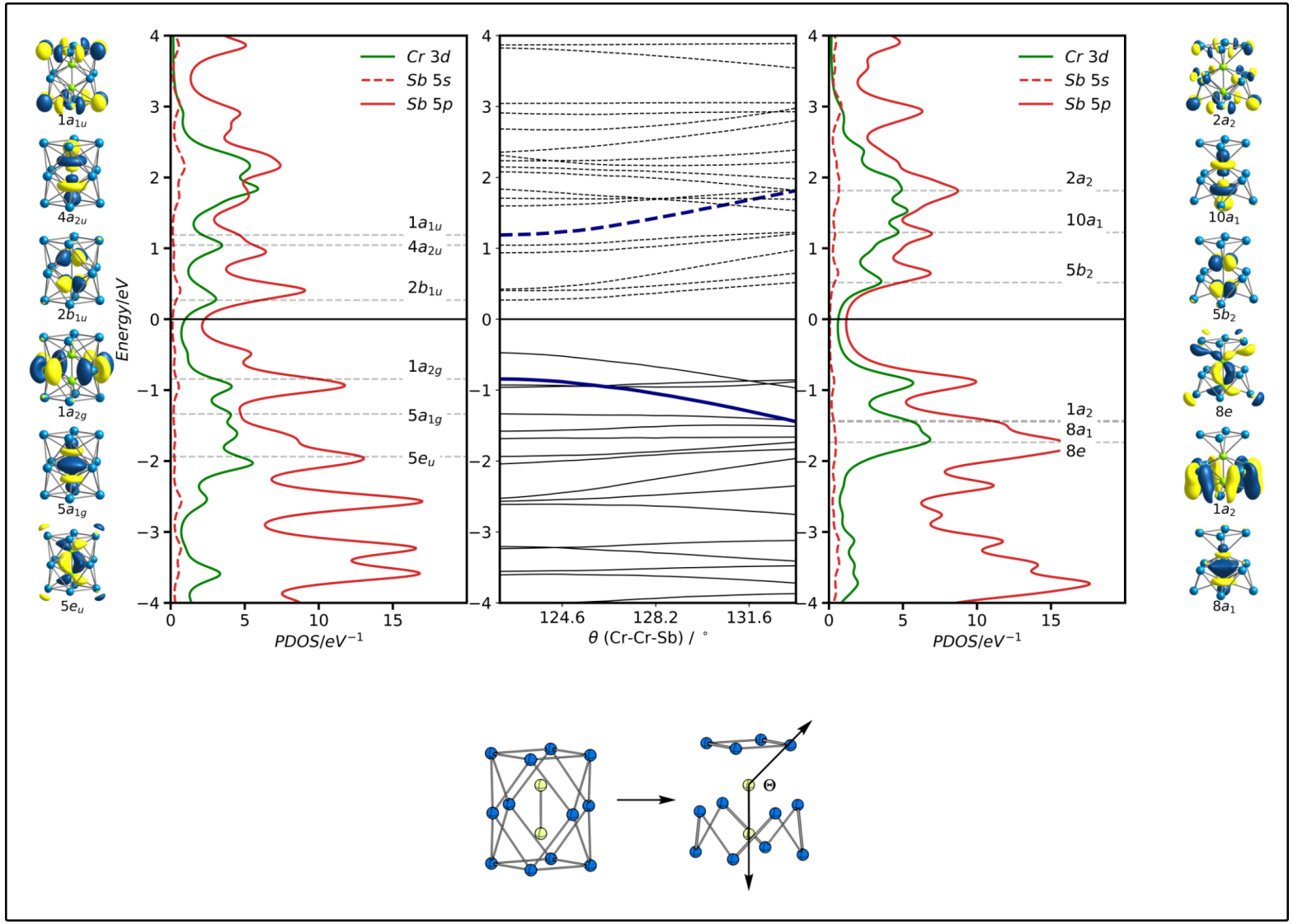

Figure 3.12: Walsh diagram connecting the D_{4h}- and C_{4v}-symmetric limits in $[Cr_2Sb_{12}]^{3-}$. 18 intermediate structures were generated by interpolating between the two optimised structures in Table 3.2. The orbitals and PDOS plots shown correspond to the spin-β set: occupied levels are shown as full lines, virtual levels as dashed lines and the $1a_2/2a_2$ pair is shown in blue.

and minor charge transfer in the second (Fe_2) and then to driving a switch to lower connectivity architectures with more M-cage interaction in the third (Cr_2). The Zintl cluster family offers a rich diversity with many different combinations of elements possible by identifying the underlying electronic factors which drive structural changes and systemic patterns within this remarkable family.

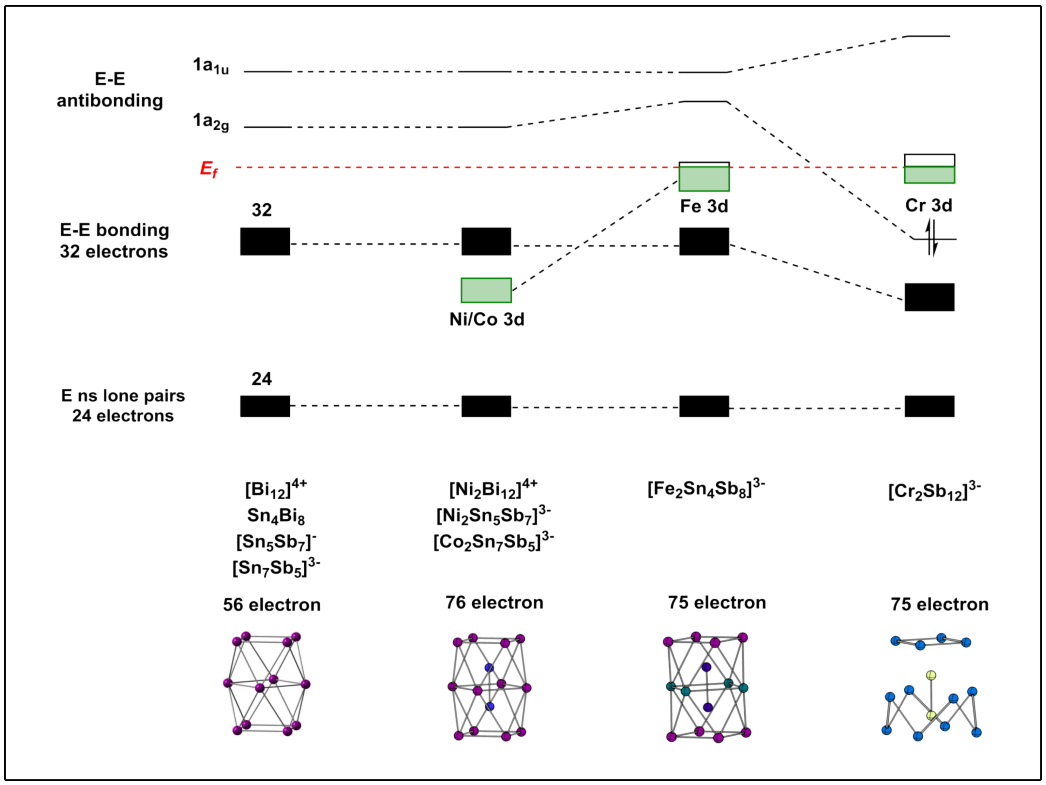

Figure 3.13: Overview of the trends in electronic structure across the 75- and 76-electron M_2E_{12} series.

3.3 Metal-Metal Bonding in Pentagonal Bipyramidal Cluster Compounds Containing a *cyclo*-Sn_5 Ring: $[(CO)_3MSn_5M(CO)_3]^{4-}$ (M = Cr, Mo)

3.3.1 Introduction

The chemistry of *cyclo*-Pn_5 rings of the pnictogens (Pn) is well established, and many compounds of P_5^- and its heavier congeners, As_5^- and Sb_5^-, have already been reported in the literature.[150–152] These compounds are not only interesting from a synthetic point of view but also as Pn is isolobal with a CH group,[153,154] allowing us to rationalise the similar structural chemistry of complexes of P_5 and C_5H_5.[155] Similar compounds with cyclo-Tt_5 rings containing the tetrel (Tt) elements Si, Ge, Sn and Pb are less explored. An isoelectronic relationship with Pn_5 would require a –6 formal charge on Tt. Tadorov and Sevov reported both Sn_5^{6-} and Pb_5^{6-} in a family of Zintl phases, Na_8BaPb_6, Na_8BaSn_6 and Na_8EuSn_6 where the charge was balanced by the presence of isolated Tt^{4-} and Tt_5^{6-} ions in the unit cell.[156] In late 1970s the lighter homologues of Tt_5^{6-}, such as Si_5^{6-} and Ge_5^{6-} were crystallised and characterised in the binary phases such as $Li_{12}Si_7$ and $Li_{11}Ge_6$.[157–159] The planar cyclo-Pn_5^- rings or Tt_5^{6-} rings can be stabilised by aromaticity (having 6π electrons) or by the number of valence/skeletal electrons. In terms of Wade's rule, the Tt_5^{6-} clusters have a $2n+6 = 16$ skeletal electrons count or, equivalently, $4n+6 = 26$ total valence electron counts, which leads to a 5-vertex *arachno* cluster based on a pentagonal bipyramid with two missing *trans* vertices. These two perspectives are equally valid and emphasise that the electronic structure of ring compounds and clusters of heavier main group elements is often quite complicated, with different interpretations possible.

After the report of Sn_5^{6-} and Pb_5^{6-} rings,[156] Fässler and co-workers synthesised a molecular analogue, $[(CO)_3MoPb_5Mo(CO)_3]^{4-}$, which they formulated as a Pb_5^{4-} ring bridging two neutral $Mo(CO)_3$ fragments.[160] The total electron count is now **4×5+4=24** which means the ring consists of 4π electrons with anti-aromatic character rather than aromatic. But the Pb-Pb bond lengths in this cluster (3.0138 - 3.0647 Å) are marginally shorter than those in the aromatic (6π) Pb_5^{6-} unit with a total electron count of 26 in Na_8BaPb_6 (3.047 - 3.117 Å). The electronic structure reveals a very substantial charge transfer from the Pb_5^{4-} ring to the $Mo(CO)_3$ fragments and back bonding from the metal (Mo) to the ligand (CO). Therefore, the C-O stretching frequencies are substantially reduced from the free CO value of 2143

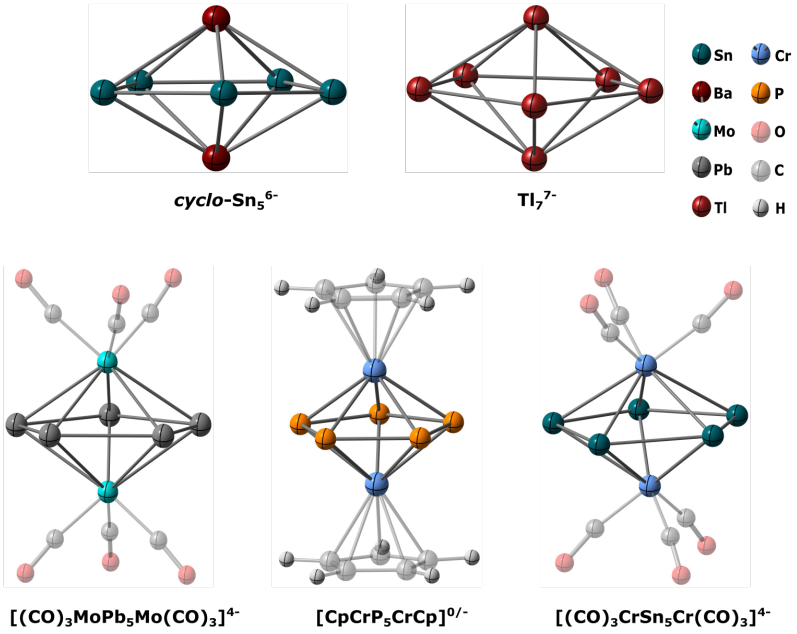

Figure 3.14: Examples of pentagonal bipyramidal cluster architectures from the transition metal series and main-group: *cyclo*-Sn_5^{6-}; Tl_7^{7-}; $[(CO)_3MoPb_5Mo(CO)_3]^{4-}$; $[CpCrP_5CrCp]^{0/-}$ and $[(CO)_3CrSn_5Cr(CO)_3]^{4-}$, this work .

cm^{-1} to 1889 cm^{-1}. This can confirm a simple correlation between bond lengths and formal charge on the five-membered ring. Gholiee et al. have recently published a detailed computational survey of the family of pentagonal bipyramidal clusters with general formula $[(CO)_3ME_5M(CO)_3]^{4-}$, M = Cr, Mo, W; E = Si, Ge, Sn and Pb.[161] Their analysis, using the M06-2X functional in combination with a def2-TZVPP basis, agrees with the conclusion from Fässler and Kaupp, that there is substantial charge transfer from the formally Tt_5^{4-} ring to the $M(CO)_3$ fragments and eventually carries a positive charge. Clearly, the formal charge is at best a first approximation, and the balance between M-M, M-Tt and Tt-Tt bonding is a delicate one.

In this section, we report the electronic structure analysis of two tin analogues of Fässler's lead cluster, $[(CO)_3MSn_5M(CO)_3]^{4-}$, M = Cr (**4**) and Mo (**5**). Both compounds are formed from the reaction of K_4Sn_9 with the organometallic precursors $M(MeCN)_3(CO)_3$ (M = Cr, Mo), and both feature a planar *cyclo*-Sn_5 motif capped by two $M(CO)_3$ fragments. This new structural data provides a platform to consider the general features of bonding in the family of pentagonal bipyramids. In the later part, we take the opportunity to compare these two new clusters to closely related species that share the pentagonal bipyramidal architecture and to compare the different electron-counting models that have been applied in this context.

3.3.2 Computational Details

All DFT calculations were performed using the ORCA 5.0.1 software.[162,163] A range of functionals were considered, including the generalised gradient approximation (GGA) functional proposed by Perdew, Burke, and Ernzerhof (PBE),[124] the hybrid B3LYP,[95] the meta-hybrid M06-2X[164] and the double-hybrid, B2PLYP.[165,166] Scalar relativistic effects were included using the zeroth-order relativistic approximation (ZORA).[167] A valence triple-zeta polarised relativistically re-contracted Karlsruhe basis set (ZORA-def2-TZVP)[168–170] was employed for H, C and O[171] and segmented all-electron relativistically contracted (SARC) basis sets were used for heavier elements. The RI-J approximation to the Coulomb integrals (J) was made using the (SARC/J)[169,170] auxiliary basis set appropriate for ZORA calculations. The conductor-like polarisable continuum model (CPCM) was implemented taking water as a solvent with a dielectric constant (ϵ) 80.4 to model the confining potential of the cation lattice.[172–175] The multiwfn package was used to analyse the topology of the electron density and to compute bond orders.[176] Similar methodologies, models and parameters were adopted in previous journals for DFT calculations and analysis.[177,178]

3.3.3 Results and Discussion

3.3.3.1 Structural Characterisation

The X-ray diffraction structures of the two anions $[(CO)_3CrSn_5M(CO)_3]^{4-}$ (**4**) and $[(CO)_3MoSn_5Mo(CO)_3]^{4-}$ (**5**) are shown in Figure 3.15. The X-ray analysis reveals that **4** crystallises in the triclinic space group $P\bar{1}$ and contains a $[(CO)_3CrSn_5Cr(CO)_3]^{4-}$ anion with a $[K_2(en)_3]^{2+}$ unit and two $[K([2.2.2]-crypt)]^+$ cations per cluster. **5** crystallises in the monoclinic space group $P2_1/c$ with one $[(CO)_3MoSn_5Mo(CO)_3]^{4-}$ anion, three $[K(18\text{-crown}-6)]^+$ cations and one further, isolated, K^+ in the unit cell. The structure of the $[(CO)_3MSn_5M(CO)_3]^{4-}$ anions (M = Cr, **4**; Mo, **5**) look like the Pb analogue,[160] pentagonal bipyramids with a Sn_5 ring capped by two $M(CO)_3$ fragments at the vertices. The M–M distances along the principal axis are 2.948(9) Å and 3.1393(5) Å in **4** and **5**, respectively. Fässler and co-workers showed that the Mo-Mo distance of 3.2156(8) Å in $[(CO)_3MPb_5M(CO)_3]^{4-}$ is longer than the Mo-Mo bond in $[Mo_2(CO)_{10}]^{2-}$ (Mo-Mo = 3.123 Å).[179]

The corresponding Mo-Mo distance of 3.1393(5) Å in the structure **5** is almost identical to that in $[Mo_2(CO)_{10}]^{2-}$, while the Cr-Cr distance of 2.948(9) Å in **4** is shorter than that in $[Cr_2(CO)_{10}]^{2-}$, 2.970 Å.[179] Therefore, the identification of metal-metal bonds in systems with bridging ligands is very difficult, as illustrated by the

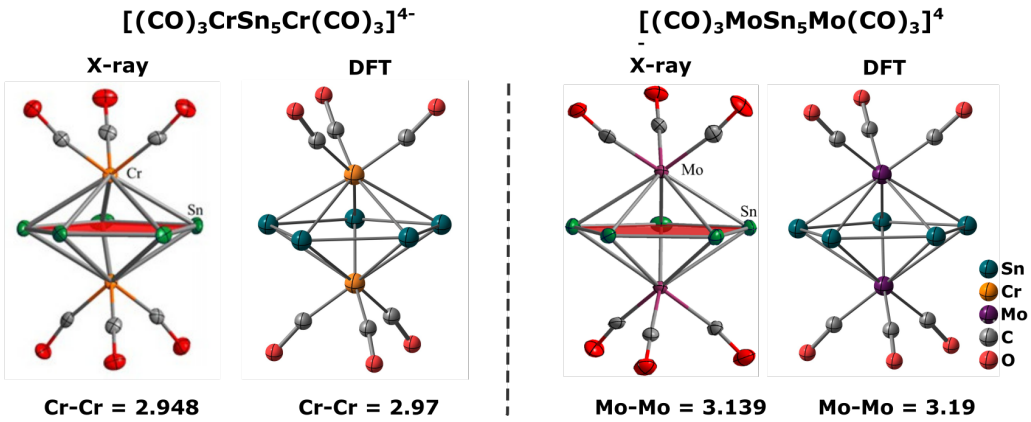

Figure 3.15: X-ray and DFT structure of anionic $[(CO)_3CrSn_5Cr(CO)_3]^{4-}$ and $[(CO)_3MoSn_5Mo(CO)_3]^{4-}$, respectively.

spirited debate over the existence or otherwise of a Fe-Fe bond in $Fe_2(CO)_9$.[180–182] But in this case, it seems clear that direct metal-metal bonding cannot be excluded just based on the structural data alone. The Sn_5 rings are almost perfectly planar, with the sums of the interior angles close to the ideal value of 540°(**4**: 539.850°; **5**: 539.928°). The Sn–Sn bond lengths in **4** (av. 2.878 Å) and **5** (av. 2.934 Å) similar to the values in the Sn_5^{6-} clusters: 2.883 Å in Na_8EuSn_6, 2.921 Å in Na_8BaSn_6, highlighting the absence of a simple relationship between bond length and formal charge.[156]

3.3.3.2 Electronic Structure

The DFT-based optimised structures of Sn_5 clusters $[(CO)_3MSn_5M(CO)_3]^{4-}$, (M = Cr, Mo) are shown in Figure 3.15 and the bond lengths are compared in the table 3.4, along with corresponding values for Fässler's Pb_5 cluster, using a range of exchange-correlation functionals.[160] The gradient corrected functionals (PBE) give somewhat shorter M-M bond lengths compared to their hybrid functional (B3LYP),[95] which is a relatively common observation in systems with weak metal-metal bonds.[183] But the double hybrid functional B2PLYP[165,166] predicts M-M bond lengths that are shorter than those of the other functionals and even shorter than the experimental values. Despite the functional dependence of the absolute bond lengths, the calculations replicate the important trends in the crystallographic data, irrespective of functional. Within the pair of Sn_5 clusters, the optimised Cr-Cr bond length is $\sim$ 0.2 Å shorter than the Mo-Mo bond and the Sn-Sn bonds in the Sn_5 ring are distinctly shorter in the Cr complex than its Mo counterpart. Likewise, the 0.07 Å elongation of the

Mo-Mo distance in $[M(CO)_3Pb_5M(CO)_3]^{4-}$ *vs* $[(CO)_3MSn_5M(CO)_3]^{4-}$ as seen in the X-ray data is reproduced across all functionals.

Table 3.4: Optimised bond lengths for $[(CO)_3MSn_5M(CO)_3]^{4-}$, M = Cr, Mo and $[(CO)_3MoPb_5Mo(CO)_3]^{4-}$ for PBE, B3LYP and B2PLYP functionals

		M-M	M-Tt	Tt-Tt
$[(CO)_3CrSn_5Cr(CO)_3]^{4-}$	X-ray	2.94	2.87	2.93
	PBE	2.97	2.88	2.91
	B3LYP	3.07	2.91	2.91
	M062X	2.97	2.86	2.88
	B2PLYP	2.85	2.87	2.93
$[(CO)_3MoSn_5Mo(CO)_3]^{4-}$	X-ray	3.14	2.93	2.94
	PBE	3.19	2.99	2.98
	B3LYP	3.27	3.02	2.98
	M062X	3.20	2.97	2.95
	B2PLYP	3.15	2.98	2.97
$[(CO)_3MoPb_5Mo(CO)_3]^{4-}$	X-ray	3.21	3.05	3.04
	PBE	3.22	3.08	3.09
	B3LYP	3.31	3.11	3.10
	B2PLYP	3.17	3.06	3.09

A schematic molecular orbital diagram showing the interaction between a Sn_5^{4-} fragment and a $(CO)_3M{-}M(CO)_3$ unit is summarised in Figure 3.16.

Note that the orbitals of the Sn_5^{4-} ring are labelled according to D_{5h} point symmetry while those of $M(CO)_3$ and $(CO)_3M{-}M(CO)_3$ are labelled according to C_{3v} and D_{3h}, respectively. The complete cluster has only C_s point symmetry (where the mirror plane passes through one of the CO ligands of the top Cr/Mo and one of the CO ligands of the bottom Cr/Mo, facing opposite and one of the Sn atoms in Figure 3.15) but is labelled according to D_{3h} to retain the parentage of the orbitals in which the ligand (CO) orientation is slightly nonsymmetric. The bonding interaction between the Sn_5^{4-} ring and the transition metal center is dominated by charge transfer from the highest occupied orbitals on Sn_5^{4-} with Sn-Sn σ (e_1') and Sn-Sn π (e_2'') character, which overlaps with in- and out-of-phase combinations of the degenerate LUMO of $M(CO)_3$ ($2e'$ and $2e''$, respectively) to generate near-degenerate pairs with a' and a'' symmetry (($5a'$,$3a''$), ($6a'$,$4a''$). The air- and moisture-sensitivity of both **4** and **5** has prevented the measurement of infra-red spectra for either, but our computed C=O stretching frequencies (1712 cm^{-1} and 1744 cm^{-1} for **4** and **5**, respectively) indicate a similar red-shift to that observed in the Pb_5 analogue (measured, 1737 cm^{-1},[160] calculated 1744 cm^{-1}). In addition, there is a further significant interaction between

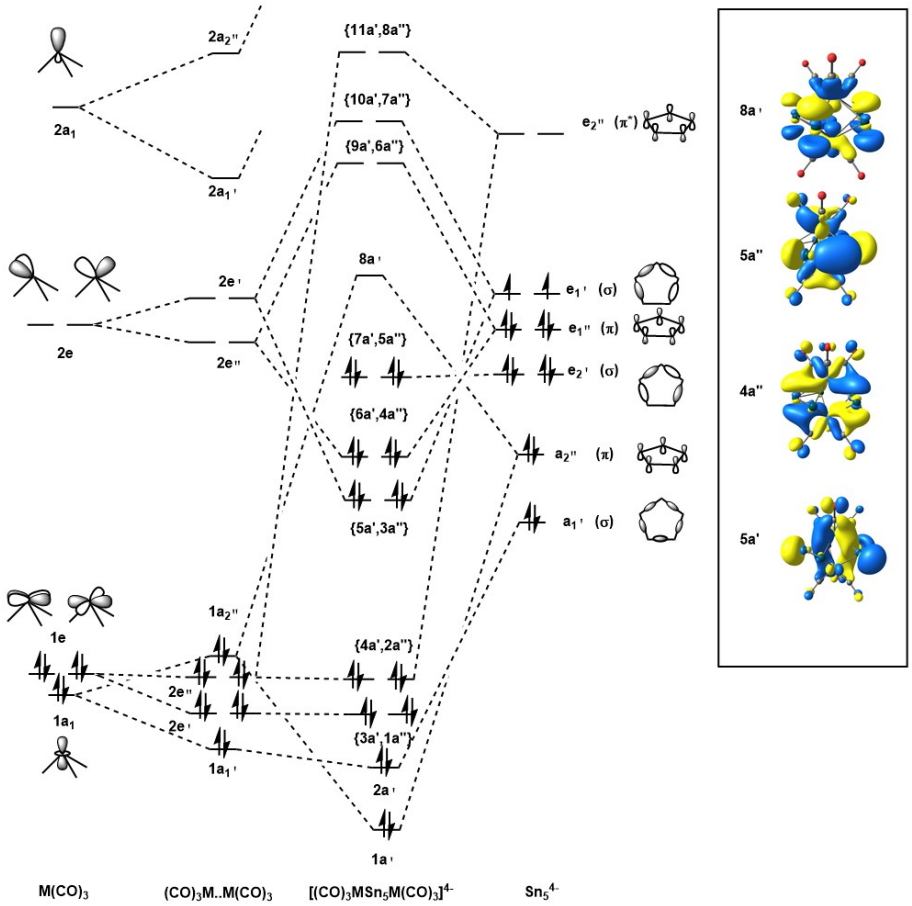

Figure 3.16: Schematic molecular orbital diagram for $[(CO)_3MSn_5M(CO)_3]^{4-}$. Note that the orbitals of the $M(CO)_3$, $M_2(CO)_6$ and Sn_5 fragments are labelled according to C_{3v}, D_{3h} and D_{5h} point symmetry, respectively. The cluster itself has only C_S point symmetry, but labels appropriate to D_{3h} are nevertheless used to emphasise the parentage of the orbitals.

the out-of-phase combination of d_{z^2} orbitals and the Sn_5 π a_2'' orbital, which destabilises the antibonding combination to the extent that it constitutes the LUMO of the complex ($8a'$). This LUMO, an iso-surface plot which is shown in Figure 3.16, is clearly localised primarily on the Sn_5 ring, with relatively minor contributions from the out-of-phase combination of Cr d_{z^2} orbitals.

3.3.3.3 Electron-counting and Metal-Metal Bonding in Pentagonal Bipyramidal Clusters

To place these new Sn_5 clusters into an appropriate context, it is useful to compare them with other 7-vertex cluster compounds (examples in Figure 3.14) with the same or similar formal electron counts. Perhaps the most obvious point of comparison is

with the 7-vertex main-group clusters $Tl_4Bi_3^{3-}$ and Tl_7^{7-}, the former was synthesised recently by Dehnen[184] and co-workers and the latter by Corbett and co-workers in 2000.[185] The $Tl_4Bi_3^{3-}$ cluster has a total valence-electron count of 4n+2 = 30, a skeletal-electron count of 2n+2 = 16, and is a classically *closo* cluster. It is worth emphasising that the additional 2n electrons included in the total count correspond to the radially directed lone pairs on the seven vertices, which have dominant 6*s* character in both clusters. Corbett's Tl_7^{7-} cluster has a total electron count of 28, two electrons fewer (4n = 28) and is compressed along the principal axis, generating a short *trans*-annular Tl-Tl bond. Its a_2''-symmetric LUMO (the HOMO of $Tl_4Bi_3^{3-}$), shown in Figure 3.17, has Tl-Tl π^* character around the equator, just like the LUMOs of $[(CO)_3MSn_5M(CO)_3]^{4-}$, but also substantial Tl 6*s* character on the apical Tl atoms, giving rise to the direct Tl-Tl bond.

We have analysed the electronic structure of $[(CO)_3MSn_5M(CO)_3]^{4-}$ in terms of the well-established electron-counting model. Fässler and Kaupp formulated the skeletal electron count as 2n = 14 skeletal electrons, treating the $Mo(CO)_3$ fragment as a zero-electron donor. The assumption here is that the occupied 3*d* orbitals, including the $3d_{z^2}$ orbitals aligned along the principal axis, are not involved in the cluster bonding. The linear combinations of $3d_{z^2}$ are the direct analogues of the 6*s* radial lone pairs in $Tl_4Bi_3^{3-}$, and if we include these we reach a total-electron count of 28 (= 4n), highlighting an isolobal analogy to Tl_7^{7-}. So why, then, do we consider a *trans*-annular Tl-Tl bond present in the main-group cluster, but not in $[(CO)_3MSn_5Cr(CO)_3]^{4-}$? The resolution to this is somewhat subjective: if the a_2'' LUMO is localised entirely on the apical atoms, a *trans*-annular bond is fully developed while the equatorial 5-membered ring retains the full complement of 6π electrons. At the opposite extreme, if the LUMO is localised entirely in the equatorial plane, the electron deficiency is accommodated in an anti-aromatic 4π ring while both in- and out-of-phase combinations of $3d_{z^2}$ are occupied, leaving no *trans*-annular bond. The LUMOs shown in Figure 3.18 suggest that the amplitude of the LUMO is indeed shifted towards the apical atoms in Tl_7^{7-} compared to $[(CO)_3CrSn_5Cr(CO)_3]^{4-}$, justifying the rather different descriptions of bonding.

A connection between these two limiting descriptions can be established through the P_5-bridged clusters, $CpCrP_5CrCp$ and $Cp^*CrP_5CrCp^*$ and their one-electron reduced analogues.[186,187] The neutral Cp cluster has a Cr-Cr separation is 2.69(1) Å, considerably shorter than that in **4**, and Hoffmann's analysis of the bonding concludes that there is indeed Cr-Cr bonding present.[188] The one-electron reduced analogue $[CpCrP_5CrCp]^-$ noted in Scherer's original report of the synthesis of the Cp^*

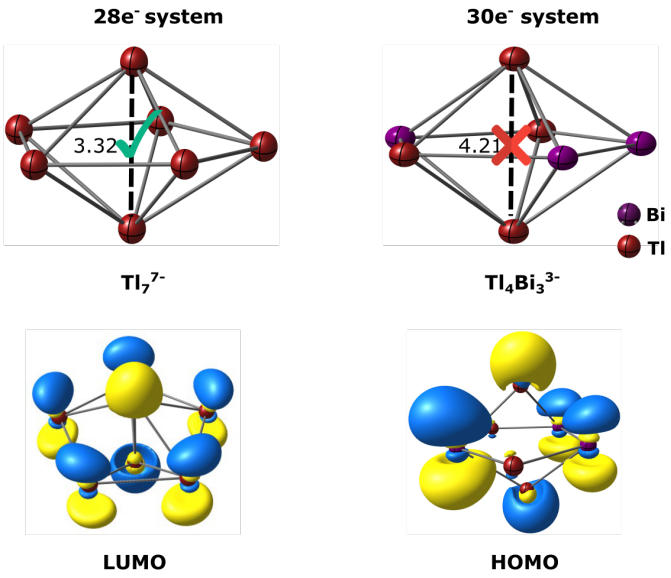

Figure 3.17: HOMO and LUMO isosurface plot of $Tl_4Bi_3^{3-}$ and Tl_7^{7-}, respectively.

compound is particularly interesting in the present context because its total valence electron count of 28 establishes a further isolobal relationship to both Tl_7^{7-} and $[(CO)_3CrSn_5Cr(CO)_3]^{4-}$.[187] The optimised structure of $[CpCrP_5CrCp]^-$ is summarised in Table 3.5, the Cr-Cr bond length of 2.61 Å is indicative of an even stronger Cr-Cr interaction than in the neutral species. The 28 available electrons in $[CpCrP_5CrCp]^-$ can either be partitioned to give a 6π-electron P_5^- ring and two d^5 CpCr fragments (and hence a Cr-Cr bond) or as a 4π-electron P_5^+ ring with two d^6 $CpCr^-$ fragments (and hence no Cr-Cr bond). The LUMO shown in Figure 3.18 is clearly strongly localised on the apical Cr atoms with relatively minor contributions on the equatorial P_5 ring, confirming that the electron deficiency is accommodated on the apical atoms.

An important point to take from this analysis is that there is no black-and-white distinction between the electronic structure models for $[(CO)_3CrSn_5Cr(CO)_3]^{4-}$ (M = Cr, Mo), $[CpCrP_5CrCp]^-$ and Tl_7^{7-}. All three share a common skeletal-electron count of 28, 2 fewer than the *closo* count of 30 and they constitute a continuum of situations defined by the shape of the LUMO, and hence the electron deficiency (relative to the *closo* form) is accommodated. In terms of the molecular orbital diagram shown in Figure 3.16, the limiting cases defined by $[(CO)_3CrSn_5Cr(CO)_3]^{4-}$ and $[CpCrP_5CrCp]^-$ are connected by a shift in the relative energies of the metal- and E_5-based fragments. A downward shift of the orbitals on the E_5 ring will increase the metal d_{z^2} character in the LUMO, increasing the importance of the *trans*-annular

bonded resonance form.

3.3.3.4 QTAIM Analysis

The Quantum Theory of Atoms in Molecules (QTAIM) offers an alternative perspective on the nature of the bonding in these systems. However, we note that the separation of metal-metal and metal-ligand bonding remains far from simple.[189]

Table 3.5: Comparison of Mayer bond orders (BO) and QTAIM parameters for the *trans*-Annular M-M Bond Critical Points (BCPs) for 28-electron M_2E_5 clusters, $[(CO)_3CrSn_5Cr(CO)_3]^{4-}$, $[CpCrP_5CrCp]^-$, and $Tl_7{}^{7-}$

	$[Cr_2Sn_5(CO)_6]^{4-}$	$[Mo_2Sn_5(CO)_6]^{4-}$	$[CpCrP_5CrCp]^-$	$Tl_7{}^{7-}$
r_{M-M}/Å	2.97	3.19	2.62	3.32
BO_{M-M}	0.39	0.28	0.72	0.31
δ_{M-M}	0.40	0.44	0.93	0.52
ρ_{BCP}/ au	0.028	0.029	0.055	0.020
G_b / au	0.010	0.011	0.026	0.009
V_b / au	-0.015	-0.017	-0.045	-0.010

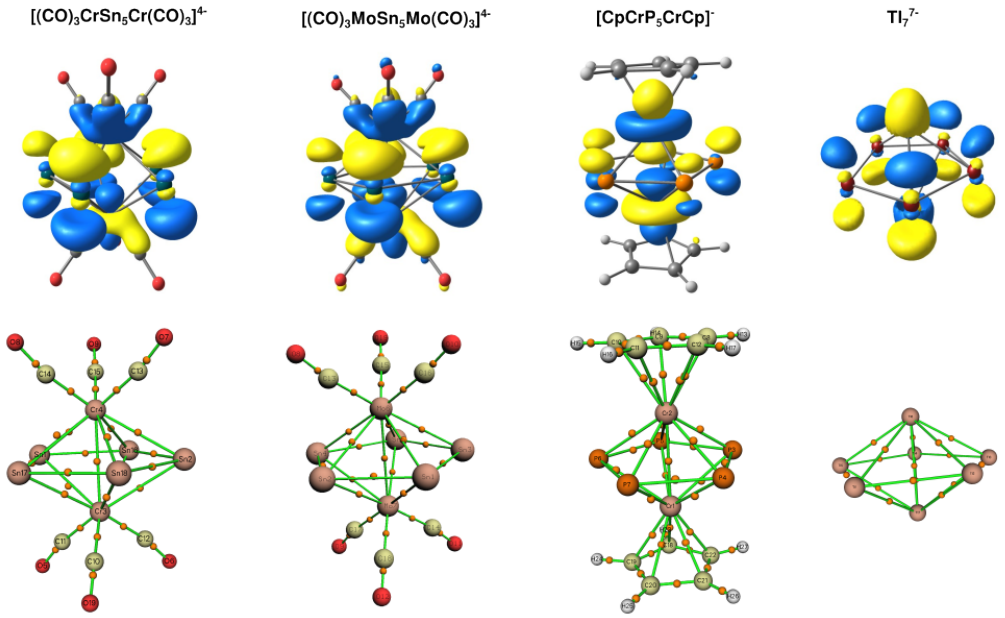

Figure 3.18: Molecular graphs and contour plots of the LUMOS of $[(CO)MSn_5M(CO)_3]^{4-}$ (M = Cr, MO), $[CpCrP_5CrCp]^-$ and $Tl_7{}^{7-}$. Bond Critical Points (BCPs) are shown in the molecular graphs as red dots.

The delocalisation index, δ, offers a direct measure of Cr-Cr bond strength and the values of 0.26 and 0.59 for $[(CO)_3CrSn_5Cr(CO)_3]^{4-}$ and $[CpCrP_5CrCp]^-$, respec-

tively. This correlates directly with the computed values for the Mayer bond order (0.39 and 0.72) extracted from the wavefunction itself (Table 3.5). The topology of the electron density reveals bond critical points (BCPs) midway between the Cr centres for both $[(CO)_3CrSn_5Cr(CO)_3]^{4-}$ and $[CpCrP_5CrCp]^-$ (see molecular graphs in Figure 3.18), but the electron density at the BCP (ρ_{BCP}) is considerably larger for the latter (0.055) than the former (0.028). Following Macchi's classification of the local indicators of bond type, the balance between kinetic (G_b) and potential (V_b) energies is consistent with an open-shell-type interaction in both, although the local dominance of V_b over G_b in $[CpCrP_5CrCp]^-$ is indicative of enhanced covalent Cr-Cr character.[190] All of the indicators, structural and electronic, are therefore consistent with the conclusion that Cr-Cr bonding is considerably stronger in $[CpCrP_5CrCp]^-$ than it is in $[(CO)_3CrSn_5Cr(CO)_3]^{4-}$. The Mayer bond order, delocalisation index and properties of the *trans*-annular BCP for the Tl_7^{7-} cluster suggest that it sits closer to $[(CO)_3CrSn_5Cr(CO)_3]^{4-}$ than to $[CpCrP_5CrCp]^-$ on this spectrum of bond types.

3.3.4 Conclusions

The two new cluster compounds, $[(CO)_3MSn_5M(CO)_3]^{4-}$, M = Cr, Mo, feature a pair of zero-valent $M(CO)_3$ fragments bridged by a *cyclo*-Sn_5 unit. The Sn clusters are isostructural with the Pb analogue, $[(CO)_3MoPb_5Mo(CO)_3]^{4-}$, reported previously by Fässler and co-workers. The LUMO of both clusters has a dominant Sn-Sn π character, consistent with their formulation as Sn_5^{4-} rings coordinated to two zero-valent $Cr(CO)_3$ fragments. The electronic structure makes a striking contrast with the isoelectronic $[CpCrP_5CrCp]^-$ anion, where the relative energies of the orbitals on the E_5 and M_2 fragments are reversed, causing the LUMO to have dominant Cr-Cr σ^* rather than Sn-Sn π character. The Tl_7^{7-} cluster is isolobal with both clusters and the axial compression in this *hypo*-electronic cluster is strikingly reminiscent of the short Cr-Cr bond in $[CpCrP_5CrCp]^-$. This triad of 28-electron clusters therefore maps out a continuum of situations between two limits where (i) The LUMO is localised in the equatorial E_5 ring ($[(CO)_3Cr/MoSn_5Cr/Mo(CO)_3]^{4-}$), and (ii) the LUMO is localised on the M_2 caps ($[CpCrP_5CrCp]^-$), forming a *trans*-annular bond. This continuum perspective establishes a link between apparently quite different electron-counting perspectives.

3.4 Summary and Conclusions

In this Chapter, I have discussed the electronic structure of a number of new clusters that contain Sn in combination with a range of different transition metals. The $[Ru@Sn_{12}]^{4-}$ cluster serves as a benchmark, where back-bonding from a single metal to Sn does not drive structural change, but softens the Sn-Sn vibrations. In the latter sections, I turn to bimetallic clusters (two transition metals) and show how the subtle interplay of metal-metal and metal-Sn bonds determines the structure. The majority of known transition metal encapsulated Zintl clusters are well described as 'closed-shell' clusters where the TM has a d^{10} electronic configuration and there is little or no direct interaction with the cage, preserving its original structure and symmetry. On the other hand, in cases where the d-orbitals on the metal are not core-like, interactions with the orbitals of the cage, increase the total electron count of the cluster. Therefore, a careful consideration of the role of the metal d electrons is essential to understanding the structural diversity within this family of clusters.

In the first compound, $[Ru@Sn_{12}]^{4-}$ we have found that in X-ray structure the cluster is slightly distorted from an ideal icosahedral geometry, but the DFT analysis indicates that, at least in the gas phase, the equilibrium structure has perfect I_h symmetry. However, back-bonding is reflected in a very soft h_g-symmetric vibrational mode, and also the energetic proximity of the 3-connected (fullerene-like) architecture adopted by endohedral $[Ru@Ge_{12}]^{3-}$ and $[Ta@Ge_8As_4]^{3-}$. It seems likely, therefore, that the distortions observed in the solid state are a consequence of the presence of K^+ cations in the lattice, which are not included in the model. Theoretically, we have shown that if we go beyond Ru, $[Tc@Sn_{12}]^{5-}$ would be very close to the cross-over point to the 3-connected D_{2d} structure cluster, reflecting the further destabilisation of the d-orbitals and enhanced back-bonding to the g_g-symmetric LUMO of the icosahedral cage. Backbonding becomes more prominent in the case of our next study, comparing the structural chemistry of the isoelectronic pair $[Fe_2Sn_4Bi_8]^{3-}$ and $[Cr_2Sb_{12}]^{3-}$. The former has an ideal triple-decker architecture with D_{4h} symmetry, very common for the M_2E_{12} family cluster, where the metal d-electrons are core-like. $[Cr_2Sb_{12}]^{3-}$, in contrast, is significantly distorted from D_{4h} to C_{4v} symmetry and can be viewed, to a first approximation, as a $CrSb_8$ crown with a separate Sb_4 ligand. The upward shift of d-orbital energy from Ni to Fe to Cr leads to increased back-bonding in both systems. In $[Cr_2Sb_{12}]^{3-}$, orbital crossing occurs, transferring electrons from a Cr-Cr antibonding orbital to a Sb-Sb antibonding orbital, breaking the Sb_{12} unit into two fragments. The metal-metal bonding is significant for both

of the systems and post-optimisation analysis suggests the M-M formal bond order is 0.5 and 1 for Fe_2 and Cr_2 clusters, respectively. The interplay of M-M and M-Sn bonding is less straightforward in the final pair of structures $[(CO)_3MSn_5M(CO)_3]^{4-}$, M = Cr, Mo, because a single orbital is both M-M and Sn-Sn bonding. The LUMO in $[(CO)_3CrSn_5Cr(CO)_3]^{4-}$ has dominant Sn-Sn π rather than metal d character for , leading us to propose a formulation as $Sn_5{}^{4-}$, with neutral $M(CO)_3$ fragments. The multiple bond character leads to Sn-Sn bond distances of 2.91 Å, shorter than single Sn-Sn bond distances of 3.067(2)-3.167(3) Å in $Ca_{31}Sn_{20}$.[191]

Chapter 4

Catalysis of the Water-Gas Shift Reaction by $Ru@Sn_9$

4.1 Introduction

The use of Zintl clusters or metalloids rather than isolated noble metal atoms as the catalytic centre offers the potential to exploit the interactions between transition and main-group metal to achieve low-barrier reactions, and recent work from our collaborators in Tianjin suggests that Zintl clusters are effective catalysts for the reverse water gas shift (rWGS) and CO_2 methanation reaction. Common active catalysts for WGS (or r-WGS) reactions are highly dispersed or isolated transition metals such as Ru, Ni, Rh, Ir and Pd on oxide surfaces.[192] Recently, Sun et al. have reported the selective reduction of CO_2 on highly dispersed $RuSnO_x$ sites, derived from a $[Ru@Sn_9]^{6-}$ Zintl cluster.[3] Different reaction media, pressures and temperatures were used to explore the selectivity of the catalyst, but an atomic-level understanding of the mechanism, and how it relates to the electronic properties of the cluster remain unclear.

Metal oxide surfaces are often used as excellent support for noble metals because of their flexible oxidation states and high activity in redox reactions, which is often due to oxygen defects in CeO_2, Al_3O_4, TiO_2 etc. Cerium oxide is one of the most efficient compounds, in part because of facile changes in oxidation state between Ce^{4+} to Ce^{3+}, and is widely used in high-performance oxygen storage applications and catalytic redox reactions, solid oxide fuel cells, water-gas shift reactions, etc. Ceria (CeO_2) itself is not highly efficient for catalytic reactions but, over the past two decades, numerous studies have been conducted on depositing different transition metals on the oxide surface, with remarkable success.[193] These supported oxides maintain high catalytic efficiency while reducing the huge cost of using bulk noble metal catalysts or

larger (nano)particles of Au, Pt, and Pd in industrial processes. Here, we will briefly discuss about the water-gas-shift (WGS) reaction and the development of ceria-based noble metal catalysts for the WGS reaction.

4.1.1 The Water Gas Shift (WGS) Reaction

The Water Gas Shift Reaction (WGSR) is an important reaction in many industrial processes like hydrogen production, manufacturing ammonia, steam-methane reforming, hydrocarbon production etc. It is the conversion of carbon monoxide in the presence of water vapour to carbon dioxide and hydrogen. A schematic model of how the WGS process is utilised in industries is shown in Figure 4.1. This reaction is thermodynamically exothermic.

$$CO + H_2O \rightleftharpoons CO_2 + H_2 \qquad \Delta H = -41\ kJ/mol \tag{4.1.1}$$

Even though the WGSR was discovered in 1780 by an Italian physicist Felice Fontana, this method started to be implemented extensively in industries long after, in the early 20th century for mass production of hydrogen at a lower cost. Because of the huge demand for hydrogen, there is always a need for large-scale hydrogen production in industries. A cheap and efficient catalyst can facilitate the demand. Therefore it's always a motivating topic for researchers to discover a better catalyst. The conventional way of hydrogen production in ammonia synthesis plants has been using iron oxide-chromium oxide catalyst at higher temperatures 310-450°C since the early 20th century. But over the years a lot of developments have been done to tune the catalyst properties like efficiency, reducing sulfur poisoning, thermal stability etc. Noble metals on a support offer a great potential to be excellent catalysts. Based on these developments and our interest we have discussed briefly mainly three types of catalysts in this section : (i) High-Temperature Shift Catalysts, (ii) Low-Temperature Shift Catalysts, and (iii) Ceria and Noble Metal-based Catalysts.

4.1.1.1 High-Temperature Shift Catalysts

As the name suggests High-Temperature Shift (HTS) catalysts work well at relatively high temperatures in a range of 310-450°C, whereas they fail badly at lower temperatures.[194] The HTS catalyst iron oxide-chromium oxide started being used commercially in 1914, with the composition of 74.2% Fe_2O_3, 10% Cr_2O_3, 0.2% MgO and remaining percentage attributed to volatile components. Fe-based HTS catalysts

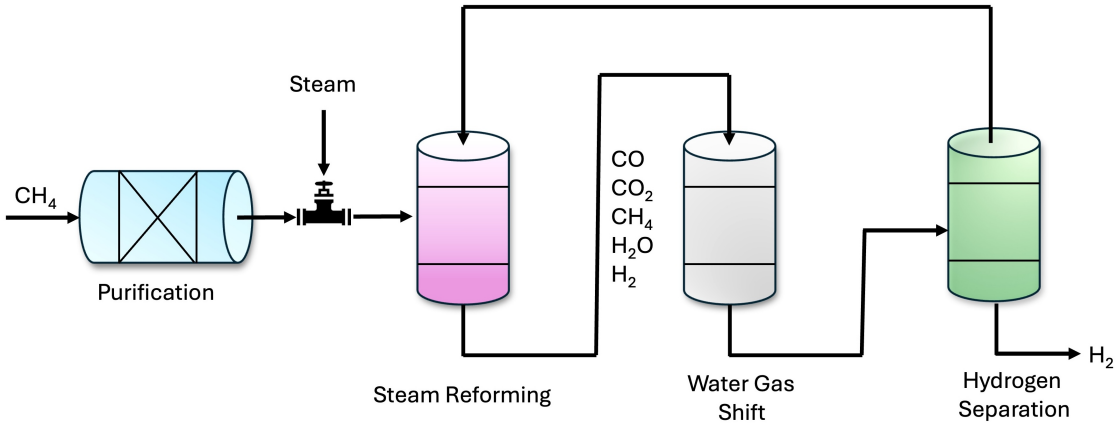

Figure 4.1: Scheme of methane-steam reforming and ware-gas-shift process for H_2 production.

are synthesised by the co-precipitation method as hematite (Fe_2O_3) and then reduced to magnetite (Fe_3O_4) during the process.[195]

$$3\,Fe_2O_3 + CO \rightleftharpoons 2\,Fe_3O_4 + CO_2 \qquad \Delta H = +24.8\ kJ/mol \tag{4.1.2}$$

$$2\,Fe_3O_4 + H_2O \rightleftharpoons 3\,Fe_2O_3 + H_2 \qquad \Delta H = +16.3\ kJ/mol \tag{4.1.3}$$

A careful reduction process is required to avoid the formation of metallic iron which could lead to the Fischer-Tropsch process and produce hydrocarbons. Once Fe_2O_3 is reduced to Fe_3O_4, still, chromium remains as Cr^{3+} in Cr_2O_3 and inhibits the re-crystallisation of magnetite, acting as a stabiliser. The Fe-Cr catalysts can only be used for 3-5 years because of the sintering and need to be replaced.[192,196] Several studies show that the catalytic activity of Fe-Cr catalyst depends on the Fe^{2+}/Fe^{3+} electronic nature of the system and adding some cations which have similar charge, size and ionisation potential as Fe^{2+} in the lattice can influence the stabilisation and reactivity of the catalysts, for example, Mn^{2+}, Ni^{2+}, Zn^{2+}, Co^{2+} transition metal promoters and other metal cations, Ba^{2+}, Pb^{2+}, Hg^{2+} etc.[197–199] Among all transition metal promoters, rhodium has been proven to be one of the most effective HTS-WGS catalysts for hydrogen release.[200] Even though various promoters have been reported for catalytic advancement, the number of promoters has been narrowed down considering the toxicity and environmental impact. The Fe-Cr-based catalysts exhibit outstanding catalytic activity but several attempts have been made to find a suitable substitute which is chromium-free. A good replacement could be Al, Al-Cu or Ni.[201] Recently, Alumina has been believed to be a good HT-WGS catalyst because of its higher surface area and thermal stability.[202]

4.1.1.2 Low-Temperature Shift Catalysts

This reaction occurs at slightly low temperatures in the range of 200-250°C or below. The Low-Temperature Shift (LTS) catalyst is a mixture of ZnO, CuO and Al_2O_3/Cr_2O_3. The typical composition, reported by Newsome et al. is 68-73% ZnO, 15-20% CuO, 9-14% Cr_2O_3, 2-5% Mn, Al and MgO, whereas 32–33% CuO, 34–53% ZnO, 15–33% Al_2O_3 composition was mentioned by C. Rhodes et al.[194,203,204] ZnO and Cr_2O_3 helps on the crystallisation of the catalyst and Al_2O_3, mainly inactive, in some cases helps in the dispersion and minimises pellet shrinkage. These Cu/Zn catalysts are air sensitive, sulfur, halogen and unsaturated hydrocarbon intolerant, so these need to be protected. ZnO is a good protector from sulfur poisoning.

$$CuO + H_2 \rightleftharpoons Cu + H_2O \qquad \Delta H = -80.8\ kJ/mol \tag{4.1.4}$$

As LTS catalysts are very sensitive and selective, the conversion ratio is quite high even at low intake. Like HTS catalysts, some TM promoters like Mn can promote Cu/Al_2O_3 efficiency for CO conversion of about 90% in WGSR.[205] The Cu-based LTS catalyst is not only restricted to the mixture of Cu-Zn, a variety of different structural modifications, and incorporation of noble metals and oxide supporting system have been developed by the researchers over the years to minimise the poisoning, sintering effect and maximise the stability, efficiency and sustainability of the catalysts. For instance, Cu-based perovskites are stable and efficient (for example $La_{1.85}Ca_{0.15}CuO_4$), also Cu nanoparticle or CuO supported on CeO_2, ZrO_2 has a high stability and conversion rate.[206]

4.1.2 Ceria and Ceria-supported Catalysts

4.1.2.1 Ceria (CeO_2)

Cerium dioxide (CeO_2 or ceria) was first used by Ford Motor Company as an oxygen storage component in car converters around 50 years back. Since then there has been a massive spike in implementing ceria not only in the car industries but also in petrochemical industries, fertiliser factories, fuel cells etc.[193] Ceria is directly involved with some important catalytic reactions such as water gas shift reaction, photocatalysis, reforming process, thermochemical water splitting, and hydrocarbon reaction, thus representing a big market.

Cerium (Ce) is one of the most abundant rare earth elements on earth and affordable to use. It does not fall in the 'critical rare earth' category, which means the risk of use is comparatively low. That allows researchers to exploit the element for

different uses. Therefore, the number of research articles on ceria and ceria-based catalysts has increased exponentially over two decades. Different phases of cerium oxides can be formed after the oxidation of metallic Ce, mainly Ce(III) and Ce(IV) ionic states in Ce_2O_3 and CeO_2 respectively, depending on the reaction temperature and oxygen pressure. Non-stoichiometric CeO_{2-y} can be found after releasing oxygen from the crystal and the oxygen vacancies are very common in ceria, which leads to a mixture of oxidation states in ceria.

$$CeO_2 - yO \rightarrow CeO_{2-y} + \frac{y}{2}O_2 \tag{4.1.5}$$

This excellent ability to shift between Ce(III) and Ce(IV) states by buffering oxygen in the crystal makes ceria and ceria-based mixed oxides unique. This property is called oxygen storage capacity (OSC), introduced to evaluate and compare redox properties, especially in automotive converters. Several experimental techniques can be used to study the oxygen storage kinetics such as oxygen buffering capacity (OBC).[207]

Many theoretical studies have been performed to provide a fundamental understanding of the electronic structure and properties of CeO_2 (ceria) and ceria-based catalysts.[208] One of the most common investigations is to find the position of extra electrons when the system is reduced. Reduction can happen either by oxygen vacancies and/or by the supported materials. In some studies, it has been revealed that for an oxygen-defected CeO_2 surface, the Ce ion close to the oxygen vacancy (nearest neighbour, NN) does not reduce to Ce^{3+} from the initial Ce^{4+}, but the reduction would be a bit far away from the vacant site which is called 'next nearest neighbour' (NNN).[209,210] DFT with the HSE06 (hybrid functional) and DFT+U (Hubbard correction) was used for this analysis. However, the LDA+U method suggested the NN Ce ion reduction. Therefore, the localisation of the electrons depends on the methods adopted in the study to some extent but mainly depends on the supported system.

Applications of Ceria

The applications of ceria and ceria-based catalysts are quite diverse (Figure 4.2) and crucial for modern chemical technologies.

A. Three-Way Catalysts (TWC) :

As the name suggests, three major reactions are catalysed by TWCs, oxidation of CO and hydrocarbons (CH) and the reduction of nitrogen oxides (NO_x). These are the major pollutants produced in the automobile engine by combustion of gasoline and the automotive TWCs are used to remove those pollutants. Al_2O_3 doped ceria, some CeO_2 based promoters $Ce_xZr_{1-x}O_2$, noble metal supports Pt/Pd on CeO_2 and mixed oxides CeO_2-ZrO_2 are commonly used as TWCs.[211] The principal role of the CeO_2 is

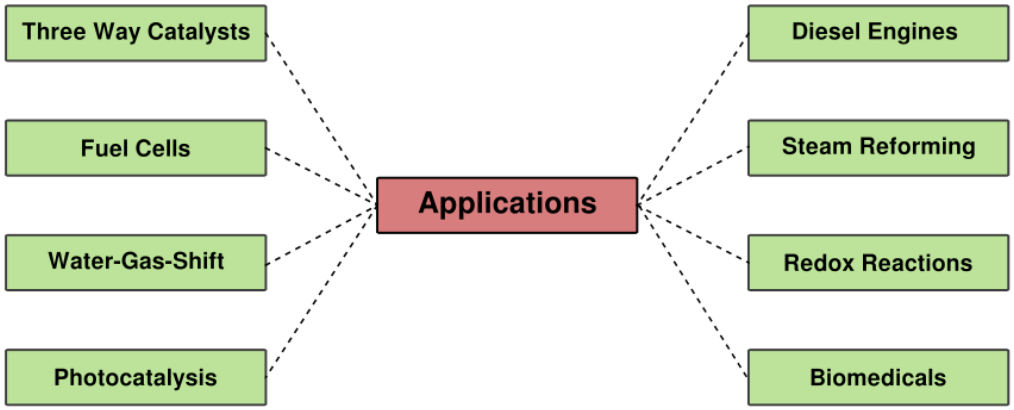

Figure 4.2: Applications of CeO_2 based catalysis in several fields.

to act as an oxygen buffer, extending the three-way 'window' (Figure 4.3 (a)).[212]

B. Diesel Engines :

Along with CO, NO_x and hydrocarbons, soot is one of the main pollutants in diesel engines which has a negative impact on the environment and human health. Several processes have been tested to reduce the soot emission and catalytic filtration is one of the advanced techniques where soot is usually oxidised.

CeO_2 based materials have been good catalysts for soot combustion, in fact, some catalytic modifications can improve the performance significantly like cobalt oxide support, rare earth -modification, Ce-Zr oxide, nano alloy support etc. Two mechanisms have been proposed so far for soot combustion by ceria-based catalysts (Figure 4.3 (b)) : (i) Active oxygen mechanism where soot is oxidised by the O present in CeO_2 and then the vacancy is filled by the supplied oxygen gas, (ii) NO_2 assisted mechanism, where NO (generated during the combustion of diesel) is firstly oxidised to NO_2 by CeO_2 and then NO_2 oxidise the soot.[213]

C. Steam Reforming :

Steam methane reforming (SMR) is the most widely used method in industries to produce hydrogen. Compared to other reforming processes, SMR produces a higher H_2/CO ratio. As is thermodynamically endothermic, it requires a higher temperature for the reaction:

$$CH_4 + H_2O \rightleftharpoons CO + 3\,H_2 \qquad \Delta H^0_{298} = +206.2\ kJ/mol \tag{4.1.6}$$

Nevertheless, a number of reports have been published on CeO_2-based catalysts for the SMR process and the amount of work has exponentially increased over the past two decades. Some of the systems used for the SMR process are noble metal supports Ru, Ni, Pt, Pd and Rh on CeO_2, a series of mixed oxides Yb_2O_3, Gd_2O_3,

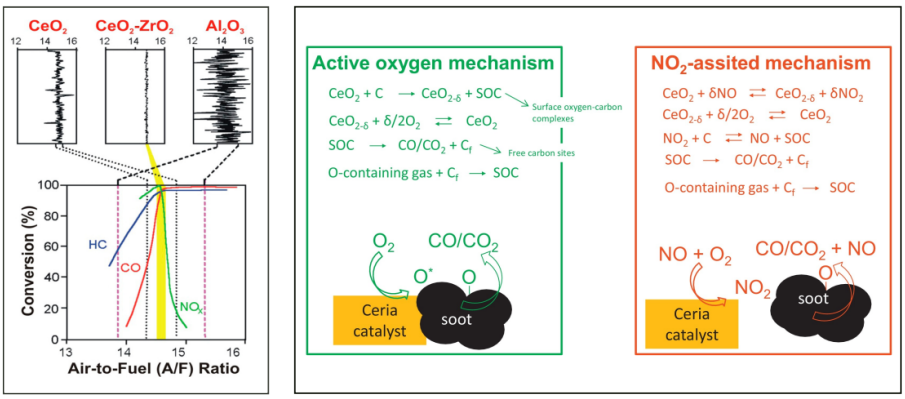

(a) TWCs (b) Diesel Engines

Figure 4.3: (a) Conversion efficiency of TWCs. Adapted with permission from Reference.[212] Copyright 2000 Elsevier. (b) scheme of soot combustion reaction mechanism on ceria-based catalysts. Adapted with permission from Reference.[213] Copyright 2014 Elsevier.

La_2O_3 etc. with CeO_2, $Ni/Ce_{0.8}Zr_{0.2}O_2$, bi-metallic support on ceria $Rh\text{-}Pt/CeO_2$, $Cu/CeO_2/ZrO_2$ and so on.

D. Water Gas Shift Reaction :

The WGS reaction has been discussed in the previous section, but it is important to note the importance of this process in the context of the SMR process. Industrial processes including methanol synthesis, Fischer-Tropsch synthesis or hydroformylation reaction require well-defined $H_2/CO/CO_2$ ratios to control the processes efficiently.

E. Oxidation of Organic Compounds :

CeO_2 and CeO_2-based materials are excellent catalysts for the conditioning of volatile organic compounds (VOC), extensively used in wastewater plants to remove organic pollutants. The reaction follows a Mars-van Krevelen (MvK) type mechanism where ceria supplies oxygen to the adsorbate and is re-oxidised by supplied oxygen. Methane is the most difficult VOC to oxidise and a major environmental hazard. A recent review on Au-based catalysts and TM metal supports has been published which has great capability for VOC combustion.[214]

F. Partial Hydrogenation :

Ceria can be a good alternative to the traditional Pd-based catalyst (Lindlar's catalyst) for partial reduction of alkynes to olefins because of its high activity, selectivity and low cost.

G. Photocatalysis :

Ceria-based materials have gained attention in the field of photocatalysis as an alternative to conventional TiO_2 for both water splitting and wastewater treatment.

CeO_2 has a wider band gap (3.2-3.4 eV) which falls in the UV range, although the presence of O vacancies and noble metal doping (Fe, Co, Mn) bring this gap into the UV/visible region.

Although ceria-supported noble/transition metals-based catalysts have found extensive use in heterogeneous catalysis, an atomic-level understanding remains elusive. Here, we briefly discuss some previous studies on ceria-based catalysts.

4.1.2.2 Au-Ceria

Historically, Au has been considered an inert material for catalytic reactions since the late 80's.[215] Haruta et al. discovered a small nanoparticle of Au supported on some oxide systems can exhibit low-temperature CO oxidation activity and be used as a catalyst in different reactions such as oxidation and WGS reactions.[216] There are many factors to decide the reactivity of Au-based catalysts like particle size, reaction condition, pretreatment conditions, support system etc. Goodman and coworkers have done a lot of research on the model reactions of Au nanoparticles (NPs) on TiO_2 support and found that the quantum size of the NPs significantly determines the reactivity.[217] Flytzani-Stephanopoulos et al. found that the whole NPs do not participate in the reaction rather the Au atoms' contact with the support is crucial as Au can be partially oxidised to $Au^{\delta+}$.[218] The interaction between Au and oxide support stabilises the NPs by increasing the contact area. A common phenomenon in these systems is oxygen vacancies on the oxide surface, which could be single, double or multiple vacancies as well as surface, subsurface or bulk vacancies. Many experimental and computation studies have been performed to determine the structure, vacancies and reaction rate of Au-based catalysis. Several DFT studies by Liu et al. show Au atoms will be adsorbed on top of O on the $CeO_2(111)$ pristine surface and O vacant site for the defective surface.[219] Au is oxidised to $Au^{\delta+}$, on the other hand, partial reduction of CeO_2 both in the absence and presence of oxygen vacancy, leading to electron transfer to the vacant $4f$ orbital of ceria. The adsorption energy of Au on different ceria surfaces suggests that the partially reduced ceria (with O vacancy) is the best support of Au compared to pure CeO_2 and completely reduced Ce_2O_3 is rather inert.[220] Au is the active site for catalysis and O vacancy does influence the process. It was also concluded that neither single Au atoms nor sizable NPs have the highest efficiency but some ultrasmall Au clusters could be very effective for catalysis. Another DFT study by Henkelman et al. on Au NPs supported by CeO_2 explained how CeO_2 with O vacancy influences the CO oxidation reaction and the adsorption

behaviour of the Au_{13} NPs.[221] The choice of the size of Au NPs determines the geometry of the structure. A pyramidal-like 3-layered Au_{13} nano cluster would be the most stable structure both for pure ceria and O vacant surface Figure 4.4.

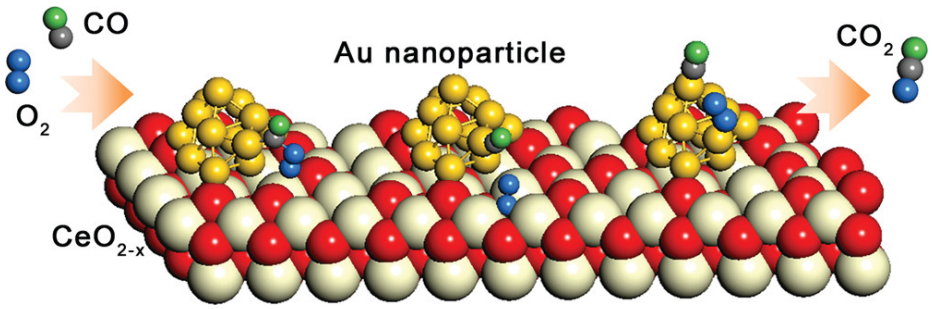

Figure 4.4: Au NPs model on supported ceria for CO oxidation. Adapted with permission from Reference.[221] Copyright 2012 American Chemical Society.

They suggested that CO and O_2 will be co-adsorbed on the Au NPs but it will follow the M-vK mechanism where CO will be oxidised by the lattice oxygen, following the oxidation of the lattice by supplied O_2. A slightly different technique was used by Rodriguez et al. where CeO_{2-y} and TiO_{2-y} nanoparticle was supported on Au(111) support for the WGS reaction.[222] It was mentioned that CeO_2/Au(111) has higher catalytic activity, and follows a lower energy path compared to Au(100) or Cu(100) and some other reported systems. They concluded that water dissociation is the rate-determining step. Kim et al. reported that the inclusion of Pd, Pt and Ti into an Au_{13} NC-supported CeO_2 can significantly improve the formation energy of oxygen vacancy and catalytic activity can be optimised.[223] A supported Au catalyst can exhibit excellent CO oxidation activity at low temperatures but suffers from Au NPs sintering under reaction conditions, resulting in rapid deactivation of the catalyst. Therefore, there are constant efforts to find new materials with anti-sintering abilities and diverse applications.

4.1.2.3 Pt-Ceria

Pt is another noble metal which has gained attention for its catalytic activity for different chemical reactions, especially the WGS reaction. Compared to Au, Pt is bound strongly with CeO_2, which minimises the sintering phenomenon and encourages Pt to disperse over the surface. However, the CO molecule has a higher binding energy with Pt, which leads to CO adsorption on the Pt site and charge transfer from the metal to the surface. A theoretical study by Bruix et al. on Pt single atom supported on pure CeO_2 suggests that Pt will bind to the bridging site of two top-layer oxygen

atoms.[224] However, the dispersion of Pt at different positions on the surface can't be ruled out. Open-shell DFT calculation shows the oxidation of Pt^0 to Pt^+ and the reduction of Ce^{4+} to Ce^{3+}. Xu et al. mentioned that the CO oxidation activity on Pt/CeO_2 comes from two aspects: 1) small-sized particles disperse over the surface to provide more active sites. 2) charge transfer from metal to the support.[225] An interesting study by Vayssilov et al. reveals how the morphology of supported oxide determines the oxygen spillover on the Pt nanoclusters (NCs).[226] Two types of CeO_2 supports for Pt_8 NC were considered. (i) CeO_2 slab and (ii) $Ce_{40}O_{80}$ nanoparticle. It has been reported that there is a significant charge transfer from the Pt_8 NC to both supports. However, the oxygen spillover from the CeO_2 to the Ru_8 NC would be preferable for the $Ce_{40}O_{80}$ NPs whereas it's energetically not favourable for the CeO_2 slab system (Figure 4.5). Two main factors that drive oxygen spillovers are the oxygen vacancy formation energy from the support and the oxygen binding energy with the Pt NC.

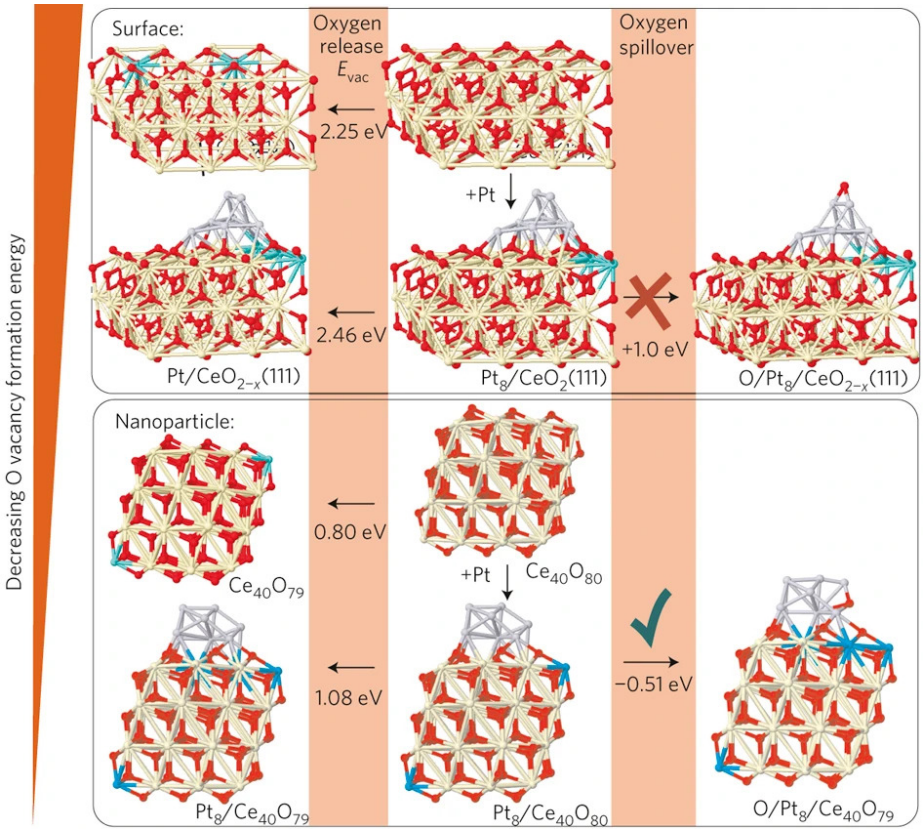

Figure 4.5: Oxygen release and oxygen spillover in extended and nanostructured Pt–CeO_2 models. Adapted with permission from Reference.[226] Copyright 2011 Nature Publishing Group UK London.

The adsorption behaviour, structure and electronic properties of Pt_8 NC on CeO_2

(111) surface were studied by Bruix et al.[227] The geometry optimisation revealed that the Pt_8 forms two layers on the support. The bottom layer contains six Pt atoms directly in contact with surface oxygens and the top layer has two Pt atoms. Vecchietti et al reported the role of oxygen vacancies on CeO_2-supported Pt cluster for WGS reaction is significant.[228] The oxygen vacancy formation energy or the supported oxide reducibility can increase the reaction rate by adsorbing the water faster. The metal-support interface plays an essential role in CO adsorption and water dissociation.

4.1.2.4 Pd-Ceria

Pd is also a very commonly used catalyst for WGS reactions and three-way catalytic (TWCs) reactions because of its low cost and excellent CO oxidation performance. Like Pt catalyst, Pd-based catalytic performance depends on the cluster size and the dispersion over the oxide surface. Sintering of the small NPs is the main reason for the degradation of catalytic performance for most of the noble metals including Pd, hence several techniques could be used to prevent it. Embedded materials can also prevent the sintering and enhance the stability and reactivity.[215] Cargnello et al. prepared Pd/CeO_2 nanostructures by self-assembly and found a good catalytic activity for CO oxidation.[229] Pd is not inert for catalytic reactions, different facets of Pd solids like Pd(111), Pd(100) etc. can have different reactivities but supported Pt can exhibit a higher reactivity for CO oxidation. The rate of CO oxidation mainly depends on the CO adsorption energy on Pd and supported Pd has a strong CO binding energy. A computational study by Yang et al. shows the existence of different adsorption features for a single Pd atom on a clean and O-vacant CeO_2 surface.[230] Pd prefers to be adsorbed at the two oxygen-bridging sites for a clean surface whereas in the reduced surface, it will be slightly away from the vacancy but the adsorption energy would be much stronger. They also concluded that oxygen removal from a Pd/CeO_2 system is much easier than a clean CeO_2 because the extra electrons can be easily accommodated at the partially occupied metal *d*-orbital and can have good oxygen storage capacity.

4.1.2.5 Other Metal-Ceria

The studies were not only restricted to Pt, Pt and Au. Some other noble metals (Rh, Ru, Ir etc.) and transition metals (Cu, Ag, Ni, Fe, Co etc.) based catalysts were investigated in the past few decades. Some model catalysts are shown in Figure 4.6.

Several journal articles have been published on Rh and Ir nanoclusters supported on oxides to act as good WGS catalysts.[231,232] The WGSR on Rh/CeO_2 catalyst

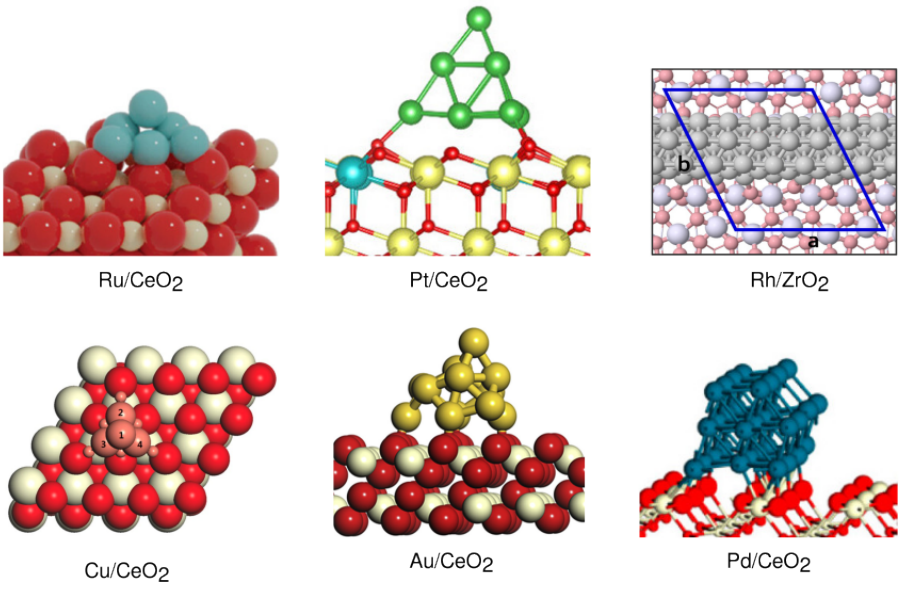

Figure 4.6: Examples of CeO_2 supported metal catalysts.

takes place at the Rh-CeO_2 interface. Catalytic activity depends on the support exclusively as Rh/CeO_2 is highly active for WGSR whereas Rh/SiO_2 is not under similar reaction conditions.[233] A theoretical investigation by Chen et al. shows that a small Rh_4 cluster can be a good catalyst for WGSR and the mechanism will follow the carboxylic pathway (*vide infra*). The adsorption of Rh_4 is favourable when it forms a layered cluster on top of oxygens on the surface.[234] Non-noble metal-based catalysts on supported oxides have caught the researchers' attention because of the lower price and similar reactivity for different catalytic reactions. Like noble metal supports, the active site for the reaction is the metal support interface and the strong metal support interaction (SMSI) promotes stability and reactivity. Due to the strong interaction between Cu and CeO_2 and the high dispersion of Cu on ceria, Cu/CeO_2 has a high catalytic activity in WGSR. Su et al. also mentioned the lattice oxygen self-spillover on the ceria-supported Cu system can increase the catalytic ability in WGSR.[235] They reported on a reducible oxide support, oxygen spillover causes a highly dispersed monolayer structure with partial reduction of Cu. This causes strong adsorption of CO at the Cu-ceria interface increasing the reaction rate. Ni supported on CeO_2 can be used as a WGS catalyst and the catalytic activity was enhanced significantly after adding a small amount of La to the surface for the catalyst.[236] Ag deposited on CeO_2 nanocubes and nanorods can influence the catalytic activity of CO oxidation. The shape of the Ag NPs and the oxygen vacancies of the oxide surface control the reactivity to a certain extent.[237] Thinon et al. compared various metals

on oxide catalysts under identical WGSR conditions.[238] The reaction temperature was 300°C and two different reactant gas compositions as shown in Figure 4.7. They reported that Pt, Au noble metals had high CO_2 production yield, whereas on Rh, Rh catalysts, produced CO_2 gas was further reduced to methane, resulting in a low yield of CO_2. The reduction process depends on the partial pressure of the mixture of gases and the activation energy barriers of the system.

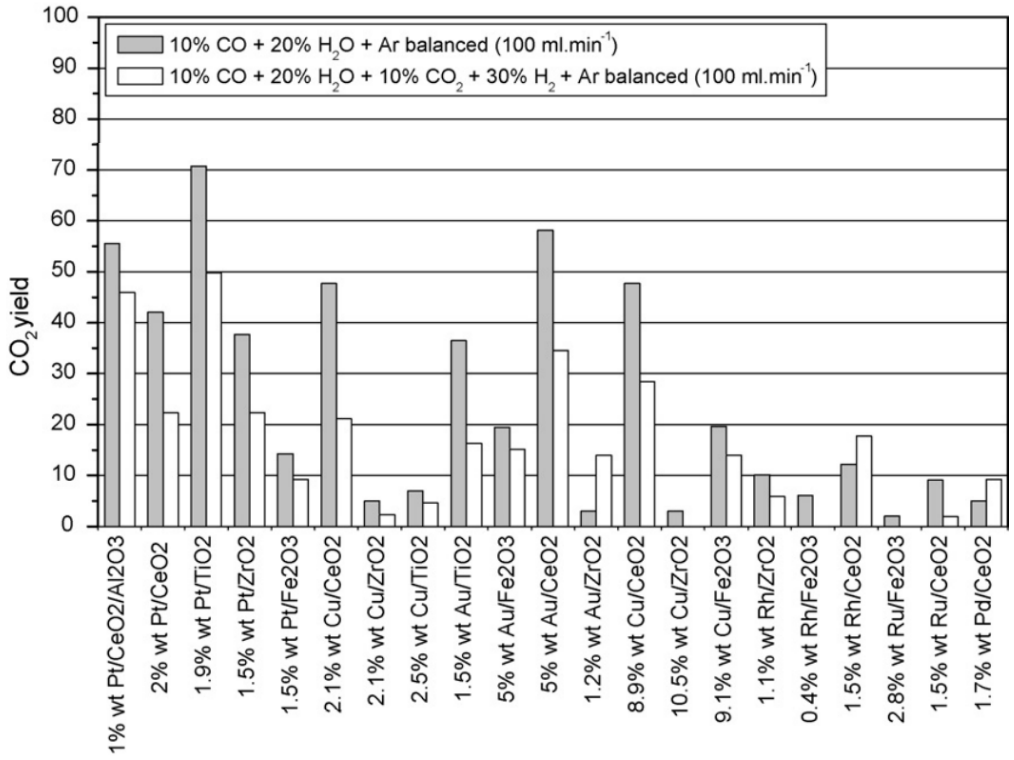

Figure 4.7: Carbon dioxide yield of various metals on oxide catalysts at 300°C. Adapted with permission from Reference.[238] Copyright 2008 Elsevier.

Although noble/transition metals play an important role in catalytic reactions, however, there are some disadvantages because of high cost and poor selectivity at high temperatures. New strategies like metal doping to support oxides and/or adding a second metal (bimetallic compound) can efficiently improve the catalytic performances.[239] Introduction of metals into the support not only improves the activity but also forms stable compounds with different physical and chemical properties such as interfacial effect, synergistic effect etc. It reduces the sintering and aggregation of noble metals. Doping of TMs and noble metals can lower the activation energy barrier of oxygen reduction, produce oxygen vacancy or defect and increase the Ce^{3+}/Ce^{4+} ratio on the support which has a great influence on catalytic activity.[215] Metals such as Co, Fe, Cu, and Pd low-valence cations can influence intrinsic oxygen vacancy on

support and increase CO oxidation. Park et al. showed that Cu-doped CeO_2 has higher catalytic activity than Ni- or Co-doped ceria.[240]

Adding a second metal can be an effective strategy to tune catalytic performance through modification of electronic and structural factors or via a bifunctional effect in which atoms of the two metals provide catalytic sites which play unique roles, such as separating the adsorption of different reactants or intermediates.[241,242] Designing a CeO_2 -supported Pd-based bimetallic system (Pd-Ag, Pd-Cu) can improve CO oxidation activity by offering different active sites.[243]

The key takeaway messages from here are how the metal nanoclusters will be adsorbed on the support and what is the role of oxygen vacancy, metal support interaction and charge transfer, which has a great impact on the structure and reactivity of the catalysts.

4.1.2.6 Ru-Ceria

Ru is also highly active for several catalytic processes and ceria-supported Ru and Ru-based bimetallic catalysts are active for WGSR.[244] Utaka et al. reported the catalytic performances of Ru, supported on different oxide surfaces for WGS reaction.[245] Since WGS is an exothermic reaction, it will be more effective at low temperatures. It is worth noting that the WGS reaction is reversible and produced CO_2 can be reduced to CO (rWGS reaction), whereas both CO_2 and CO can be reduced by the produced H_2 to CH_4 (methanation reaction). Methane is stable at low temperatures. Even though the WGSR is fast on Ru catalysts, it could be hindered by the presence of H_2. There is a competition between the CO oxidation (WGS) or reduction (rWGS, methanation etc.) processes if the catalyst is active for the methanation reaction. Some of the metal catalysts such as Ru-based ones tend to have high activity for methanation reactions. It was concluded that even though Ru has a tendency for methanation reaction, different oxide supports (ZrO_2, V_2O_3 etc) can have some activity for WGS reaction in various temperature zones and reaction conditions.

Recently, Sun et al. synthesised a CeO_2 supported Ru/Sn-based catalyst using $[Ru@Sn_9]^{6-}$ Zintl cluster as a precursor and studied the catalytic activities towards CO_2 hydrogenation reactions (rWGS and methanation).[3] The endohedral cluster dispersed over the surface and formed Ru-SnO_x bimetallic cluster, confirmed by EDX spectroscopy. A few minor peaks of $RuSn_2$ and Ru_3Sn_7 were also observed. The CO chemisorption on Ru also confirmed that the endohedral Ru atom, trapped inside the $[Sn_9]$ cage, came out and dispersed on the surface. The X-ray photoelectron spectra (XPS) showed Sn was partially oxidised and indicated direct Sn-O interaction on

the surface. STEM characterisation technique also provided the presence of isolated single Ru atoms or pseudo-clusters. However, the researchers could not manage to characterise Sn and postulated that probably the crystal structure of $[Ru@Sn_9]^{6-}$ is entirely or partially preserved after landing on the surface. Therefore, a detailed understanding of the adsorption and/or dispersion of the $[Ru@Sn_9]^{6-}$ cluster is still lacking. The schematic plot in Figure 4.8 indicates the dispersion of the cluster and the reaction site of the reaction is unknown.

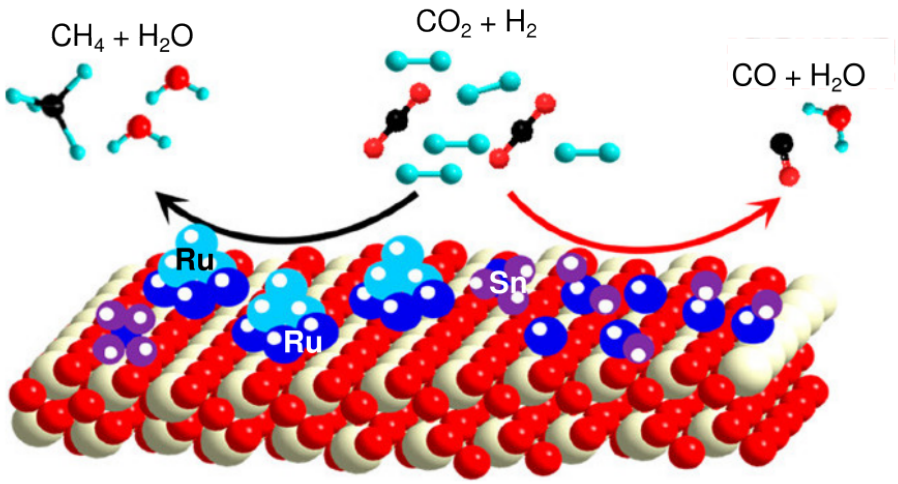

Figure 4.8: Schematic description of CO_2 hydrogenation over separated active sites of Ru NPs on top of CeO_2. Adapted with permission from Reference.[3] Copyright 2020 American Chemical Society.

The key questions to be addressed are:

1. Does the cluster remain intact after absorption, or do strong interactions between surface and adsorbate lead to monolayer formation?

2. If a monolayer is formed, what is the most favourable position for the Ru atom?

3. Is it possible to identify a smaller model (with fewer Sn atoms and therefore a smaller unit cell) which captures the essential features of the full system?

The Ru-SnO_x/CeO_2 catalyst is highly selective towards rWGS reaction over methanation reaction in CO_2 hydrogenation, but the selectivity could be switched to $\approx 100\%$ methanation by simply adding H_2O to the reaction system. With the combination of kinetic studies and *in situ* characterisations, the key reaction intermediates were captured, where carboxyl ($COOH^*$) and formate ($HCOO^*$) are the intermediates for

rWGS reaction and methanation reaction, respectively. However, a thorough computational study is required to determine the reaction mechanism and the potential energy surface of those reactions.

In this study, we adopt DFT study to investigate the stability of the $[Ru@Sn_9]^{6-}$ Zintl cluster on the $CeO_2(111)$ surface by comparing the optimised energies of the cluster on the surface with a dispersed structure where the Ru and Sn atoms are dispersed on the surface. Note that, if the cluster remains intact, it is designated as $[Ru@Sn_9]^{6-}$, and the '@' indicates the metal is encapsulated. If its charge state and structure are uncertain (as is the case for the absorbed species) the empirical formula $RuSn_9$ is used instead. In many cases, clusters prove not to be stable on the surface but rather are disrupted by strong metal-support interactions (SMSI). An important first objective therefore is to establish the stability of the $RuSn_9$ cluster on the surface under normal reaction conditions. Once this has been done, we report how the oxygen defect (vacancy) on the surface is participating to stabilise the system. Later, we investigate the reaction mechanism of the WGS reaction and CO methanation reaction on the most stable catalyst. Since the WGS reaction is a reversible process and the forward reaction is exothermic and thermodynamically more favourable in ideal conditions, we have studied the WGS reaction rather than the reverse-WGS reaction. However, the potential energy surface remains the same, only the direction of the reaction changes.

4.2 Computational Details

Spin-polarised Density Functional Theory (DFT) calculations were performed to investigate the optimised structure and potential energy surface for all the elementary steps in the WGS and CO methanation reactions on the $CeO_2(111)$ surface, utilising the Vienna Ab initio Simulation Package (VASP) code.[246,247] We used a plane wave basis set and the projector augmented wave (PAW) method to describe the interaction between valance electron and atomic cores.[248] To accurately treat the highly localized Ce $4f$ orbitals and correct the self-interaction energy, we applied the Hubbard-correction term (U) with a value of $U_{eff} = 5.0$ eV to the Ce $4f$ states.[249] This U_{eff} value was reported to describe the electronic structure of reduced ceria in previous studies.[250,251] The exchange and correlation were treated within the generalised gradient approximation (GGA) using the Perdew-Burke-Ernzerhof (PBE) functional, as apllied in several journals.[124,252] The valence electron density of all the atoms is, for Ce: twelve ($5s^2$, $5p^6$, $6s^2$, $5d^1$, $4f^1$), O: six ($2s^2$, $2p^4$), Ru: eight ($5s^1$,

$4d^7$), Sn: four ($5s^2$, $5p^2$) H: one ($1s^1$) and C: four ($2s^2$, $2p^2$). Two sets of supercells were constructed to reduce the computational cost, especially for the transition state calculation, and different values in a few parameters were set: (i) 3×6×1 supercell to study the stability and absorption of $RuSn_9$ cluster on CeO_2 surface (big cell), ii) 2×4×1 supercell to study the reaction mechanism of WGS and CO methanation reaction (small cell) (Figure 4.9). The kinetic energy cut-off was chosen to 510 eV for a 3×6×1 cell and 400 eV for a smaller one to describe valence electrons by plane wave basis, as reported in journals.[253,254] The reciprocal space was sampled using a 2×2×1 Monkhorst pack special k-point grid and the Gaussian smearing with sigma value 0.1 eV was applied for electronic optimisation for bigger cell whereas, gamma-centred 1×1×1 k-point was used with a lower sigma value of 0.05 for the smaller cell.[252,255] The electronic structure and geometry optimisation calculations ran until they reached the convergence threshold of 10^{-5} eV and 10^{-3} eV, respectively. Force convergence, using a tolerance of 0.01 eV/Å threshold was considered wherever needed (to verify the accuracy). Transition states (TSs) for the elementary reactions were located using the climbing-image nudged elastic band method (CI-NEB) and were confirmed as having a single imaginary frequency.[256,257]

The adsorption energy is defined as

$$E_{adsorption} = E_{(surface+adsorbate)} - E_{(surface)} - E_{(adsorbate)} \tag{4.2.1}$$

where $E_{(surface+adsorbate)}$ is the total energy of the adsorbate interacting with the surface; $E_{(surface)}$ and $E_{(adsorbate)}$ are the total energies of the bare surface and free adsorbate in the gas phase, respectively.

A stoichiometric O-terminated CeO_2(111) surface was obtained by a slab-cutting process. Firstly, the unit cell of bulk cubic ($Fm\bar{3}m$) CaF_2-like optimised structure with lattice parameter 5.40 Å was taken and a (111) slab was cut out.[258] The supercell was modelled by transforming the unit cell to 3×6×1 and 2×4×1 supercells to make the surface approximately square and large enough to avoid interaction with neighbouring cells. Nine atomic layers (3 ML) were considered and only the uppermost 3 atomic layers (1 ML) were allowed to relax. A 16 Å vacuum gap was imposed in the supercell to avoid interactions between periodic images along the z-axis.

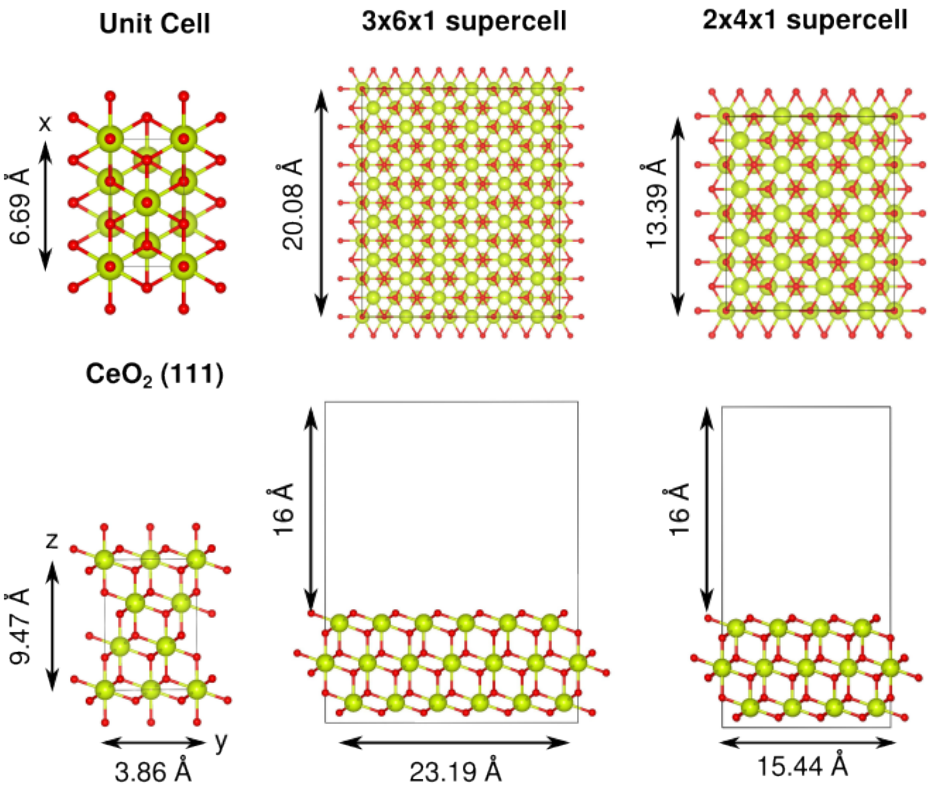

Figure 4.9: Computational models of different size of $CeO_2(111)$ supercells. The big cell (3×6×1) is for studying the adsorption behaviour of $RuSn_9$ on the CeO_2 surface and the smaller cell (2×4×1) to study the oxygen defect and reactivity of the catalyst.

4.3 Adsorption of $[Ru@Sn_9]^{6-}$ on $CeO_2(111)$

In this section, we build up a model for the absorbed Zintl cluster on a CeO_2 surface. We begin by considering the absorption of Sn atoms and clusters, where there is some literature precedent to compare to, and then introduce the Ru atom in a second step.

4.3.1 Adsorption of Sn atoms

Zhao et al. have previously reported a DFT study of the adsorption of up to 4 atoms of Sn on a $CeO_2(111)$ surface.[252] For a single Sn atom, they concluded that the hollow position in the middle of three O atoms proves to be the preferred adsorption site rather than the top of oxygen on the surface (Figure 4.10 (**a**)). However, with increasing surface coverage by two or more Sn atoms, this preference is reversed, favouring the 'on top of O' configurations, shown in Figure 4.10. Their study was focused on the monolayer structures where all Sn atoms make contact with the surface,

but a key question that we seek to answer here is whether the $RuSn_9$ system absorbs as a mono-layer or as an intact 3-dimensional cluster. As a precursor to this, we have extended the work reported by Zhao to compare monolayer vs 3-dimensional cluster absorption for Sn_x clusters, and also expanded the scope of the study to include up to 5 Sn atoms. The lowest energy structures found for one (a and b), two (c), three (d), four (e and f) and five (g, h and i) Sn atoms are collected in Figure 4.10 and various energetic parameters are collected in Table 4.1. Where comparison is possible, the results for the smaller clusters are fully consistent with Zhao's work.[252]

Table 4.1: Adsorption energies (E_{ads}) and total and average (per Sn atom) Sn-Sn cohesive energies (E_{Sn-Sn}) of x Sn on the $CeO_2(111)$ surface.

Figure 4.10	configurations	E_{ads}/eV	$E^{total}_{coh(Sn-Sn)}$/eV	$E^{av}_{coh(Sn-Sn)}$/eV
(a)	1Sn-hollow	-4.78		
(b)	1Sn-1O_top	-2.42		
(c)	2Sn-2O_top	-6.17	-1.32	-0.66
(d)	3Sn-3O_top	-9.74	-2.47	-0.82
(e)	T_d-Sn_4 cluster	-11.98	-4.71	-1.18
(f)	4Sn-4O_top	-13.87	-4.17	-1.04
(g)	5Sn-5O_top	-17.51	-5.39	-1.08
(h)	1Sn_top_4Sn (middle)	-16.16	-6.48	-1.29
(i)	1Sn_top_4Sn (edge)	-15.94	-6.26	-1.25

As reported by Zhao, a single Sn atom prefers to bind to the 3-fold hollow position on the surface (**a**, -4.78 eV), with the alternative position on top of surface oxygen (**b**) over 2 eV less stable (ΔE_{abs}= -2.42 eV). The Sn-O bond length in **b** is 1.98 Å compared to 2.18 Å for **a**. For two Sn atoms, however, the preference switches to the on-top sites, which allows the two Sn atoms to form a direct Sn-Sn bond (this is not possible in the hollow sites because the Sn atoms are too deeply embedded in the surface). We can estimate the strength of the Sn-Sn interaction by defining the cohesive energy through the following equations:

The total adsorption energy, E_{ads} and Sn-Sn cohesive energy, $E_{coh(Sn-Sn)}$, are defined using the equations below:

$$E_{ads} = E_{xSn/surface} - (E_{surface} + xE_{Sn})$$
$$E_{Sn-O} = E_{ads(1Sn-1O_{top})} - (E_{surface} + E_{Sn})$$
$$E^{total}_{coh(Sn-Sn)} = E_{ads} - x'E_{Sn-O}$$
$$E^{av}_{coh(Sn-Sn)} = E^{total}_{coh(Sn-Sn)}/x$$

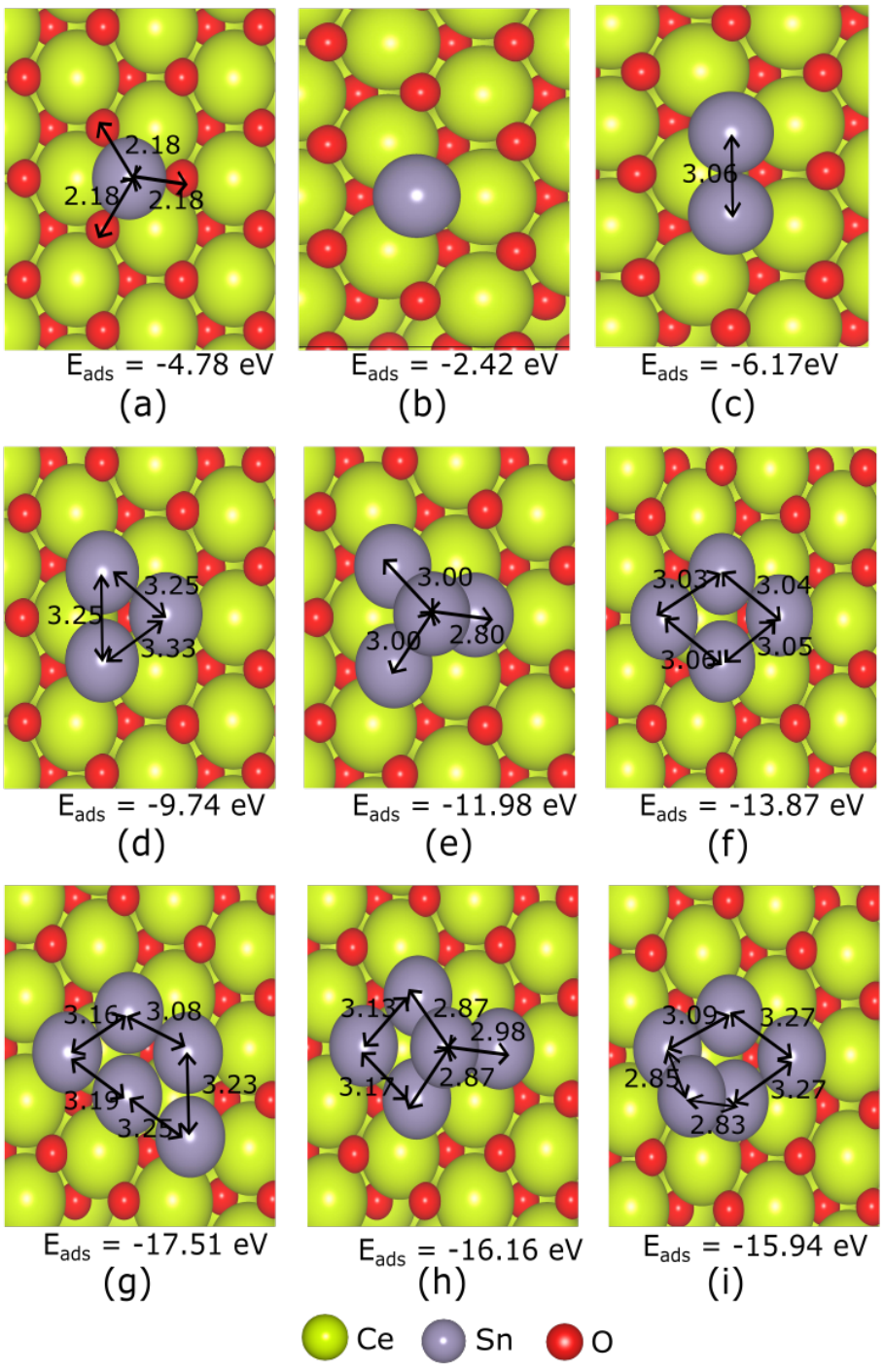

Figure 4.10: Lowest energy structures for different number of Sn adsorbed on the CeO_2(111) surface: (a) 1Sn-hollow, (b) 1Sn-1O_top, (c) 2Sn-2O_top, (d) 3Sn-3O_top, (e) tetrahedral Sn_4 cluster, (f) 4Sn-4O_top, (g) 5Sn-5O_top, (h) and (i) 1Sn_top of 4Sn.

where $E_{xSn/surface}$ is the total energy of the system with x Sn atoms adsorbed on the surface. $E_{surface}$ is the energy of the pristine CeO_2 surface and E_{Sn-O} is the energy change when a single Sn atom is absorbed on top of a surface oxygen, -2.42 eV (model (**b**) in Figure 4.10). The Sn-Sn cohesive energy, $E^{total}_{coh(Sn-Sn)}$, is then defined as the total absorption energy minus the sum of the energies of the Sn-O bonds formed, where 'x'' denotes the number of Sn-O bonds formed whereas 'x' refers the total number of Sn. We assume here that the Sn-O bond energies are independent of the surface coverage (-2.42 eV in each case). If the Sn atoms are infinitely separated on the surface, then $E^{total}_{coh(Sn-Sn)}$ would be zero, so the value reflects the extent to which the Sn atoms interact with each other. The average Sn-Sn cohesive energy, $E^{av}_{coh(Sn-Sn)}$ is defined by the amount of Sn-Sn interaction energy felt by a single Sn atom. For the Sn_2 system (**c**), the total Sn-Sn cohesive energy is -1.32 eV, indicating a strong residual Sn-Sn bonding interaction each Sn atom contributes -0.66 eV.

For 3 Sn atoms, the most stable structure has a triangle of Sn atoms, all sitting on top of surface O sites (Figure 4.10 **d**). In this case, the total cohesive energy is -2.47 eV, or -0.82 eV per Sn atom, with more Sn-Sn bonding interactions. For the Sn_4 system, we have considered two possible configurations, (**e**) a tetrahedral Sn_4 cluster adsorbed on the surface and (**f**) a monolayer structure. The monolayer, **(f)**, is -1.89 eV more stable than the intact cluster, **(e)**, and the Sn-Sn cohesive energy of (**f**) is -1.04 eV per Sn atom, higher than the Sn_3 as the number of Sn-Sn interactions has increased. The total cohesive energy of the tetrahedral Sn_4 cluster (**e**) is greater, at -4.71 eV than the monolayer (**f**), -4.17 eV. But the extra Sn-O bonding for monolayer (**f**), stabilises the structure. Similar patterns emerge for Sn_5, where the most stable isomer, (**g**), is a monolayer with 5 Sn atoms on top of surface O sites. Alternative structures with one Sn atom on top of a Sn_4 monolayer are less stable, again by approximately 1.5 eV, despite the greater Sn-Sn cohesive energy provided by the larger number of Sn-Sn interactions. The data collected in Figure 4.10 and Table 4.1 indicate that the stability of the surface-absorbed clusters is a compromise between Sn-O bond formation, favouring monolayers, and Sn-Sn bonding interactions, favouring intact clusters. Clearly, in these systems, the Sn-O bond formation dominates, and monolayers prevail. Similar compromises are apparent in related studies on transition metal clusters, where, for example, the Pt_8 cluster prefers to form a double layer on a $CeO_2(111)$ surface, the bottom layer consisting of 6 Pt with 2 Pt sitting in 3-fold positions above this.[227] Likewise in Ru_6 on CeO_2, 1 Ru sits on top of the Ru_5 layer surface.[259]

The highly localised nature of the $4f$ orbitals of Ce provides a convenient measure of the degree of charge transfer between the adsorbate and the surface. Ce^{4+} has no f electrons and hence no spin density, and so reduction of the surface is immediately obvious from the formation of Ce^{3+} ions which have characteristic spin densities close to 1.0. By monitoring the number of such sites, we can estimate the degree of charge transfer from the cluster to the surface. Zhao noted (up to 4 Sn) that the degree of reduction of CeO_2 increases with Sn coverage, with an approximate 1:1 ratio between the number of Sn atoms bound to the surface and the number of reduced Ce centres.[252]

$$x\mathrm{Ce}^{4+} + x\mathrm{Sn} \rightarrow x\mathrm{Ce}^{3+} + x\mathrm{Sn}^{+}$$

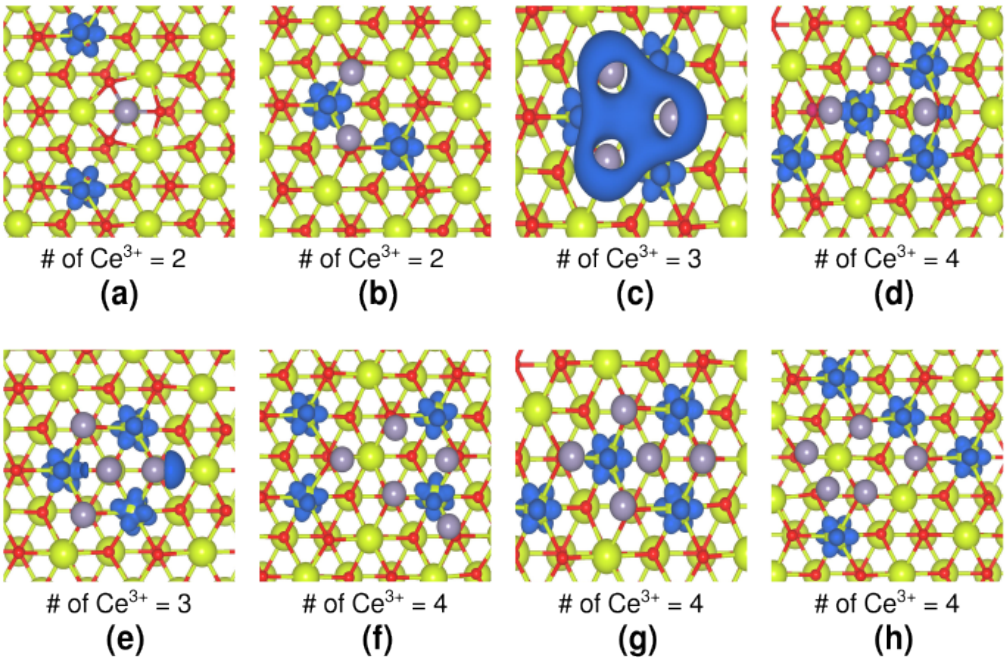

Figure 4.11: Spin density for the xSn/CeO_2(111) configurations.

Similar charge transfer behaviour has been observed in the systems shown in Figure 4.11, with the 1:1 ratio persisting in the 4-atom clusters. The reduced Ce^{3+} ions have spin density (blue) that has the characteristic 8-lobed shape of an f_{xyz} orbital. For 3 Sn, partial spin has been found on the Sn atoms, suggesting 3 electrons are transferred to the surface and the Sn_3 appears to have unpaired electrons, however, the degree of reduction of the surface is consistent. For the 5-atom monolayer, structure (**g**), however, we find only four reduced Ce sites on the surface, (even number of electrons are transferred) which suggests that the extent of charge transfer is, ultimately, limited by the accumulation of positive and negative charges on the absorbate

and surface sites. We explore this issue in more detail in the following discussion of the $RuSn_9$ cluster.

4.3.2 Adsorption of $RuSn_9$ Cluster

In Sun's experimental investigation, an anionic $[Ru@Sn_9]^{6-}$ Zintl cluster was used to prepare the highly dispersed $Ru-SnO_x/CeO_2$ catalyst, but the extent to which the cluster remains intact when on CeO_2 is not clear.[3] The $[Ru@Sn_9]^{6-}$ endohedral Zintl cluster has a *closo* tri-capped trigonal prismatic geometry with D_{3h} symmetry where the anionic cluster is stabilised by counter cations (K^+). The total formal charge distribution of the cluster $[Ru^{2-}@{Sn_9}^{4-}]$ implies a d^{10} configuration of the Ru metal.[38] The empty ${Sn_9}^{4-}$ cluster has C_{4v} symmetry, although the structural and energetic difference between this and the tri-capped trigonal prism is marginal. Clearly, the presence of a metal at the centre of the cluster favours the more symmetric D_{3h} geometry. A similar trend has been noted in $[Au@Pb_{12}]^{3-}$, which has an electron count consistent with a *nido* geometry ($4n + 4$), but instead adopts a distorted *closo* structure.[52] The structure of the cluster after absorption on the CeO_2 surface is, however, ambiguous. As noted previously, spectroscopic measurements have confirmed the dispersion of the cluster homogeneously over the surface and the data has been interpreted as showing the presence of smaller fragments such as $RuSn_2$, Ru_3Sn_7 as well as isolated Ru centres and/or Ru-Sn bimetallic compounds. There is no strong evidence of a soft landing of the $[Ru@Sn_9]^{6-}$ cluster where the structure remains intact. The purpose of this section is therefore to probe the most stable structures of $RuSn_9$ on a $CeO_2(111)$ surface.

We have optimised geometries for the $CeO_2(111)$ surface with an intact, approximately D_{3h}-symmetric, $Ru@Sn_9$ cluster (**A** in Figure 4.12) and also with a range of different planar raft-like structures where all 9 Sn atoms make direct contact with the CeO_2 surface (**B** - **E** in Figure 4.12).

For the raft-like structures, there are a number of possibilities for the position of Ru, which may be adsorbed on the CeO_2 surface at the edges of the Sn_9 island or, alternatively, on top of thereof, maximising the number of contacts to Sn atoms. Specifically, we have considered four distinct raft-like geometries where, in all cases, the Ru and Sn atoms sit on top of O atoms on the CeO_2 surface, as the Sn atoms do in the most stable geometries of the Sn_x clusters described in the previous section. In the structural family denoted **B**, the 10 atoms of the cluster form a triangular 'island', with all 10 atoms making direct contact with the surface. There are then three possible positions for the Ru atom: in the centre (1**B**), on a vertex (2**B**) or

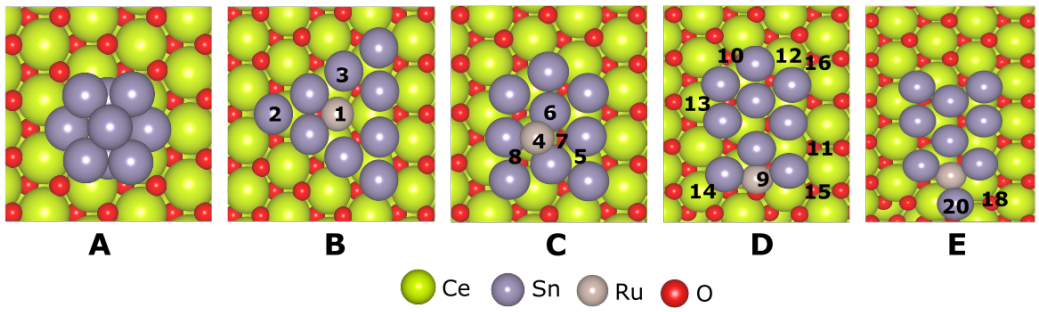

Figure 4.12: Different $RuSn_9$ models after absorption on the surface. **A**: the intact cluster, **B**: a symmetric triangular $RuSn_9$ 'island', **C**: Ru on top of a Sn_9 mono-layer, **D**: Ru at the edge of the Sn_9 mono-layer and **E**: less compact $RuSn_9$ monolayers, coordinated by higher number of Sn. The numbers correspond to the position of the Ru atom for the different models.

along an edge (3**B**), in figure 4.12. In the structural family **C**, only the 9 Sn atoms make contact with the surface, and the Ru atom sits on top of the Sn_9 monolayer, maximising the number of Ru-Sn bonds. Again, there are different possibilities, labelled 4**C** - 8**C** in Figure 4.12. In the structural family **D**, we retain the same Sn_9 motif as in **C**, but now Ru is absorbed at the junction of the Sn_9 island and the CeO_2 surface. Finally, structural family **E** contains a number of alternative structures where the Sn_9 island is less compact.

4.3.2.1 Model A: Intact Ru@Sn_9 Cluster

Absorption of the cluster onto the surface starting from a geometry where the Ru@Sn_9 cluster is intact, leads to a local minimum on the surface with a similar spherical structure, but distorted and cannot retain the symmetry. The cluster bonds to the surface via four Sn atoms, each of which sits on top of a surface O atom (Sn-O = 2.06 - 2.14 Å). The Sn-Sn bonds adjacent to the CeO_2 surface are elongated (3.18 - 4.42 Å) and the average Sn-Sn bond distance is $\sim$ 3.34 Å, higher than the isolated cluster (3.05 - 3.14 Å). It indicates a strong metal support interaction and the unstable nature of the cluster on the surface. The transfer of charge from the absorbed cluster to the CeO_2 surface that was highlighted for the Sn_x clusters is also apparent here: an analysis of the spin densities shows that three Ce ions have been reduced from the +4 to +3 charge state. For comparison to the other structural models, the energy of the intact cluster model **A** is taken as the reference ($E = 0$).

4.3.2.2 Model B: Symmetric Triangular Island

In this model, all 10 atoms (9 Sn and Ru) are in direct contact with the surface, forming a monolayer, and there are three possible positions for the Ru atom, (1**B**) Ru at the centre, surrounded by 6 Sn atoms, (2**B**) Ru at the vertex of the triangle, and (3**B**) Ru on one of the edges. The three models differ in the balance between Ru-Sn and Sn-Sn bonding: 1**B** maximises the number of Ru-Sn contacts while 2**B** maximises the number of Sn-Sn contacts. The optimised structures and relative energies of these submodels are shown in Figure 4.13.

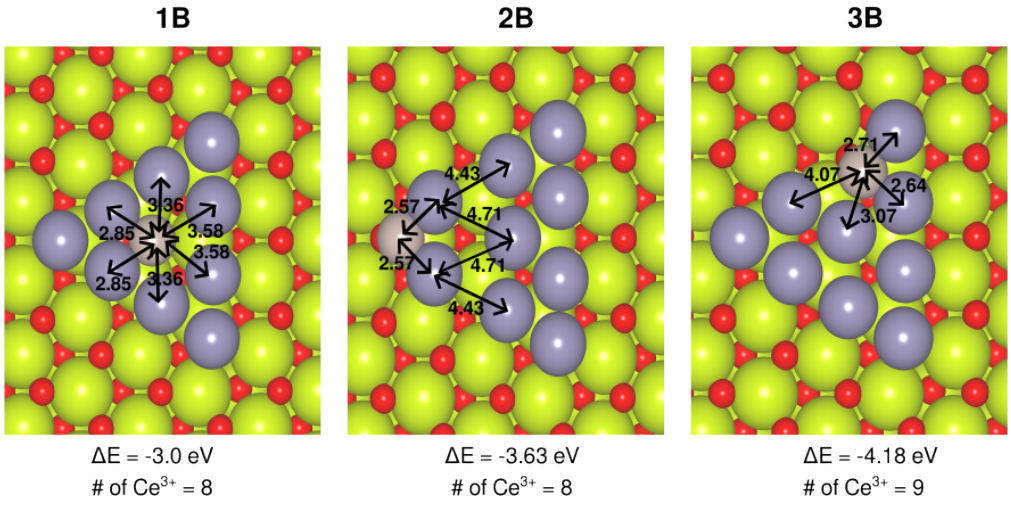

Figure 4.13: Optimised structures, bond distances (in Å) and the number of reduced Ce atom(s) of the submodels of the model (**B**): a symmetric triangular 'island' after dispersion.

The first point to note is that all three models from the B family are substantially ($>$ 3 eV) more stable than the intact cluster model, **A** - this offers an immediate indication that absorption of the cluster in its intact structure is unlikely. The increased number of Sn-O and Ru-O bonds in structures 1**B** - 3**B** compared to the intact cluster, **A**, also leads to a much higher degree of charge transfer, and we find either 8 or 9 Ce ions are reduced from the +4 to the +3 state, these ions being located in the region of the surface just below the absorbed cluster. This is consistent with the trend noted by Zhao for Sn_{1-3} and extended to Sn_4 and Sn_5 in the previous section, where there is an approximate 1:1 ratio between the number of Sn-O bonds formed and the number of reduced Ce ions in the surface layer. The most stable of these structures, 3**B**, corresponds to the maximum degree of charge transfer (9 Ce^{3+} ions), suggesting that the charge transfer is an important driver of stability. The

geometries of the optimised structures also indicate that the Ru atom forms 2 or at most 3 strong bonds (< 3 Å) to the Sn atoms, with any additional Ru-Sn contacts being rather longer. The Sn atoms directly bonded to the Ru also tend to separate from the remainder of the Sn_x raft by around 4.5 Å, perhaps reflecting the polarity of the Ru-Sn bonds.

4.3.2.3 Model C: Ru on Top of Sn_9 Monolayer

In this model, a Sn_9 monolayer is absorbed on the CeO_2 surface, with Ru seated in several positions on top of the monolayer. Optimised structures and energies are shown in Figure 4.14. All four structures, 4**C**, 5**C**, 7**C** and 8**C** have the Ru in a 3-fold site on the Sn_9: attempts to locate a minimum with Ru on top of a single Sn atom (6**C** in Figure 4.12) led instead to rearrangement to one of the structures shown in Figure 4.14. The Ru-Sn bond distances are very similar in all four models (2.47 Å to 2.57 Å) and are significantly shorter than those found in the **B** structural family. Charge transfer from the cluster to the surface is again significant: 8 Ce^{4+} ions close to the cluster are reduced to Ce^{3+}.

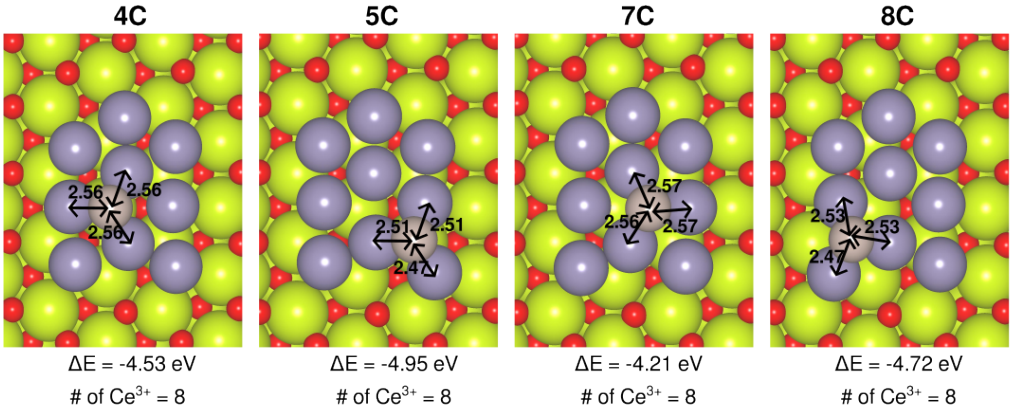

Figure 4.14: Optimised structures, bond distances (in Å) and number of reduced Ce atom(s) of the submodels of model (**C**): Ru on top of Sn_9 monolayer.

4.3.2.4 Model D: Ru Edge of Sn_9

In model **C**, the Ru atom sits on top of the Sn_9 layer, whereas in model **D** it is placed at the junction of the Sn_9 layer with the CeO_2 surface. The possible sites are shown in Figure 4.12**D**, numbered 9-16, and the optimised geometries of the lowest-energy structures are shown in Figure 4.15. Three distinct types of Ru-Sn interactions have

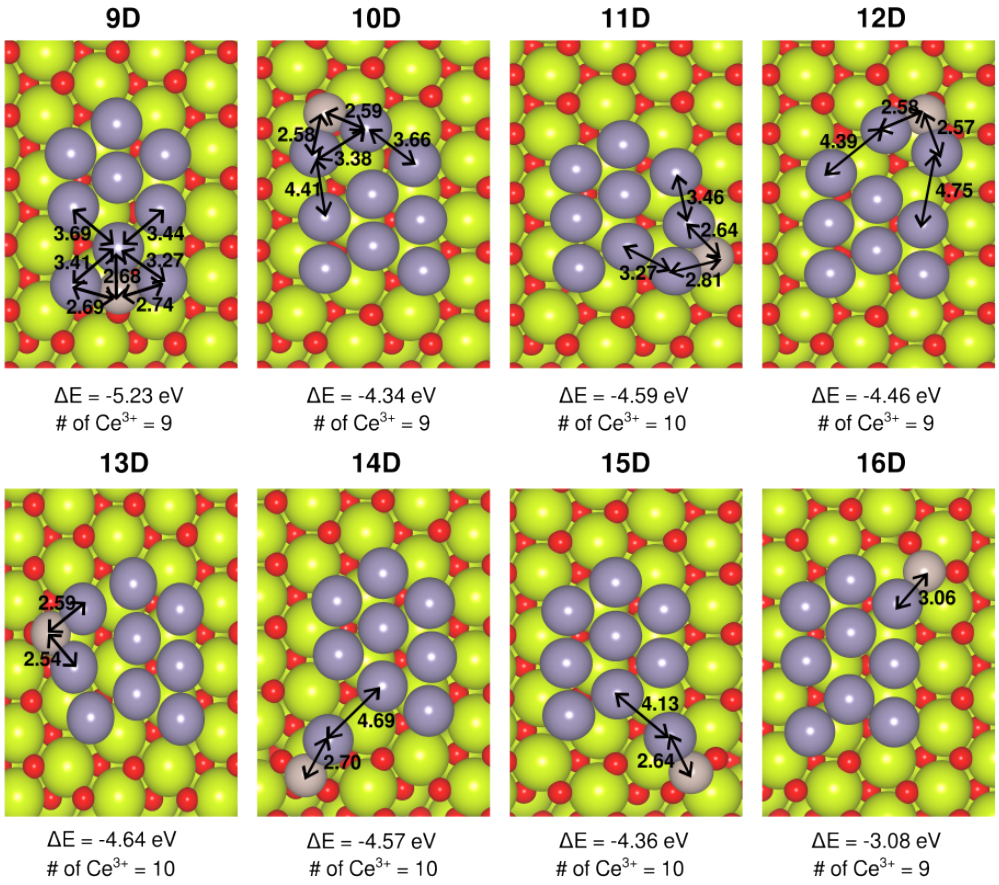

Figure 4.15: Optimised structures, bond distances (in Å) and number of reduced Ce atom(s) of the submodels of the model (**D**) where Ru is positioned at different edging sites of the Sn_9 layer.

been considered (i) Ru surrounded by 3 Sn, 9**D** (ii) Ru bonded to 2 Sn atoms (10-13**D**) and (iii) Ru bonded to a single Sn atom(14-16**D**).

The shift of the Ru atom to a position where it makes direct contact with the CeO_2 surface enhances the degree of charge transfer, and we find that either 9 or 10 Ce ions are reduced to the +3 charge state. We also note again the tendency of the Sn atoms directly bonded to the Ru to separate from the others that were apparent in structural family **B**. The most stable of these structures is 9**D**, and indeed this proves to be the most stable motif amongst all the possibilities that we have considered, with an energy 5.29 eV below the reference point, structure **A**. In 9**D**, the Ru is coordinated to three Sn atoms with bond lengths of 2.68 - 2.74 Å, and the $RuSn_3$ is separated from the residual Sn_6 island at Sn-Sn distances of about 3.5 Å. The $RuSn_3$ motif in 9**D** is rather similar to that in the most stable member of the **B** family, 3**B**.

The charge transfer from the cluster to the Ce ions in the surface has been empha-

sised as an important driver of stability, and the distribution of these reduced Ce ions relative to the absorbed cluster is shown in Figure 4.16(a) for the most stable isomer, 9**D**. The reduced Ce^{3+} ions have spin density (blue) that has the characteristic 8-lobed shape of an f_{xyz} orbital and the reduced Ce atoms are very close (underneath) to the Sn. The projected density of states shows a prominent majority-spin Ce $4f$ peak below the Fermi level, confirming the reduction of these ions. The five Ce atoms that sit directly under the Sn_9 island are all reduced, as are four additional nearest neighbours. The localisation of charge in the vicinity of the absorbed cluster suggests that electrostatic interactions between the net negatively charged CeO_2 surface and the net positively charged cluster play an important role in the stability of these structures.

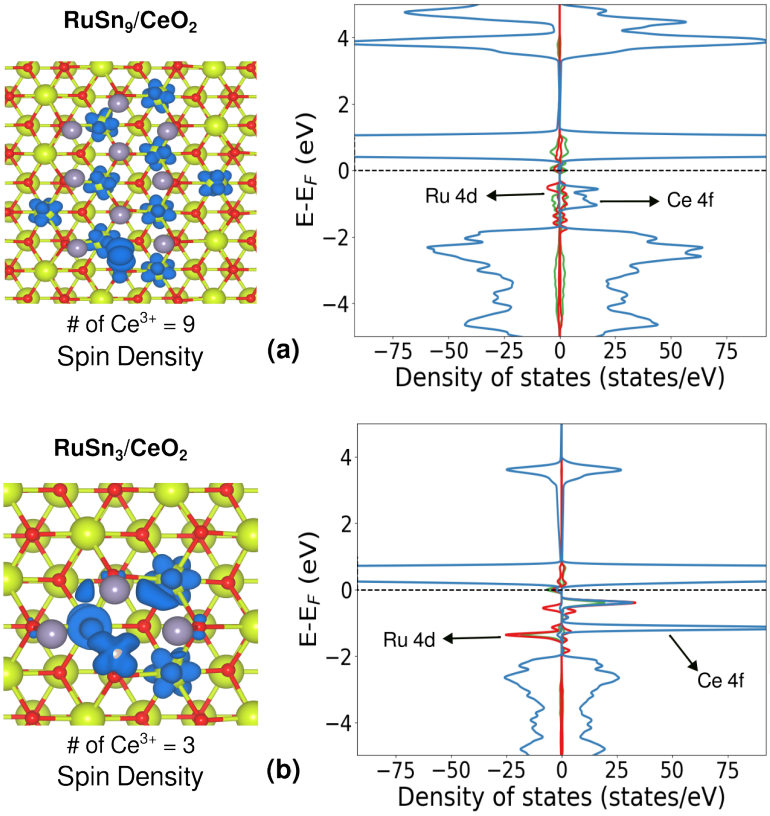

Figure 4.16: Spin Density and Projected Density of States (PDOS) of (a) model 9**D** and (b) the smaller model, $RuSn_3$.

4.3.2.5 Model E: Ru Coordinated by a Higher Number of Sn

Prompted by the stability of 9**D**, in a final step we have searched for other arrangements of Ru and Sn on the surface that contain the stable $RuSn_3$ motif or higher

coordination of Ru. These are collected in family **E**, Figure 4.17. Amongst these, the

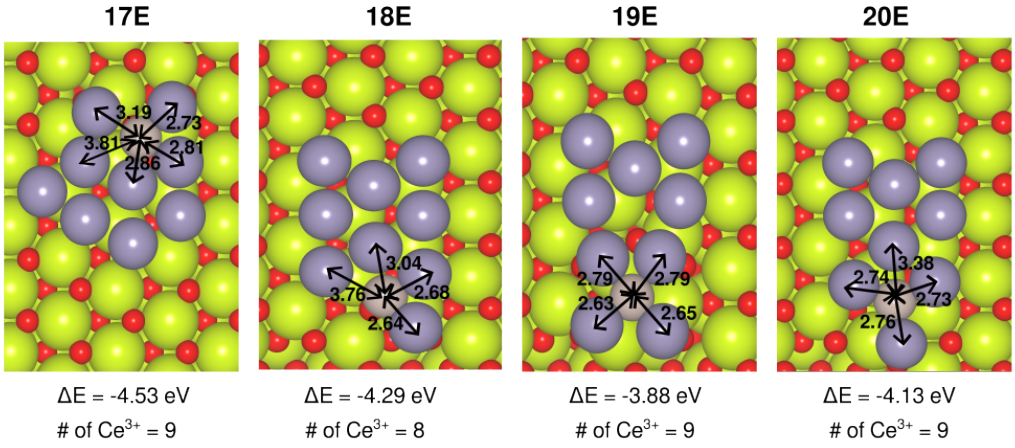

Figure 4.17: Optimised structures, bond distances (in Å) and number of reduced Ce atom(s) of the submodels of model **E**: Ru coordinated by a higher number of Sn .

most stable in model 17**E** (ΔE= -4.53 eV), where again we find the $RuSn_3$ unit with Ru-Sn bond lengths between 2.73 Å and 2.81 Å, but the residual Sn_6 unit is less compact than in 9**D**, with fewer Sn-Sn bonds. The characteristic transfer of 9 electrons to the CeO_2 surface is common to 17**E**, 9**D** and 3**B**, the most stable members of their class. Structurally, 9**D**, 17**E** and 3**B** are simply related by the shifts of one or more Sn atoms: this is most obvious for the 17**E** - 3**B** comparison, where translation of the Sn atom at the top left of 17**E** to the apex position at the bottom right generates 3**B**.

The energies of all structures from the **A**, **B**, **C**, **D** and **E** families are summarised in Figure 4.18. The most stable structure of each model are shown in Figure 4.19. All of the possible structures of a dispersed (raft-like) cluster are more stable than an intact (approximately spherical) $RuSn_9$ cluster by > 3.0 eV (per unit cell). Amongst all the structures considered, 9**D** (shown in Figure 4.12) is the most stable, and the motif where a Ru atom makes direct contact with the CeO_2 surface and 3 Sn atoms in a T-shaped geometry is common to the most stable members of families **B** (3**B**), **D** (9**D**) and **E** (17**E**). A rather different geometry, 5**C**, is also relatively stable, where the Ru atom again contacts three Sn atoms (now in a facial geometry) but does not bond directly to the surface. The relative flatness of the potential energy surface suggests that the Ru atom may have some degree of mobility over the Sn 'island' under catalytic conditions.

The computed energies discussed above appear to resolve the debate about the presence (or otherwise) of intact clusters on the surface - energetically these are very unfavourable. We can explore the origins of the stability of the monolayers (**B** - **E**)

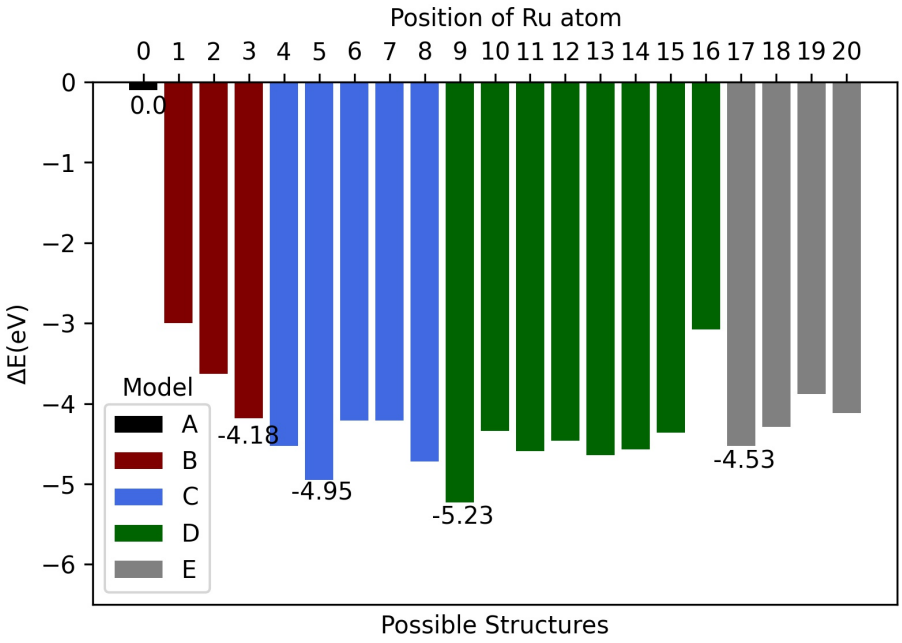

Figure 4.18: Relative energy plot of all the model isomers w.r.t the intact cluster model (**A**).

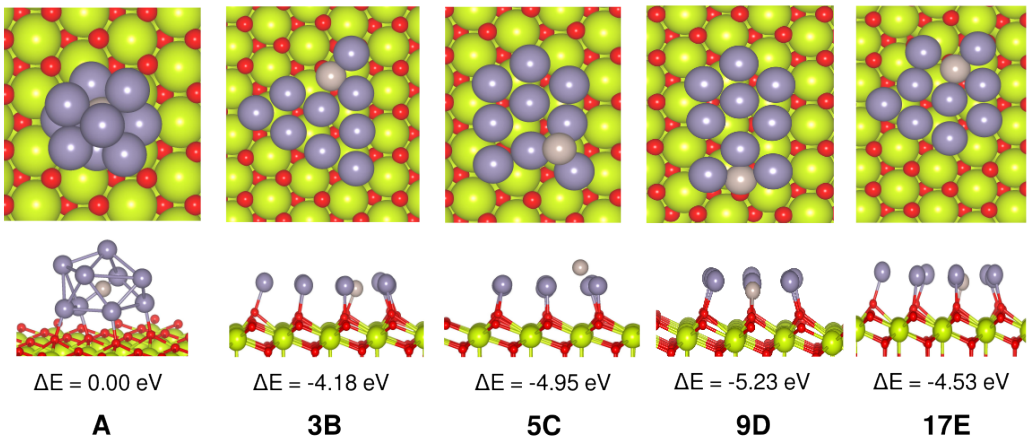

Figure 4.19: Most stable structure of **A**, **B**, **C**, **D** and **E** families. (top and side view)

through the energy cycle laid out in Figure 4.20. In this figure, the energies of isolated clusters correspond to single-point calculations carried out at the geometries that the (neutral) clusters adopt when absorbed on the surface.

The total energy difference of 5.23 eV between models **A** and 9**B** can be decomposed into the sum of the dissociation and rearrangement of the cluster from the compact 3-dimensional structure to the monolayer (+7.89 eV in the gas phase) and then re-absorption of the monolayer (-16.60 eV) minus the adsorption of the intact

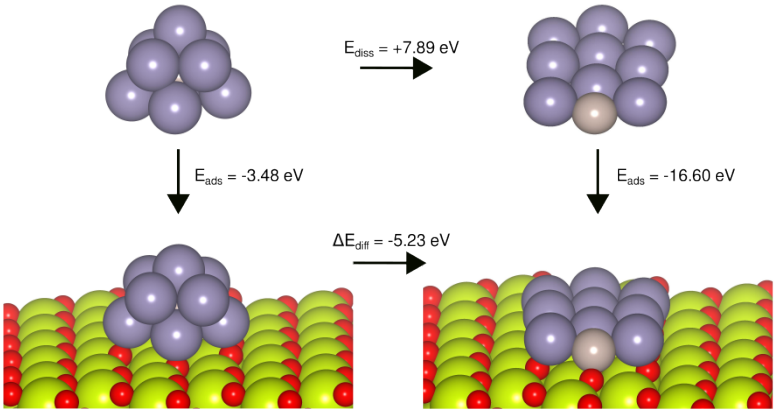

Figure 4.20: Schematic model to analyse the dispersion of $Ru@Sn_9$ cluster to form a monolayer in terms of energies.

cluster (-3.48 eV). It is clear that the rearrangement from the 3-dimensional form to the monolayer is very unfavourable in the gas phase, but this is more than compensated for by the high interaction energy of the monolayer which, as we have noted above, is driven by the strong charge transfer to the CeO_2 surface.

4.3.3 Smaller Model: $RuSn_3$

Whilst the discussion in the previous section appears to resolve the debate about the structure of the absorbed species, the formation of a $RuSn_9$ monolayer presents significant challenges for our computational study of the reaction mechanism for the WGS reaction. Specifically, the $RuSn_9$ monolayer, 9**D**, occupies a much larger area on the CeO_2 surface than the intact cluster (**A**), and so a larger unit cell is required to prevent interactions between the clusters in neighbouring cells. This concern is particularly pressing given the high degree of charge transfer to the surface, and the slow $\frac{1}{r}$ dependence of coulomb interactions with distance. The 3×6×1 expansion of the unit cell used for the previous calculations is tractable for the small number of calculations reported in figure 4.18, it is unlikely to be useful for a wider study of the mechanism of various catalytic reactions which demand transition state searching as well as the location of minima. We have, therefore, sought to identify smaller models that capture the key electronic features of the electronic structure of the full system. The separation of the $RuSn_3$ unit from the Sn_6 island that is common to the most stable structures, 9**D**, 3**B** and 17**E**, suggests that one possibility is to model the active site as $RuSn_3$ rather than $RuSn_9$, in which case the dimensions of the unit cell in x and y direction can be reduced. From Figure 4.21, the Sn_6 unit and the $RuSn_3$ units

are separated by Sn-Sn distances of 4.07 Å , considerably greater than those within the Sn_6 unit (3.28 Å).

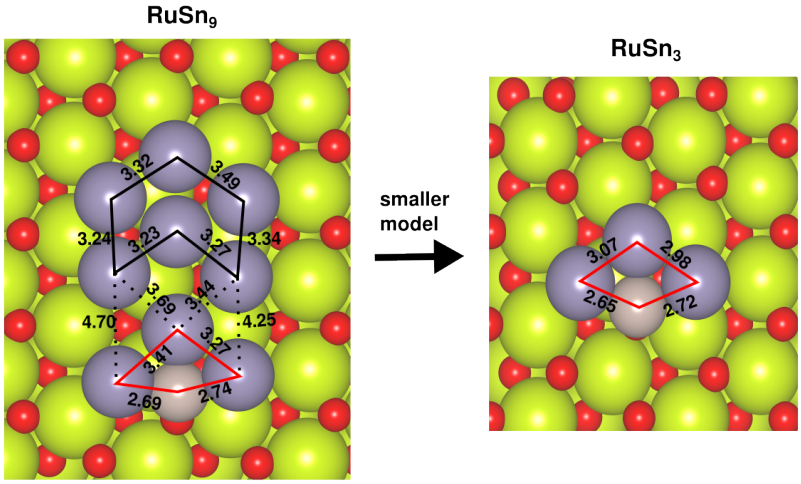

Figure 4.21: Comparing the Sn-Sn and Ru-Sn bond distances for the main model, $RuSn_9$ and the smaller model, $RuSn_3$.

We have optimised the structure of the isolated $RuSn_3$ unit in a smaller 2×4×1 expansion of the $CeO_2(111)$ surface, and find that the Ru-Sn distances are largely unchanged by the removal of the Sn_6 component (2.65-2.72 Å vs 2.69-2.74 Å in 9**D**). In contrast, the Sn-Sn distances are more strongly affected, contracting from $\sim$ 3.3 Å to $\sim$ 3.0 Å. The greater sensitivity of the Sn-Sn distances is unsurprising given that these atoms are in direct contact with the Sn_6 island that is absent in the smaller model. The projected density of states (PDOS) and spin density plot for the smaller $RuSn_3$ model is compared to that of the full $RuSn_9$ unit (in 9D) in Figure 4.16. The smaller number of Sn atoms in the model leads to a reduced transfer of charge to the surface (only 3 Ce ions are reduced), but the spin density on Ru and the localisation of the reduced Ce^{3+} ions in the region of the surface directly below the absorbed cluster are common to both the large and small models. The PDOS plots are also striking similar, both showing the majority-spin $4f$ peak below the Fermi level that is characteristic of Ce^{3+}. In light of these similarities, structural and electronic, we proceed to study the mechanism using the smaller $RuSn_3$ system as our basic model for the catalytic unit.

4.3.4 Influence of Oxygen Defects

Before moving on to the study of catalysis, we explore one further aspect of the surface absorption of the cluster on CeO_2, the possible role of defects. The presence

of oxide ion defects is an intrinsic feature of oxide surfaces, and there have been many discussions of oxygen spillover wherein oxygen can be extracted from the surface by an absorbed species, which is itself oxidised.[226,227] Yang et al. have shown that the deposition of Pt on a CeO_2 surface reduces the oxygen vacancy formation energy relative to a clean CeO_2 surface and also that the vacancy formation will occur close to the adsorbate.[260]

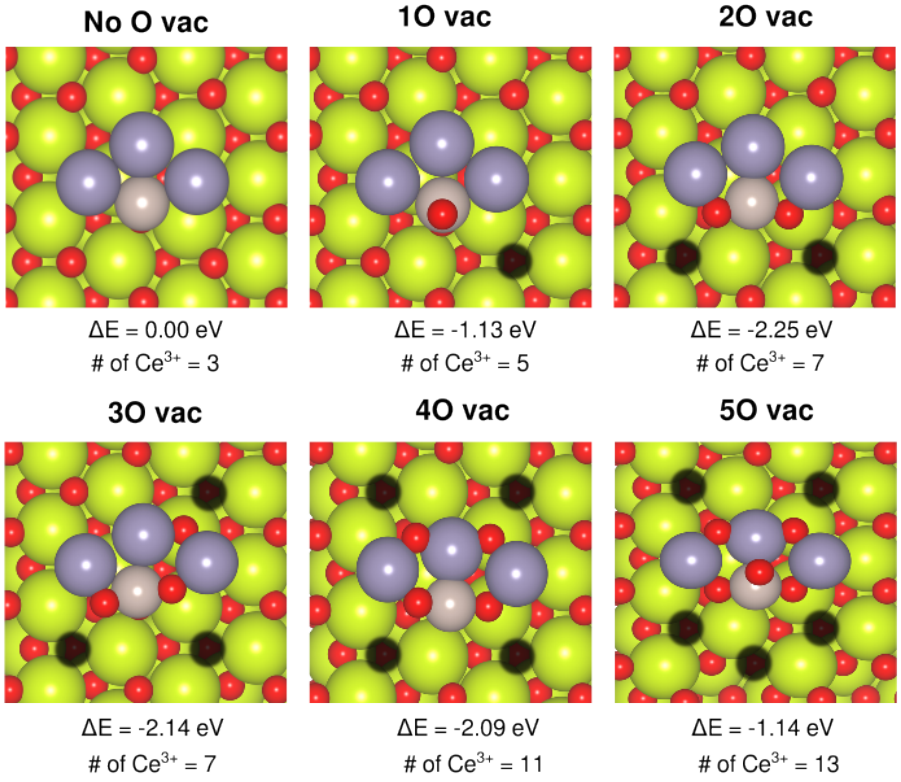

Figure 4.22: Optimised structures, relative energies and number of reduced Ce atoms of different numbers of oxygen-spillover systems where black circles are the oxygen-vacancy sites.

Using the $RuSn_3$ model identified in the previous section, we have searched for isomeric structures where one or more O atom is extracted from the surface to form Ru-O or Sn-O bonds. The extraction of a single O atom (**1O vac** in Figure 4.22) to form a terminal Ru=O unit is exothermic (ΔE = -1.13 eV), as is the extraction of a second oxygen to form two Ru-O-Sn bridges (ΔE = -2.25 eV) (**2O vac** in Figure 4.22). Models where the vacancy position is further away from the $RuSn_3$ are less stable by $\sim$ 0.2 eV. Extraction of a third or fourth oxygen to bridging Sn-O-Sn sites is marginally endothermic, while extracting a fifth oxygen to form a terminal Ru=O unit is very unfavourable. Each extraction step results in the 2-electron reduction of

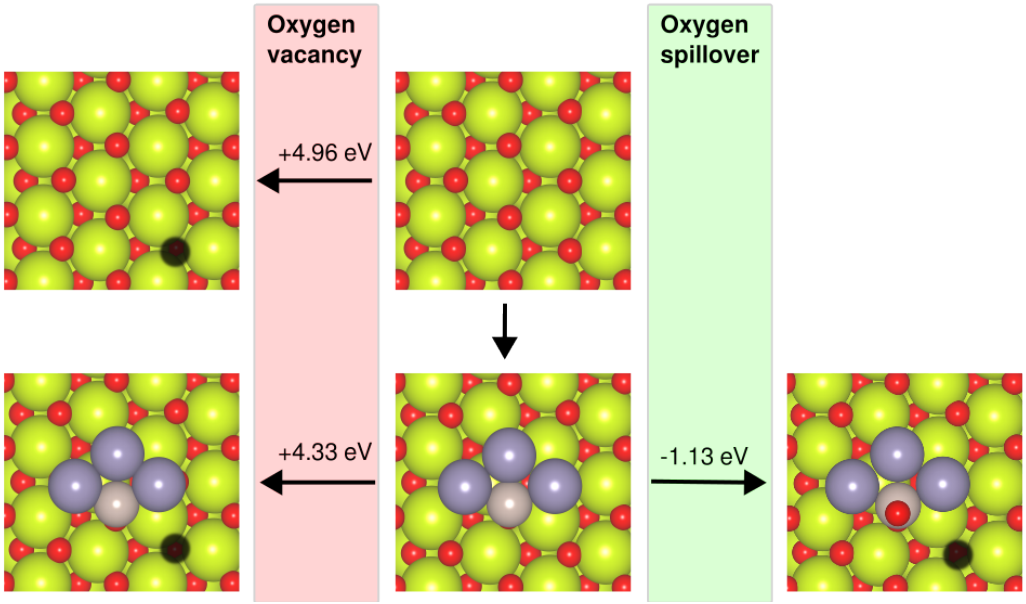

Figure 4.23: Comparison of the oxygen vacancy formation and oxygen spillover energies for both with or without adsorbate on the $CeO_2(111)$ surface. A single oxygen atom was pulled out from the surface and placed in the vacuum, subsequently the oxygen atom was adsorbed on the cluster.

the CeO_2 surface (marked by an increase of 2 in the number of reduced Ce centres) with concomitant oxidation of the $RuSn_3$ unit, to the point where the **5O vac** model has 13 reduced Ce centres, indicating a very significant charge separation between adsorbate and support.

Further insight into the thermodynamics of vacancy formation comes from the elementary processes shown in Figure 4.23. On the isolated surface, the oxygen vacancy formation energy is extremely high (+4.96 eV), consistent with the high stability of the CeO_2 lattice. In the presence of the absorbed cluster, the formation of the defect is still highly endothermic (+4.33 eV), but the formation of the Ru-O bond in **1O vac** more than compensates, leading to the oxygen spillover energy of -1.13 eV. The oxygen spillover of the system may well exert a significant impact on the catalytic efficiency of the $Ru-SnO_x/CeO_2$ system. The remaining part of this chapter involves the exploration of the mechanism using the basic $RuSn_3$ model shown in Figure 4.21 and compares the impact of oxygen spillover in the reaction mechanism.

4.4 Mechanistic Studies of the Water Gas Shift Reaction

4.4.1 Mechanism

The precise reaction mechanism of the water gas shift reaction remains a matter of some debate and depends on a number of factors including the catalyst (specifically whether it is redox-active or not) and the reaction temperature: high temperature (HT) or low temperature (LT) pathways have been proposed.[261] The two most widely accepted pathways are the redox pathway and the associative pathway, which are reviewed below.[262]

4.4.1.1 Redox Pathway

The redox mechanism is often invoked for the high-temperature WGSR (HT-WGSR), for example in the dominant industrial process involving Fe-Cr catalysis,[263–265] where the accessibility of Fe^{2+}/Fe^{3+} redox couple is a key feature. The redox pathway has also been proposed for some examples of the low-temperature WGSR.[266,267]

A schematic representation of the redox pathway is shown in Figure 4.24, and in the set of steps **A**-**I** set out below:

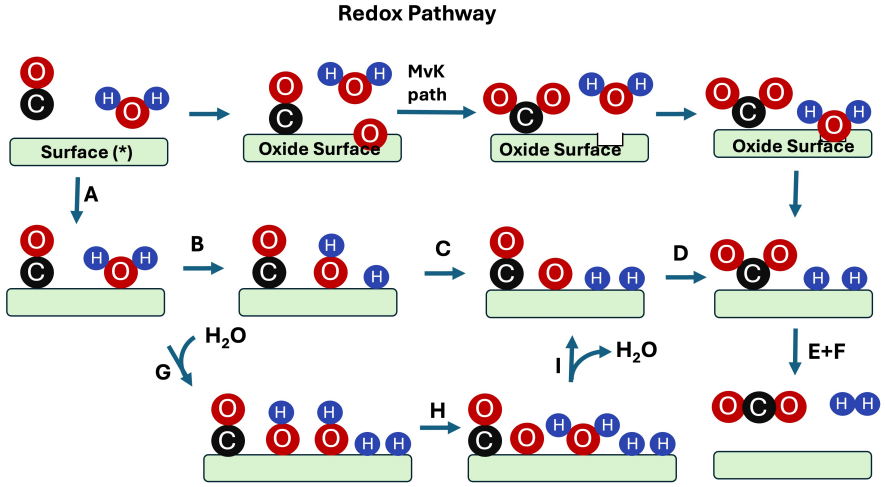

Figure 4.24: Schematic representation of redox pathways in water-gas-shift reaction.

$$CO + H_2O + * \rightarrow CO^* + H_2O^* \quad (\mathbf{A})$$

$$H_2O^* \rightarrow OH^* + H^* \quad (\mathbf{B})$$

$$OH^* \rightarrow O^* + H^* \quad (\mathbf{C})$$

$$CO^* + O^* \rightarrow {CO_2}^* \quad (\mathbf{D})$$

$$H^* + H^* \rightarrow H_2 \quad (\mathbf{E})$$

$${CO_2}^* \rightarrow CO_2 \quad (\mathbf{F})$$

$$2\,H_2O^* \rightarrow 2\,OH^* + 2\,H^* \quad (\mathbf{G})$$

$$2\,OH^* \rightarrow H_2O^* + O^* \quad (\mathbf{H})$$

$$H_2O^* \rightarrow H_2O \quad (\mathbf{I})$$

In the redox pathway, adsorption of CO and H_2O on catalyst surface sites (denoted as '*') (step A) is followed by dissociation of H_2O^* to OH^* and H^* (step B). Next, further dissociation of the O-H bond in OH^* leads to atomic oxygen (O^*) formation on the surface (step C). The active oxygen atom can then oxidise CO to CO_2 (step D). H-H bond formation between two absorbed hydrogens (H^*) is followed by desorption of H_2 and CO_2 gas (steps E and F). A variant on this scheme involves the absorption of a further molecule of H_2O followed by O-H bond cleavage to leave two OH^* groups (step G). Proton transfer and water loss then lead to the absorbed oxygen species (steps H, I).

In the sequence of steps A $\rightarrow$ F, surface bound water is the ultimate source of the oxygen atom that oxidises CO. An alternative is that the oxidation step involves one of the oxide ions of the lattice, the lattice vacancy then being back-filled by absorbed water. This mechanism, first proposed by P. Mars and D. W. van Krevelen and subsequently named the Mars-van Krevelen (MvK) pathway, is shown in the top row of Figure 4.24.[268]

4.4.1.2 Associative Pathway

The alternative associative mechanism, first proposed in the 1920s, is the dominant mechanism for low-temperature WGS, and involves a formate (HCOO) intermediate[269] Figure 4.25 shows a schematic representation of the associative pathway, and the sequence of steps, **J** - **M**, are shown below.

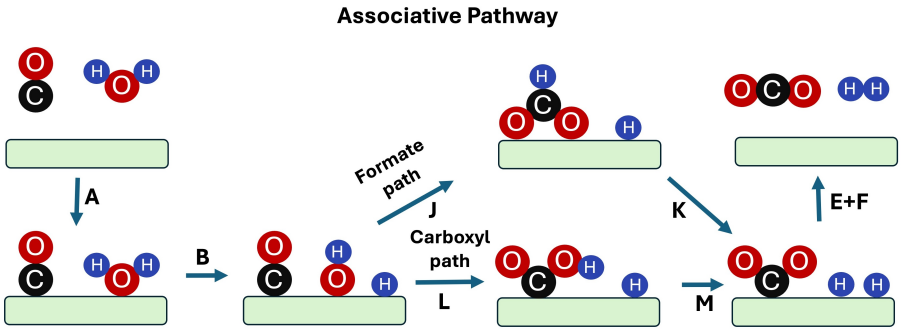

Figure 4.25: Schematic representation of associative pathways through different intermediates in the water-gas-shift reaction.

$$CO^* + OH^* \rightarrow HCOO^* \quad (\mathbf{J})$$

$$HCOO^* \rightarrow CO_2{}^* + H^* \quad (\mathbf{K})$$

$$CO^* + OH^* \rightarrow COOH^* \quad (\mathbf{L})$$

$$COOH^* \rightarrow CO_2{}^* + H^* \quad (\mathbf{M})$$

The initial steps are the same as the redox mechanism up until water dissociation (steps **A** and **B**), leading to surface-bound hydrogen and hydroxyl groups. In the so-called 'carboxyl pathway', the adsorbed OH* then transfers to the CO* (step **L**) to form a carboxyl (COOH*) intermediate. Cleavage of the O-H bond and transfer of the hydrogen to the surface (step **M**) then generates CO_2 and H_2. An alternative possibility is that the surface-bound hydrogen is transferred to the carbon of the CO*, followed by oxygen to generate a formate (HCOO*) intermediate (steps **J**, **K**, the so-called 'formate path'). Armstrong and Hilditch first proposed the formic acid decomposition mechanism to account for Cu-based catalysts.[269,270] Formate species are able to decompose spontaneously to CO and OH, but the presence of H_2O promotes the alternative decomposition to CO_2 and H_2. Gokhale et al. argued that the carboxyl (COOH) pathway is the major mechanism, with the formate species acting as a spectator.[271]

The precise identity of the active intermediate in the associative mechanism is still debated in the literature, and the balance between carboxyl and formate pathways is likely to be highly system-dependent. Computational studies appear to support the carboxyl pathway as the thermodynamically more stabilised mechanism compared to the formate path, at least on oxide surfaces.[272,273] The formation of hydroxyl ions

controls the turnover frequency for the WGSR, and so reducible surfaces (e.g. CeO_2) prove to be more effective than redox inert supports (e.g. SiO_2) and extended metal surfaces (e.g. Pt). The formate pathway, in contrast, appears to be more viable on extended metal surfaces, although it can be effectively blocked by introducing dispersed metal catalysts supported on the reducible oxide support.

Several DFT studies on supported noble metal catalysts have been devoted to predicting the most favourable mechanism for the WGS reaction. However, one of the main challenges is to correctly predict the rate-determining step (RDS) of this process and different systems have different rate-limiting steps. Rodriguez et al. reported that the cerium and titanium oxide nanoparticles supported on an Au(111) surface show excellent catalytic efficiency for WGS reaction.[222] In the reaction mechanism, CO was adsorbed on the Au surface and H_2O adsorbed on the oxide nanoparticles. The reaction goes through the carboxyl pathway and the water dissociation step $H_2O^* \rightarrow OH^* + H^*$ is the RDS. The WGS reaction on Cu-nanocluster, Cu(111) or Pd(100) catalysts appear to follow very similar pathways.[271,274,275] However, DFT and kinetic studies of the WGS reaction on a Pt(111) surface propose the $COOH^* \rightarrow CO_2{}^* + H^*$ is the rate-determining step.[273] Another study on single atom Au catalysts supported on CeO_2, TiO_2 and ZrO_2 with/without oxygen vacancy has explored different possible pathways for WGS reaction.[272] All three mechanistic paths (carboxyl, formate and redox) were compared and rate-determining steps were analysed. The carboxyl path is the lowest energy path, and the RDS in this case is H_2 formation. In contrast, O-H dissociation and -CHO formation prove to be the RDS for redox and formate path, respectively. It is clear from these studies that the identity of the rate-determining step is strongly dependent on the identity of the catalyst.

In the following section, we explore the reaction mechanism of the water-gas-shift reaction on a $RuSn_3/CeO_2$ (111) catalyst and extend our study to the oxygen spillover $RuSn_3$ catalyst, exploring how the spillover affects the reaction pathway.

4.4.2 Results and Discussion

Heterogeneous catalysis is known to be highly dependent on the reacting site of the surface and the supported nanoparticles, metalloids, or atoms. CeO_2(111) supported nanoparticles, especially those containing heavier transition metals, have been studied extensively over the past two decades. Many of these catalysts are very efficient for producing H_2 via the water gas shift (WGS) reaction, as well as the formation of methanol and methane. The outcome of these reactions is highly dependent on conditions: a 1:1 ratio of CO and H_2O typically leads to the formation of H_2 but

an increase in the pressure of H_2 increases the amount of hydrocarbon side-products, CH_4 and methanol. Our aim in this study is to establish the most effective active site for the initial step in the WGS reaction, leading to H_2 gas and CO_2.

4.4.2.1 Choice of Model Catalyst

In Figure 4.12, we showed the adsorption and stability of the $RuSn_9$ cluster on the CeO_2 surface. We observed that the cluster is not energetically stable in its 3-dimensional form, but rather is dispersed over that surface to maximise the contact area and form a monolayer of $RuSn_9$. A detailed survey of the potential energy surface has identified a smaller $RuSn_3$ fragment as a common feature in most of the stable structures, leading us to use this more tractable species as a model for the active site. The resulting reduction in computational cost is critical to the project, particularly for transition state searching. Therefore, we proceed to the mechanistic study with this smaller model, $RuSn_3$ supported by $CeO_2(111)$ as shown in Figure 4.26. We also showed in the previous section that O-spillover from the oxide surface to the nanocluster is thermodynamically favoured and in fact, the 2O-spillover at the Ru-Sn bridging site (Figure 4.22) is the most favourable structure of all those considered. We have, therefore, also considered the WGS reaction on the spillover system.

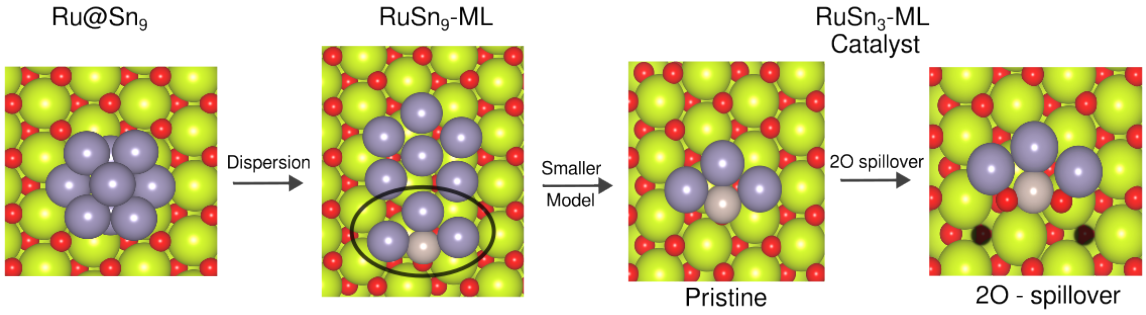

Figure 4.26: Cluster dispersion and choice of catalysts for the mechanistic study.

4.4.2.2 WGSR on a Pristine Surface

The energies and structures of key stationary points on the potential energy surface for the WGSR are summarised in Figure 4.27. The flow of charge between the surface and the adsorbate is mapped in Figure 4.28. Both associative and redox pathways have been considered. The first step of the reaction is CO adsorption on top of Ru in an end-on fashion, precisely as we would expect from known organometallic chemistry.

The CO adsorption stabilises the system significantly by -2.85 eV and the Ru-C bond distance is 1.86 Å. The C-O bond distance slightly increases to 1.176 Å from the free CO gas species (1.144 Å). A recent study on a ceria-supported Ru single-atom catalyst also shows strong CO adsorption (ΔE = -2.25 eV).[276] Absorption of CO in a tilted mode is considerably less favourable in energy, as shown by the red line in the figure. The next step is to search for favourable binding sites for H_2O. If H_2O is placed on the $RuSn_3$ unit, the calculations typically either expel the H_2O or fail to converge. In contrast, water adsorbs exothermically (-0.3 eV) on the surface Ce atom close to the cluster. Analysis of the magnetic moments on the surface Ce ions confirms that the binding of CO and H_2O has no impact on the charge transfer, there being 4 reduced Ce^{3+} ions in each case. Similar features have been noted for a CeO_2 supported Au matrix catalyst.[222] The H_2O can then dissociate exothermically to H* + OH* (step **B**) with a barrier of only 0.16 eV. We have identified two possible sites for the absorbed OH*, one close to one of the Sn atoms of the cluster (INT2, green path, CO* + HO*–Sn + H*), the other further away from it (black path, CO* + HO* + H*). The stabilisation by Sn is clearly significant as the former is more stable by 0.88 eV.

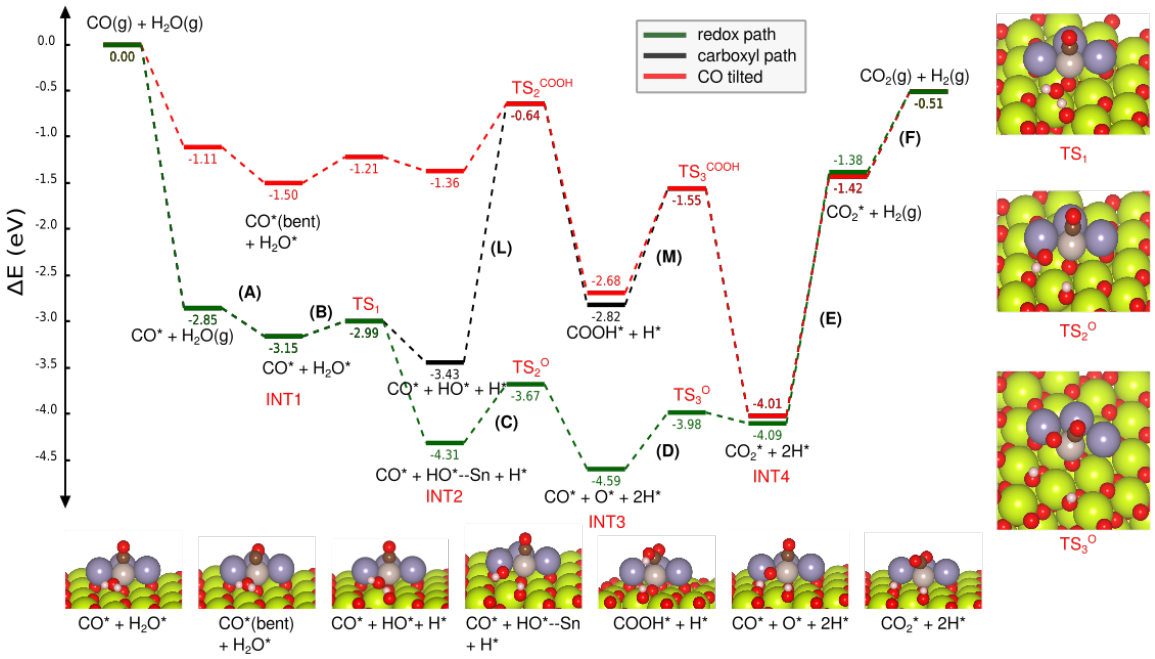

Figure 4.27: Energy profile (in eV) of the water-gas-shift reaction on a $RuSn_3/CeO_2(111)$ pristine catalyst and comparison of both redox (green) and carboxyl (black) pathways. Steps are shown in bold letter. INT = intermediate, TS = transition state; superscripts on TS indicate the path.

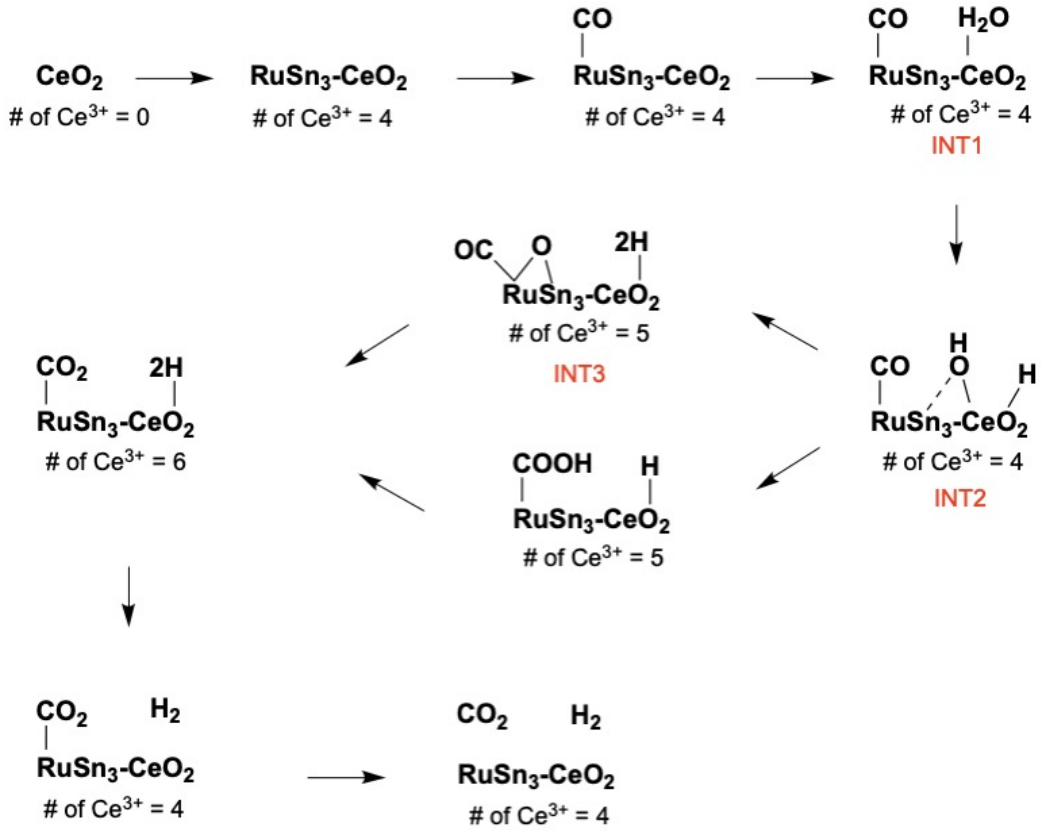

Figure 4.28: Schematic representation of the charge transfer to the surface during the WGS reaction.

From the more stable position of the OH* group (green path), the system follows a redox mechanism wherein OH* bond cleavage places a H* atom on the surface oxygen and the activated O* binds strongly at the Sn/Ru junction, forming a bridging oxide (INT3). The barrier height for OH dissociation is 0.64 eV, and the formation of the bridge ($CO^* + O^* + 2\,H^*$) is exothermic (-0.28 eV). The reduction of the surface by the H* atom causes a further increase in the number of reduced Ce^{3+} ions (to 5). The bridged Ru-O-Sn motif is precisely the same as the one noted previously in the spillover studies (Figure 4.22), suggesting that the Ru-Sn junction is a favourable locus for the oxidation of the cluster. From the bridging site, the O* (oxide) is then transferred to the adsorbed CO* with a barrier of 0.61 eV, the CO_2* being bound on top of the Ru site. The effective oxidation of the $RuSn_3$(CO) unit drives a further electron transfer to the surface (6 Ce^{3+} ions). The two H* adsorbed on the surface can then bind together and desorb as H_2 gas, withdrawing two electrons from the surface and completing the cycle. In reference to the schemes for the mechanism discussed previously, the role of the $RuSn_3$ appears to be to stabilise the surface oxygen species (formed in step **C** of the redox pathway) by forming a stable Ru-O-Sn bridge (INT3). From the alternative OH* intermediate (black line at -3.43 eV), we can also identify a carboxyl-like associative pathway where the OH* migrates directly to the CO* absorbed on Ru forming COOH* intermediate, followed by proton transfer and CO_2 desorption. This pathway merges with the red 'CO bent' pathway because the surface-Ru-CO angle is naturally bent when the OH* binds to it. It is clear, however, that this associative pathway is far less favourable, and that the more reactive O* species in INT3 is required to disrupt the strong Ru-C and C=O bonding in the bound carbonyl.

The largest barrier, 0.64 eV, (not considering the adsorption and desorption steps) on the redox pathway (green line) is that between INT2 and INT3, labelled TS_2^O in Figure 4.27, corresponding to the cleavage of the second OH bond. This value is considerably lower than the value of 1.34 eV reported for a Co/MoS_2 catalyst.[263] The most stable point on the surface corresponds to the oxide intermediate (INT3), which is 0.28 eV below the preceding hydroxide (INT2), and 0.5 eV below the CO_2 intermediate, INT4. The relatively low barrier for O-H bond cleavage is related to the stability of the oxide, which in turn is a consequence of the oxophilicity of the Ru-Sn junction. The alternative carboxyl pathway passes through the structure identified as 'COOH* + H*' in Figure 4.27, which lies 1.77 eV higher than INT3. On that basis, we believe that the redox pathway is preferred in this case, due to the relative stability of the Ru-O-Sn junction.

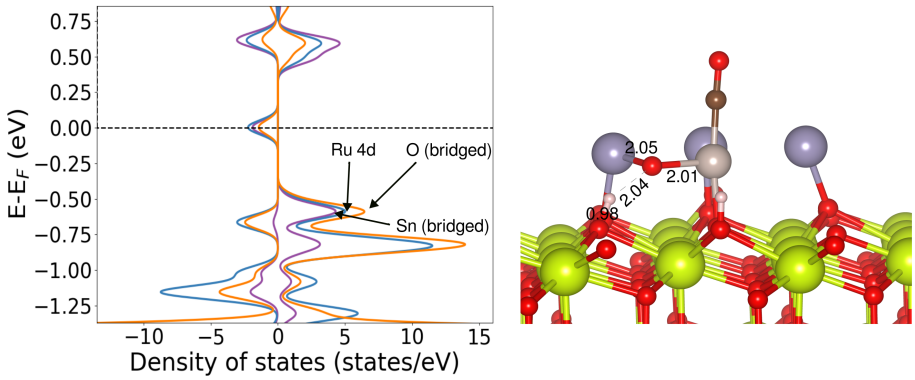

Figure 4.29: Projected DOS and optimised structure of the oxide intermediate.

The very high stability of the Ru-O-Sn intermediate has prompted us to look in more detail at its electronic structure. The synergic effect of the Ru-Sn bridging site reduces the barrier to O-H dissociation and stabilises the O atom at the bridging position. The structural features of the oxide intermediate are shown in detail in Figure 4.29. The distance between Sn and the atomic oxygen is 2.05 Å, shorter than the Sn and surface oxygen bond distance (2.09 Å), and the Ru-O (atomic) distance is the same with the Ru-O (surface) bond distance (2.01 Å). This is clear evidence of strong Ru and Sn bonding interaction with the atomic oxygen, stabilising the key oxide intermediate. The projected density of states (PDOS) plot of the atomic O, Ru confirms the strong hybridisation of the Ru/Sn/O states. The potential energy surface in (Figure 4.27) shows that the formation of the oxide intermediate O* from OH* (step **C**) is the highest barrier for the redox pathway while H* transfer from carboxyl (COOH*) to the surface (step **M**) is the RDS for the associative pathway, with barriers of 0.64 eV and 1.13 eV, respectively.

The surface reaction is happening significantly lower energy level compared to the gas phase WGS reaction as shown in Figure 4.27. The adsorption energy of supplied gases and desorption of produced gases are quite high. In this reaction medium, continuous supplies of CO(g) and water vapour drive the reaction to the desired products.

4.4.2.3 WGSR following Oxygen Spillover

We have also investigated the reaction mechanism of WGS reaction on the catalyst formed by oxygen spillover from the CeO_2 surface to the cluster (Figure 4.26). The total energy of the 2O-spillover catalyst is -2.25 eV lower than the pristine system (Figure 4.22) and, as a result, all intermediates on the pathway are also lower. In

order to facilitate the comparison of the important steps, we set the energy of the isolated catalyst (pristine or 2O-spillover) to zero. In Figure 4.30 we plot the relative potential energy surfaces for key intermediates (without transition states) of the WGS reaction for the 2O-spillover catalyst (blue and pink) and the pristine catalyst (black and green).

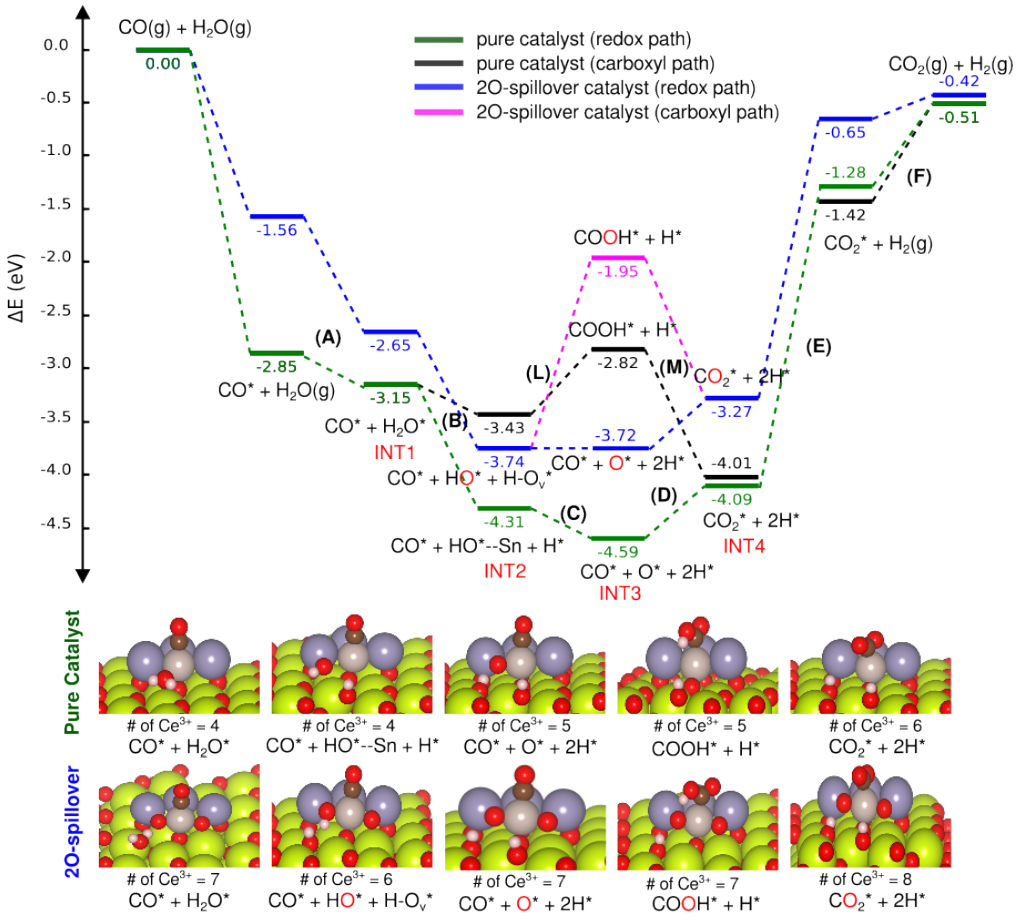

Figure 4.30: Energy profile of WGS reaction on an oxygen spillover $2\,O-RuSn_3/CeO_{2-y}$ catalyst compared to the pristine $RuSn_3/CeO_2$ catalyst. The red colour oxygen (O) in intermediates (INT) indicates the bridging oxygen and O_v indicates the water oxygen which fills the surface vacancy.

In the pristine catalyst, the key steps (i) binding of CO and H_2O (step A), (ii) cleavage of O-H bonds, with H^* migrating to oxides on the CeO_2 surface and (iii) migration of the oxide to the Ru-Sn junction (steps B and C) and, from there, to the bound CO (step D). In the case of the 2O-spillover catalysts, the mechanism is subtly different because the Ru-Sn bridging sites are already occupied by oxide ions, leaving no space for a further oxide to migrate into these positions. The initial step, CO absorption onto Ru, is very similar to that in the pristine catalyst, but the adsorption

energy is significantly less negative, -1.56 eV compared to -2.85 eV. The presence of oxygen in the Ru-Sn bridging sites results in the oxidation of the $RuSn_3$ cluster compared to the pristine catalyst (as measured by the greater number of Ce^{3+} ions in the surface), and this, in turn, reduces the amount of electron density at Ru available to back-donate to the bound CO. The binding of H_2O is, however, quite different in that it fills one of the vacant sites on the CeO_2 surface, rather than binding on top of the Ce on the surface. O-H bond cleavage then occurs in step B, and we have identified two intermediates with very similar energies (labelled INT2 and INT3 in Figure 4.30). In INT2, the hydrogen is bound to the oxide in the Ru-Sn bridging position, while in INT3 it is bound to one of the surface oxides, leaving the Ru-O-Sn bridge unprotonated. From this point, migration of one of the Ru-O-Sn bridging oxides to the bound CO^* occurs to form $CO_2{}^*$, a step that is endothermic by 0.55 eV compared to 0.50 eV in the pristine catalyst. The very similar thermodynamics for the O-transfer step in the pristine and 2O-spillover catalysts reflect the fact that the structure of the (CO)Ru-O-Sn unit is largely unchanged in the two mechanisms: the bound H_2O has filled one of the vacancies on the surface and placed two addition hydrogen on the surface oxides, but this does not influence the bound cluster, at least to a first approximation. We note that during the process of O^* transfer to the bound CO^* in 2O-spillover catalyst, a successive oxygen spillover to the bridging site occurs and keeps the catalyst same. We therefore conclude that the key step in the reaction, the migration of O^* to bound CO, is not strongly influenced by the presence or otherwise of surface defects.

4.5 CO Methanation: A side Reaction of WGSR

In the experimental study of the WGS reaction by Sun and co-workers, significant amounts of hydrocarbons were also observed. This has prompted us to explore an alternative pathway, leading to methane.

4.5.1 Introduction

All of the reactions described in the previous section are reversible, and so the precursor, CO can be reduced to CH_4 or other hydrocarbons by the generated H_2 unless it is removed from the reaction vessel. Therefore, we have extended our study to CO reduction by produced hydrogen gas in WGSR. Methanation is a general term

to describe the conversion of carbon oxide (CO_x) to methane (CH_4) through hydrogenation. It is an important step used to remove traces of CO (remaining after the water–gas shift reaction) during hydrogen production in commercial methane steam reformers.[277] Research into CO_x conversion into synthetic fuels and chemicals is one of the most active research areas in the search for clean and sustainable energy systems.[278–280] The methanation reaction is not only important for the catalytic conversion of CO into valuable products but also plays a significant role in hydrogen-based energy systems. Burning of coal, fossil fuels, or wood emits dangerous greenhouse gases (CO_x) and conversion of these to methane or substitute natural gas (SNG) offers a promising avenue to both reduce emissions and replace fossil-derived fuels. Methanation reaction of CO and CO_2 can be described as follows:

$$CO + 3H_2 \rightarrow CH_4 + H_2O \qquad \Delta H = -206\ kJ/mol$$
$$CO_2 + 4H_2 \rightarrow CH_4 + 2H_2O \qquad \Delta H = -164\ kJ/mol$$

The process is highly exothermic and is carried out in the presence of a catalyst to accelerate the reaction and also to increase the selectivity of the product. Otherwise, the hydrogenation of the gases can lead to the forming of different hydrocarbons. Two main routes of the methanation reaction are classical carbon monoxide (CO) methanation, which uses CO as a feedstock, and the other one is carbon dioxide (CO_2) methanation. We will be mainly focusing on the CO methanation reaction as the starting precursor is CO, which we have used in water-gas-shift reactions as well.

Catalysts are crucial for the methanation process, not only for the reaction acceleration and selectivity but also for up- and downstream processes. This process was first discovered by Sabatier and Senderens in 1902, where nickel was used as a catalyst.[281] In the subsequent 120 years, many noble and transition metal catalysts have been discovered that are capable of accelerating the methanation reaction.[278] The highly exothermic nature of the process means that coke formation and sintering limit catalyst lifetime, and there has been a continuous search for improved performance. For example, Fischer et al. studied a range of unsupported metal catalysts such as Ru, Rh, Ir, Ni, Pt, Pd, Fe, Ag etc. under methanation reaction conditions, noting that Ru has extremely high activity.[282] However, another study by Vannice reported that though the reactivity of Ru is very high, the noble metals (Pt, Pd) have higher selectivity.[283] Ni is also a highly selective catalyst with moderate reactivity and is much cheaper than any of Ru, Pd or Pt.[284] It therefore remains the most commonly applied active metal for commercial methanation applications. Fe

catalysts are known for high reactivity, but low selectivity towards methanation reaction.[285] Whilst the identity of the metal influences the methanation reaction, the support, promoter and preparation conditions can also be important in determining the activity and selectivity of the reaction. A large surface area can be obtained by supporting a small particle of active metals on the large surface support, and oxide supports such as Al_2O_3, SiO_2, TiO_2 are often used to create large surface areas and, in the latter case, flexible oxidation states. Al_2O_3 is mostly commonly used as support, often with promoters such as MgO which increase the thermal stability and catalytic activity of Ni catalysts. However, CeO_2 has recently found extensive use.[278,284]

Two types of CO methanation mechanisms have been proposed in the literature. Figure 4.31 shows a schematic pathway of the reaction. The first 'associative' pathway involves the transfer of adsorbed H* to the CO*. The second 'dissociative' pathway involves CO* bond cleavage followed by hydrogenation.

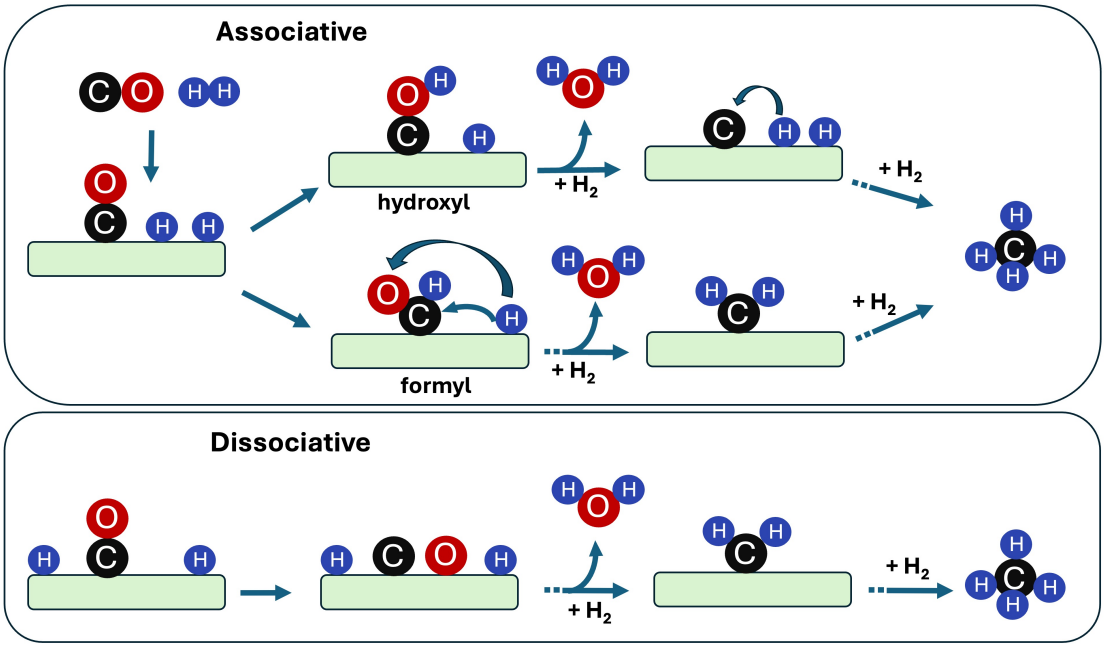

Figure 4.31: A schematic draw of both associative and dissociative mechanistic path of CO methanation reaction.

Previous studies have shown that the direct C-O bond breaking is not kinetically favourable, but H* can assist the process.[286,287] In an associative pathway, carbonyl (CO*) can be reduced by the H* and two intermediates are possible: (i) H bonds to C to generate a formyl intermediate CHO* and (ii) H* binds to the O of the carbonyl to form a hydroxyl (COH*) intermediate. Successive reduction of these two intermediates will lead to the C-O bond dissociation and release of H_2O(g) and

CH_4(g). In the case of the dissociative pathway, the C-O bond of the adsorbed CO* will dissociate first and produce atomic C* and O* intermediates. Consecutive reduction of both C* and O* will be released as CH_4(g) and H_2O(g) from the catalytic surface.

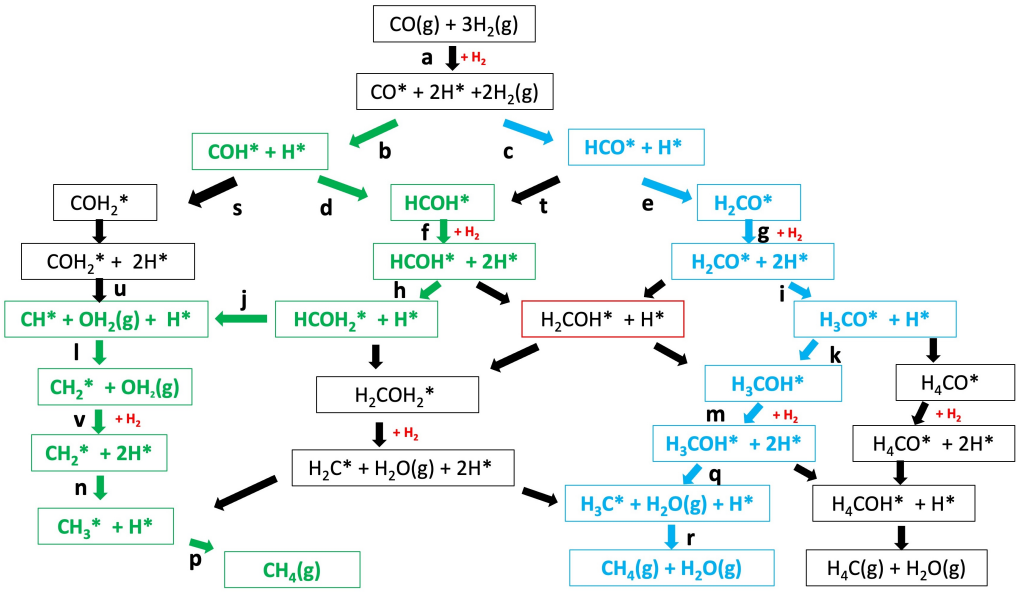

Figure 4.32: A schematic view of all possible intermediates for the associative pathway in CO methanation reaction. Blue and green colour paths are the commonly followed reaction path and these intermediates are used in the mechanistic study.

There are many possible pathways leading to the final products, differing in the order of C/O-H bond formation and C-O bond cleavage - a schematic diagram of all possible intermediates for the associative path is shown in Figure 4.32. The blue path (formyl) and green path (hydroxyl) in the figure have been considered to connect the intermediate steps for mechanistic study.

In this section, we have tried to understand the reaction pathway of CO methanation reaction on a pristine $RuSn_3/CeO_2$ catalysts. We have selected specifically pathways that differ in the order of formation of C-H and O-H bonds.

4.5.2 Results and Discussion

The energies and structures of the key stationary points of the potential energy surface for the associative pathway of the CO methanation reaction on a pristine $RuSn_3/CeO_2(111)$ catalyst are summarised in Figure 4.33. The blue pathway corresponds to the sequence of reactions shown in blue in Figure 4.32 while the green

pathway corresponds to the green steps in the same figure. We note that the H_2 adsorption steps (**a**, **f**, **g**, **m** and **v** in Figure 4.32) are not added in the potential energy plot (Figure 4.33). The initial steps involve binding of CO, precisely as we have de-

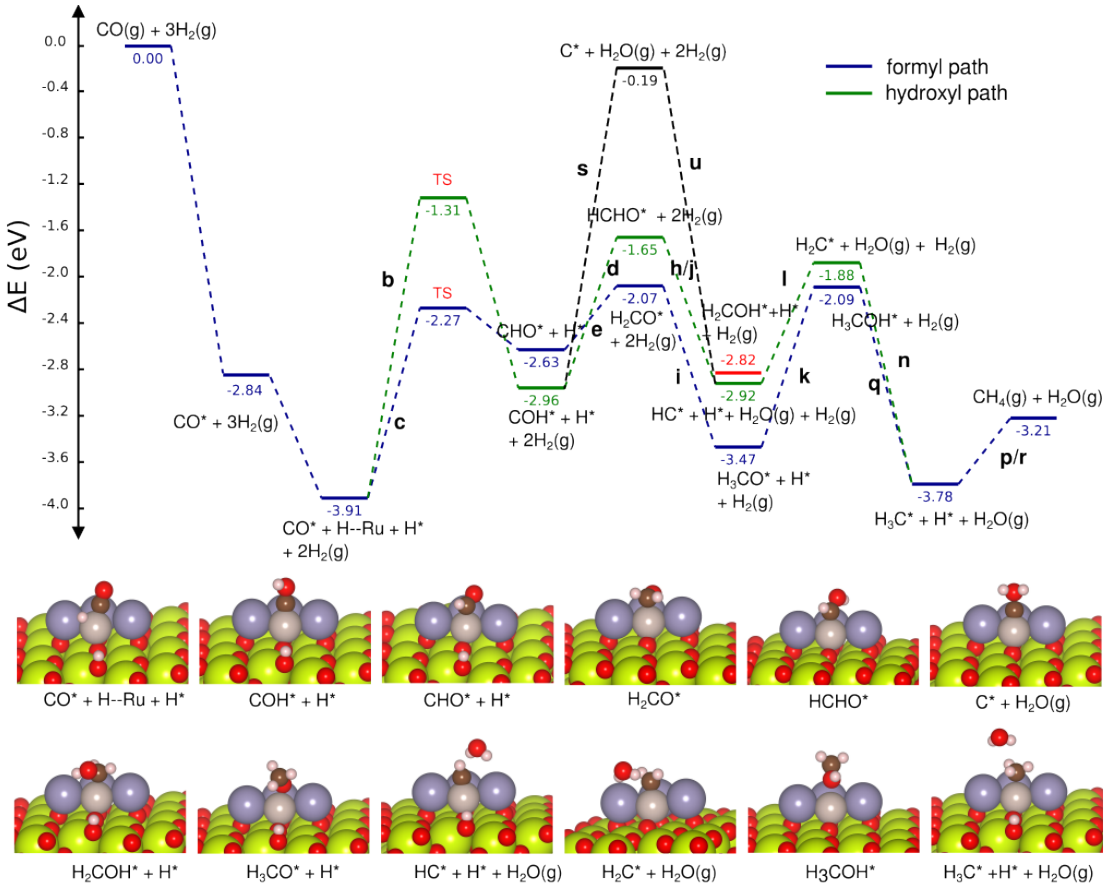

Figure 4.33: Energy profile of CO methanation reaction via associative mechanism; dark blue path indicates the reaction goes through formate (CHO*) intermediate and the green path indicates hydroxyl (COH*) pathway.

scribed in the previous section. The CO binds end-on on the Ru atom, with a binding energy of -2.84 eV. A molecule of H_2 can then bind to the surface with a binding energy of -2.56 eV, forming two surface O-H groups. The adsorption energy of hydrogen after dissociation for a clean $CeO_2(111)$ surface is reported as $\sim$ -2.16 eV.[288,289] From there, one hydrogen can migrate from the surface O-H to the Ru centre (ΔE = 1.5 eV). From that point, there are two possibilities for the migration of the hydrogen to the bound CO. In the first (blue line in Figure 4.33) the hydrogen migrates to the carbon, generating a formyl intermediate, CHO*. The alternative is to migrate to the O terminus of the ligand, which is thermodynamically more favoured by -0.33 eV, but kinetically disfavoured, with a transition state energy difference of +0.96 eV,

compared to the formyl intermediate. The second hydrogen can then migrate, again either to carbon or oxygen, giving three possible products denoted HCHO*, H_2CO* and C* + H_2O. Of these, the latter, where the C-O bond is cleaved, is much less stable than the alternatives where the C-O bond remains intact. From here, binding of a second molecule of H_2 leads to two surface O−H groups one of which can migrate to C to form H_3CO* or H_2COH*, or to O to form CH* + H_2O. Migration of the second hydrogen then yields either methanol, CH_3OH*, which is only very weakly bound to the surface, or H_2C* + H_2O, the two products having rather similar energies. It is likely that the CH_3OH then desorbs from the surface, and is the source of methanol observed in the reactions, while the CH_2* is reduced by a further molecule of absorbed H_2 to generate CH_4. The favoured pathway is a balance of thermodynamic and kinetic factors. Thermodynamically, the most stable intermediate for the first hydrogen transfer is COH*, with hydrogen bound to the oxygen, but this is accessible only via a high-energy transition state. Alternatively, the CHO* intermediate is less stable but is accessed via a much lower energy transition state. The preference for the formyl pathway is typical for a range of methanation catalysts that have been reported in the literature.[290,291]

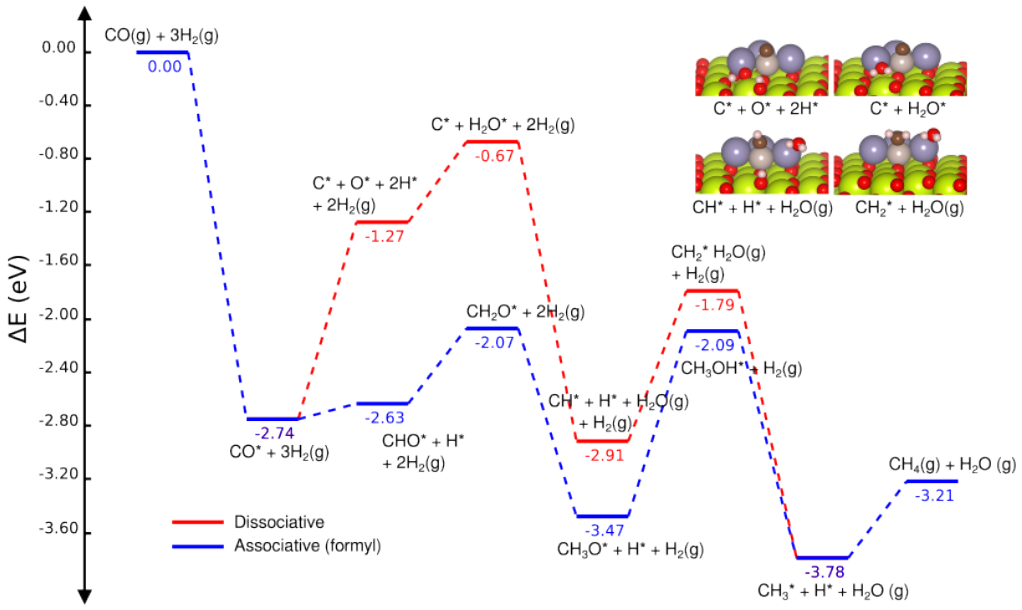

Figure 4.34: Energy profile comparison between the favourable associative path (via formate intermediate) and the dissociative path for CO methanation reaction.

Finally, we have compared the formyl path against the dissociative pathway for the methanation reaction. The energies and structures of the stationary points of the potential energy surface of the dissociative pathway are summarised in Figure

4.34 where they are also compared against the lowest energy associative path (formyl path). In the dissociative path, the key intermediate after CO bond dissociation is C* + O*, which is very high in energy, 1.36 eV less stable than the CHO* intermediate. Successive reduction of dissociated O* leads to H_2O(g) while reduction of C* generates CH_4(g). The overall path of the dissociative mechanism (red path) is, however, sufficiently high compared to the formyl path to be ruled out as a viable mechanism in this case.

4.6 Summary and Conclusions

In this chapter, I have explored the adsorption of a Zintl cluster on a CeO_2(111) surface and its catalytic activity. The isolated $[Ru@Sn_9]^{6-}$ Zintl cluster has D_{3h} symmetry and a tri-capped trigonal prismatic geometry, but the 3-dimensional structure is highly unstable when absorbed on the surface. Indeed, the thermodynamically favoured geometry is a monolayer where all the atoms (1 Ru and 9 Sn) bind with surface oxygen, leading to oxidation of the cluster and reduction of the CeO_2 surface, indicated by the presence of Ce^{3+} ions. The absorption is a balance between formation of Sn/Ru-O bonds (favouring the monolayer) vs Sn-Sn cohesive interaction (favouring a 3-dimensional structure), and the former clearly dominates. After careful consideration of several model systems, we conclude that the Ru atom is coordinated by three Sn atoms in the most stable structures. Model 9**D** (Figure 4.12) is the lowest energy. Model 9**D** shows a clear separation between a $RuSn_3$ unit and the remaining Sn_6 unit (Figure 4.21), which suggests that a smaller $RuSn_3$ model might capture all the important features of the full model ($RuSn_9$), while significantly reducing the cell size and computational cost of the subsequent survey of the catalytic pathway. Our initial studies were focused on a pristine CeO_2 surface, but we then considered the possibility that oxide ions might 'spillover' from the surface onto the $RuSn_3$ cluster of our minimal model. In fact, it proves thermodynamically favourable to extract two oxide ions from the surface, which then occupy bridging sites between the Ru and Sn atoms, with concomitant reduction of the CeO_2 surface.

A detailed mechanistic study of the WGS reaction was then performed using both the pristine surface catalysts and also the 'spillover' catalysts with the oxides in the bridging sites. The mechanism is rather similar in the two cases, with the key intermediate being the oxide in the Ru-Sn bridging position noted above. Migration from here to the ruthenium-bound CO generates CO_2 in a 'redox' pathway. The alternative carboxyl path, commonly found in low-temperature catalysts, has a considerably

higher energy. The role of the RuSn cluster appears, therefore, to be to stabilise the activated oxygen, O*, that is the key intermediate in the redox pathway. We have also reported a preliminary study of the competing methanation reaction, where the formation of formyl intermediate is kinetically favoured and follows the lower energy path over the alternative hydroxyl path.

Chapter 5

Summary and Future Work

The work of this thesis falls into two distinct chapters. The first is a fundamental study of electronic structure and metal-metal bonding in Sn-based Zintl clusters that contain transition metals (Chapter 3). The second is focussed on the catalytic applications of these clusters, specifically on the adsorption behaviour and catalytic activity of the $[Ru@Sn_9]^{6-}$ cluster on a supported oxide surface (Chapter 4), motivated by the experimental work of Sun and co-workers. Density function theory (DFT) methods have been utilised throughout the thesis for all the calculations to locate minima and transition states on the potential energy surfaces. Throughout, we have used molecular orbital diagrams and density of states as qualitative tools to interrogate the electronic structure.

The key to understanding these systems is the role of transition metal and how interactions with the cage influence the shape and electronic properties. We have mainly focused on Sn-based clusters where different transition metal(s) are incorporated. The availability of metal *d*-electrons determines the strength of the metal-cage and metal-metal bonding. On the right side of the *d* block elements typically contain closed-shell d^{10} configurations, and have relatively little effect in the cage. However, moving further left on the periodic table, the energy of the *d* orbitals increases and metal-cage interactions become more prominent via metal-to-cage charge transfer. In $[Ru@Sn_{12}]^{4-}$, weak back-bonding causes slight distortion from the ideal icosahedron that is adopted by ${Sn_{12}}^{2-}$ or $[Ni@Sn_{12}]^{2-}$. The back-bonding is much more prominent in the M_2E_{12} family, and indeed in $[Cr_2Sb_{12}]^{3-}$, we see that it is strong enough to cleave some of the Sb-Sb bonds, causing a distortion to C_{4v} symmetry. The nature of the M-M bonding is quite ambiguous in the 7-vertex metal Sn clusters, $[(CO)_3MSn_5M(CO)_3]^{4-}$ (M = Cr, Mo), but our analysis suggests that the Sn_5 unit is best considered to be in a 4- oxidation state, leaving the $M(CO)_3$ units neutral: the Cr-Cr and Mo-Mo bonds are therefore weak despite the short M-M distances.

The endohedral Zintl cluster $[Ru@Sn_9]^{6-}$ shows great promises as a catalyst when supported on a CeO_2 surface. The noble/transition metal plays the pivotal role as the main active site but the *p*-block element also has an important part to play in stabilising key intermediates in bridging sites. The strong metal-support interaction (SMSI) destroys the nearly spherical $[Ru@Sn_9]^{6-}$ cluster and disperses it as a monolayer where all the atoms make contact with the $CeO_2(111)$ surface. A systematic search of possible geometries for the dispersed cluster indicates that the most stable configuration of the monolayer has the Ru atom surrounded by three Sn atoms. The Ru-Sn junction opens up new catalytic pathways for water-gas-shift (WGS) and CO methanation reactions by stabilising the intermediate at this site. In this context, it seems that the composition of the cluster (i.e. the fact that it contains both Ru and Sn) is more important than its structure, which does not survive the process of chemisorption.

The understanding of the relationship between local atomic environments and the reactivity of clusters is important for gaining a deeper understanding of catalysis and building predictive models for faster and more efficient discovery of catalysts. Our current theoretical models are solely based on stationary points on the potential energy surface identified by DFT, and future work will involve microkinetic modelling of product distributions using kinetic Monte Carlo (KMC) simulations. High-throughput screening of compounds to search for desirable properties, as well as data-driven approaches such as machine learning to inform the design of catalysts for a targeted chemical reaction, are also emerging fields of research that will be important as the field of computational catalysis evolves.

References

[1] S. Mondal, W.-X. Chen, Z.-M. Sun and J. E. McGrady, *Inorganics*, 2022, **10**, 75.

[2] Y.-N. Yang, Z.-S. Li, S. Mondal, L. Qiao, C.-C. Wang, W.-J. Tian, Z.-M. Sun and J. E. McGrady, *Chinese Chemical Letters*, 2024, **35**, 109048.

[3] Y. Wang, C. Zhang, X. Wang, J. Guo, Z.-M. Sun and H. Zhang, *ACS Catalysis*, 2020, **10**, 7808–7819.

[4] E. Zintl, J. Goubeau and W. Dullenkopf, *Zeitschrift für Physikalische Chemie A*, 1931, **154**, 1–46.

[5] L. Diehl, K. Khodadadeh, D. Kummer and J. Strähle, *Chemische Berichte*, 1976, **109**, 3404–3418.

[6] M. Haeser, U. Schneider and R. Ahlrichs, *Journal of the American Chemical Society*, 1992, **114**, 9551–9559.

[7] B. Wang, M. Stott and J. Alonso, *Physical Review B*, 2002, **65**, 045410.

[8] L. Xu and S. C. Sevov, *Inorganic Chemistry*, 2000, **39**, 5383–5389.

[9] C. Liu, N. V. Tkachenko, I. A. Popov, N. Fedik, X. Min, C.-Q. Xu, J. Li, J. E. McGrady, A. I. Boldyrev and Z.-M. Sun, *Angewandte Chemie International Edition*, 2019, **58**, 8367–8371.

[10] C. B. Benda, T. Henneberger, W. Klein and T. F. Fässler, *Zeitschrift für anorganische und allgemeine Chemie*, 2017, **643**, 146–148.

[11] D. Dai and K. Balasubramanian, *The Journal of Chemical Physics*, 1992, **96**, 8345–8353.

[12] S. Joseph, C. Suchentrunk and N. Korber, *Zeitschrift für Naturforschung B*, 2010, **65**, 1059–1065.

[13] C. Suchentrunk and N. Korber, *New Journal of Chemistry*, 2006, **30**, 1737–1739.

[14] J. M. Goicoechea and S. C. Sevov, *Inorganic Chemistry*, 2005, **44**, 2654–2658.

[15] J. Åkerstedt, S. Ponou, L. Kloo and S. Lidin, *European Journal of Inorganic Chemistry*, 2011, **2011**, 3999–4005.

[16] C. H. E. Belin, J. D. Corbett and A. Cisar, *Journal of the American Chemical Society*, 1977, **99**, 7163–7169.

[17] M. M. Gillett-Kunnath, J. I. Paik, S. M. Jensen, J. D. Taylor and S. C. Sevov, *Inorganic Chemistry*, 2011, **50**, 11695–11701.

[18] A. Spiekermann, S. D. Hoffmann and T. F. Fässler, *Angewandte Chemie International Edition*, 2006, **45**, 3459–3462.

[19] T. B. Tai and M. T. Nguyen, *Journal of chemical Theory and computation*, 2011, **7**, 1119–1130.

[20] C. Schrenk, F. Winter, R. Pöttgen and A. Schnepf, *Chemistry–A European Journal*, 2015, **21**, 2992–2997.

[21] L.-F. Cui, X. Huang, L.-M. Wang, D. Y. Zubarev, A. I. Boldyrev, J. Li and L.-S. Wang, *Journal of the American Chemical Society*, 2006, **128**, 8390–8391.

[22] L.-F. Cui, X. Huang, L.-M. Wang, J. Li and L.-S. Wang, *The Journal of Physical Chemistry A*, 2006, **110**, 10169–10172.

[23] R. B. King, I. Silaghi-Dumitrescu and M. M. Uţă, *Dalton Transactions*, 2007, 364–372.

[24] K. Wade, *Journal of the Chemical Society D*, 1971, 792–793.

[25] D. M. P. Mingos, *Chemical Communications*, 1983, 706–708.

[26] D. P. Mingos and D. G. Evans, *Journal of Organometallic Chemistry*, 1983, **251**, c13–c16.

[27] D. M. P. Mingos, *Accounts of Chemical Research*, 1984, **17**, 311–319.

[28] A. Stock, *The Journal of Physical Chemistry*, 1934, **38**, 714–715.

[29] H. C. Brown, G. W. Kramer, A. B. Levy and M. Midland, 1975.

[30] H. Schlesinger and A. B. Burg, *Chemical Reviews*, 1942, **31**, 1–41.

[31] E. D. Jemmis, M. M. Balakrishnarajan and P. D. Pancharatna, *Journal of the American Chemical Society*, 2001, **123**, 4313–4323.

[32] E. D. Jemmis, M. M. Balakrishnarajan and P. D. Pancharatna, *Chemical Reviews*, 2002, **102**, 93–144.

[33] E. Hückel, *Zeitschrift für Physik*, 1931, **70**, 204–286.

[34] E. Hückel, *Journal of Electrochemistry and Applied Physical Chemistry*, 1937, **43**, 752–788.

[35] M. L. McKee, *Journal of the American Chemical Society*, 1988, **110**, 5317–5321.

[36] M. McPartlin, C. R. Eady, B. F. Johnson and J. Lewis, *Chemical Communications*, 1976, 883–885.

[37] S. Scharfe, T. Fässler, S. Stegmaier, S. Hoffmann and K. Ruhland, *Chemistry–A European Journal*, 2008, **14**, 4479–4483.

[38] B. J. L. Witzel, W. Klein, J. V. Dums, M. Boyko and T. F. Fässler, *Angewandte Chemie International Edition*, 2019, **58**, 12908–12913.

[39] B. Kesanli, J. Fettinger, D. R. Gardner and B. Eichhorn, *Journal of the American Chemical Society*, 2002, **124**, 4779–4786.

[40] N. Korber, *Angewandte Chemie International Edition*, 2009, **48**, 3216–3217.

[41] J.-Q. Wang, S. Stegmaier and T. Fässler, *Angewandte Chemie International Edition*, 2009, **48**, 1998–2002.

[42] B. Zhou, M. S. Denning, D. L. Kays and J. M. Goicoechea, *Journal of the American Chemical Society*, 2009, **131**, 2802–2803.

[43] T. Krämer, J. C. A. Duckworth, M. D. Ingram, B. Zhou, J. E. McGrady and J. M. Goicoechea, *Dalton Transactions*, 2013, **42**, 12120–12129.

[44] E. N. Esenturk, J. Fettinger and B. Eichhorn, *Chemical Communications*, 2005, 247–249.

[45] E. N. Esenturk, J. Fettinger and B. Eichhorn, *Journal of the American Chemical Society*, 2006, **128**, 9178–9186.

[46] L.-F. Cui, X. Huang, L.-M. Wang, J. Li and L.-S. Wang, *Angewandte Chemie International Edition*, 2007, **46**, 742–745.

[47] J.-Q. Wang, S. Stegmaier, B. Wahl and T. Fässler, *Chemistry–A European Journal*, 2010, **16**, 1793–1798.

[48] C. Liu, X. Jin, L.-J. Li, J. Xu, J. E. McGrady and Z.-M. Sun, *Chemical Science*, 2019, **10**, 4394–4401.

[49] E. N. Esenturk, J. Fettinger, Y.-F. Lam and B. Eichhorn, *Angewandte Chemie*, 2004, **116**, 2184–2186.

[50] B. Zhou, T. Krämer, A. L. Thompson, J. E. McGrady and J. M. Goicoechea, *Inorganic Chemistry*, 2011, **50**, 8028–8037.

[51] C. Liu, L.-J. Li, I. A. Popov, R. J. Wilson, C.-Q. Xu, J. Li, A. I. Boldyrev and Z.-M. Sun, *Chinese Journal of Structural Chemistry*, 2018, **36**, 1165–1168.

[52] L.-J. Li, F.-X. Pan, F.-Y. Li, Z.-F. Chen and Z.-M. Sun, *Inorganic Chemistry Frontiers*, 2017, **4**, 1393–1396.

[53] G. Espinoza-Quintero, J. C. A. Duckworth, W. K. Myers, J. E. McGrady and J. M. Goicoechea, *Journal of the American Chemical Society*, 2014, **136**, 1210–1213.

[54] M. B. Abreu, A. C. Reber and S. N. Khanna, *The Journal of Physical Chemistry Letters*, 2014, **5**, 3492–3496.

[55] V. T. Ngan, E. Janssens, P. Claes, J. T. Lyon, A. Fielicke, M. T. Nguyen and P. Lievens, *Chemistry–A European Journal*, 2012, **18**, 15788–15793.

[56] V. Arcisauskaite, D. Fijan, M. Spivak, C. d. Graaf and J. E. McGrady, *Physical Chemistry Chemical Physics*, 2016, **18**, 24006–24014.

[57] R. Ababei, J. Heine, M. Hołyńska, G. Thiele, B. Weinert, X. Xie, F. Weigend and S. Dehnen, *Chemical Communications*, 2012, **48**, 11295–11297.

[58] F. Lips and S. Dehnen, *Angewandte Chemie International Edition*, 2011, **50**, 955–959.

[59] R. J. Wilson, F. Hastreiter, K. Reiter, P. Büschelberger, R. Wolf, R. M. Gschwind, F. Weigend and S. Dehnen, *Angewandte Chemie International Edition*, 2018, **57**, 15359–15363.

[60] E. N. Esenturk, J. C. Fettinger and B. W. Eichhorn, *Journal of the American Chemical Society*, 2006, **128**, 12–13.

[61] B. Kesanli, J. E. Halsig, P. Zavalij, J. C. Fettinger, Y.-F. Lam and B. W. Eichhorn, *Journal of the American Chemical Society*, 2007, **129**, 4567–4574.

[62] J. M. Goicoechea and S. C. Sevov, *Journal of the American Chemical Society*, 2005, **127**, 7676–7677.

[63] X. Li, S. Mitchell, Y. Fang, J. Li, J. Perez-Ramirez and J. Lu, *Nature Reviews Chemistry*, 2023, **7**, 754–767.

[64] K. Yamamoto, T. Imaoka, W.-J. Chun, O. Enoki, H. Katoh, M. Takenaga and A. Sonoi, *Nature Chemistry*, 2009, **1**, 397–402.

[65] B. Qiao, A. Wang, X. Yang, L. F. Allard, Z. Jiang, Y. Cui, J. Liu, J. Li and T. Zhang, *Nature Chemistry*, 2011, **3**, 634–641.

[66] Z. Chen, L. Chen, C. Yang and Q. Jiang, *Journal of Materials Chemistry A*, 2019, **7**, 3492–3515.

[67] L. Liu and A. Corma, *Chemical Reviews*, 2018, **118**, 4981–5079.

[68] J.-C. Liu, X.-L. Ma, Y. Li, Y.-G. Wang, H. Xiao and J. Li, *Nature Communications*, 2018, **9**, 1610.

[69] X.-L. Ma, J.-C. Liu, H. Xiao and J. Li, *Journal of the American Chemical Society*, 2018, **140**, 46–49.

[70] W. E. Kaden, T. Wu, W. A. Kunkel and S. L. Anderson, *Science*, 2009, **326**, 826–829.

[71] K. Judai, S. Abbet, A. S. Wörz, U. Heiz and C. R. Henry, *Journal of the American Chemical Society*, 2004, **126**, 2732–2737.

[72] L. Zhang, R. Si, H. Liu, N. Chen, Q. Wang, K. Adair, Z. Wang, J. Chen, Z. Song, J. Li *et al.*, *Nature Communications*, 2019, **10**, 4936.

[73] H. Yan, Y. Lin, H. Wu, W. Zhang, Z. Sun, H. Cheng, W. Liu, C. Wang, J. Li, X. Huang *et al.*, *Nature Communications*, 2017, **8**, 1070.

[74] H. Qian, M. Zhu, Z. Wu and R. Jin, *Accounts of Chemical Research*, 2012, **45**, 1470–1479.

[75] B. Ni and X. Wang, *Chemical Science*, 2016, **7**, 3978–3991.

[76] J. K. Nørskov, T. Bligaard, J. Rossmeisl and C. H. Christensen, *Nature Chemistry*, 2009, **1**, 37–46.

[77] X. Sun, Y. Gao, C. Zhao, S. Deng, X. Zhong, G. Zhuang, Z. Wei and J.-g. Wang, *Advanced Theory and Simulations*, 2019, **2**, 1800158.

[78] P. Zhou, X. Hou, Y. Chao, W. Yang, W. Zhang, Z. Mu, J. Lai, F. Lv, K. Yang, Y. Liu *et al.*, *Chemical Science*, 2019, **10**, 5898–5905.

[79] F. Li, X. Liu and Z. Chen, *Small Methods*, 2019, **3**, 1800480.

[80] J. Zhu, M. Xiao, D. Ren, R. Gao, X. Liu, Z. Zhang, D. Luo, W. Xing, D. Su, A. Yu *et al.*, *Journal of the American Chemical Society*, 2022, **144**, 9661–9671.

[81] E. Jimenez-Izal and A. N. Alexandrova, *Annual Review of Physical Chemistry*, 2018, **69**, 377–400.

[82] J. Dadras, L. Shen and A. Alexandrova, *The Journal of Physical Chemistry C*, 2015, **119**, 6047–6055.

[83] O. P. Townrow, C. Chung, S. A. Macgregor, A. S. Weller and J. M. Goicoechea, *Journal of the American Chemical Society*, 2020, **142**, 18330–18335.

[84] N. S. Willeit, W. Klein, P. Coburger, E. Fritz-Langhals and T. F. Fässler, *ChemCatChem*, 2024, **16**, e202301200.

[85] B. L. Réant, B. van IJzendoorn, G. F. Whitehead and M. Mehta, *Dalton Transactions*, 2022, **51**, 18329–18336.

[86] B. van IJzendoorn, S. F. Albawardi, I. J. Vitorica-Yrezabal, G. F. Whitehead, J. E. McGrady and M. Mehta, *Journal of the American Chemical Society*, 2022, **144**, 21213–21223.

[87] B. van IJzendoorn, J. B. Whittingham, G. F. Whitehead, N. Kaltsoyannis and M. Mehta, *Dalton Transactions*, 2023, **52**, 13787–13796.

[88] P. Hohenberg and W. Kohn, *Physical Review*, 1964, **136**, B864.

[89] W. Kohn and L. J. Sham, *Physical Review*, 1965, **140**, A1133.

[90] A. D. Becke, *Physical Review A*, 1988, **38**, 3098.

[91] W.-M. Hoe, A. J. Cohen and N. C. Handy, *Chemical Physics Letters*, 2001, **341**, 319–328.

[92] J. P. Perdew, M. Ernzerhof and K. Burke, *The Journal of Chemical Physics*, 1996, **105**, 9982–9985.

[93] C. Adamo and V. Barone, *The Journal of Chemical Physics*, 1999, **110**, 6158–6170.

[94] A. D. Becke, *The Journal of Chemical Physics*, 1993, **98**, 5648–5652.

[95] R. H. Hertwig and W. Koch, *Chemical Physics Letters*, 1997, **268**, 345–351.

[96] J. Heyd, G. E. Scuseria and M. Ernzerhof, *The Journal of Chemical Physics*, 2003, **118**, 8207–8215.

[97] B. Himmetoglu, A. Floris, S. De Gironcoli and M. Cococcioni, *International Journal of Quantum Chemistry*, 2014, **114**, 14–49.

[98] E. R. Ylvisaker, W. E. Pickett and K. Koepernik, *Physical Review B—Condensed Matter and Materials Physics*, 2009, **79**, 035103.

[99] R. Ditchfield, W. J. Hehre and J. A. Pople, *The Journal of Chemical Physics*, 1971, **54**, 724–728.

[100] A. Hellweg and D. Rappoport, *Physical Chemistry Chemical Physics*, 2015, **17**, 1010–1017.

[101] F. Bloch, *Zeitschrift für physik*, 1929, **52**, 555–600.

[102] L. Fernandez Pacios and P. Christiansen, *The Journal of Chemical Physics*, 1985, **82**, 2664–2671.

[103] P. Schwerdtfeger, *ChemPhysChem*, 2011, **12**, 3143–3155.

[104] G. Kresse and D. Joubert, *Physical Review b*, 1999, **59**, 1758.

[105] N. Bohr, *The London, Edinburgh, and Dublin Philosophical Magazine and Journal of Science*, 1913, **26**, 1–25.

[106] G. N. Lewis, *Journal of the American Chemical Society*, 1916, **38**, 762–785.

[107] J. Zhao, Q. Du, S. Zhou and V. Kumar, *Chemical Reviews*, 2020, **120**, 9021–9163.

[108] B. Weinert and S. Dehnen, *Clusters–Contemporary Insight in Structure and Bonding*, 2017, 99–134.

[109] B. Oelkers, M. V. Butovskii and R. Kempe, *Chemistry–A European Journal*, 2012, **18**, 13566–13579.

[110] N. Lichtenberger, R. J. Wilson, A. R. Eulenstein, W. Massa, R. Clérac, F. Weigend and S. Dehnen, *Journal of the American Chemical Society*, 2016, **138**, 9033–9036.

[111] X. Min, I. A. Popov, F.-X. Pan, L.-J. Li, E. Matito, Z.-M. Sun, L.-S. Wang and A. I. Boldyrev, *Angewandte Chemie International Edition*, 2016, **55**, 5531–5535.

[112] L. A. O. P. Braunstein and P. R. Raithby, in *Metal Clusters in Chemistry*, Wiley-VCH, 1999.

[113] C. Dong, Y. Li, D. Cheng, M. Zhang, J. Liu, Y.-G. Wang, D. Xiao and D. Ma, *ACS Catalysis*, 2020, **10**, 11011–11045.

[114] X. Jin and J. E. McGrady, *Advanced Inorganic Chemistry*, 2019, **73**, 265–304.

[115] K. Mayer, J. Weßing, T. F. Fässler and R. A. Fischer, *Angewandte Chemie International Edition*, 2018, **57**, 14372–14393.

[116] R. J. Wilson, N. Lichtenberger, B. Weinert and S. Dehnen, *Chemical Reviews*, 2019, **119**, 8506–8554.

[117] Y. Wang, J. E. McGrady and Z.-M. Sun, *Accounts of Chemical Research*, 2021, **54**, 1506–1516.

[118] J. E. McGrady, F. Weigend and S. Dehnen, *Chem. Soc. Rev.*, 2022, **51**, 628–649.

[119] T. Krämer, J. C. A. Duckworth, M. D. Ingram, B. Zhou, J. E. McGrady and J. M. Goicoechea, *Dalton Transactions*, 2013, **42**, 12120–12129.

[120] B. Zhou, M. S. Denning, D. L. Kays and J. M. Goicoechea, *Journal of the American Chemical Society*, 2009, **131**, 2802–2803.

[121] G. Espinoza-Quintero, J. C. A. Duckworth, W. K. Myers, J. E. McGrady and J. M. Goicoechea, *Journal of the American Chemical Society*, 2014, **136**, 1210–1213.

[122] S. Mitzinger, L. Broeckaert, W. Massa, F. Weigend and S. Dehnen, *Nature Communications*, 2016, **7**, 10480.

[123] G. Te Velde, F. Bickelhaupt, E. Baerends, C. Fonseca Guerra and S. Van Gisbergen, *Journal of Computational Chemistry*, 2001, **22**, 931–967.

[124] J. P. Perdew, K. Burke and M. Ernzerhof, *Physical Review Letters*, 1996, **77**, 3865–3868.

[125] E. van Lenthe, A. Ehlers and E.-J. Baerends, *The Journal of Chemical Physics*, 1999, **110**, 8943–8953.

[126] E. Van Lenthe and E. J. Baerends, *Journal of Computational Chemistry*, 2003, **24**, 1142–1156.

[127] C. C. Pye and T. Ziegler, *Theoretical Chemistry Accounts*, 1999, **101**, 396–408.

[128] L. Qiao, C. Zhang, C.-C. Shu, H. W. Morgan, J. E. McGrady and Z.-M. Sun, *Journal of the American Chemical Society*, 2020, **142**, 13288–13293.

[129] L. Perring, P. Feschotte, F. Bussy and J. Gachon, *J. Alloys and Compounds*, 1996, **245**, 157–163.

[130] W.-X. Chen, N. V. Tkachenko, A. Muñoz-Castro, A. I. Boldyrev and Z.-M. Sun, *Nano Research*, 2022, **15**, 5705–5711.

[131] H.-B. Bürgi and J. D. Dunitz, *Structure correlation*, John Wiley & Sons, 2008.

[132] A. Cetin, O. Esenturk and E. N. Esenturk, *European Journal of Inorganic Chemistry*, 2017, **2017**, 2413–2421.

[133] F. Lips, R. Clérac and S. Dehnen, *Journal of the American Chemical Society*, 2011, **133**, 14168–14171.

[134] V. Khanna, R. Singh, P. Claes, M. T. Nguyen, A. Fielicke, E. Janssens, P. Lievens and J. E. McGrady, *The Journal of Physical Chemistry A*, 2022, **126**, 1617–1626.

[135] H. T. Pham, T.-T. Phan, N. M. Tam, L. V. Duong, M. P. Pham-Ho and M. T. Nguyen, *Physical Chemistry Chemical Physics*, 2015, **17**, 17566–17570.

[136] N. T. Mai, N. T. Tung, P. T. Thuy, N. T. Minh Hue and N. T. Cuong, *Computational and Theoretical Chemistry*, 2017, **1117**, 124–129.

[137] V. T. Tran and Q. T. Tran, *International Journal of Quantum Chemistry*, 2021, **121**, e26619.

[138] X. Li, P. Claes, M. Haertelt, P. Lievens, E. Janssens and A. Fielicke, *Physical Chemistry Chemical Physics*, 2016, **18**, 6291–6300.

[139] S.-J. Lu, L.-R. Hu, X.-L. Xu, H.-G. Xu, H. Chen and W.-J. Zheng, *Physical Chemistry Chemical Physics*, 2016, **18**, 20321–20329.

[140] H. Tsunoyama, H. Akatsuka, M. Shibuta, T. Iwasa, Y. Mizuhata, N. Tokitoh and A. Nakajima, *The Journal of Physical Chemistry C*, 2017, **121**, 20507–20516.

[141] M. Shibuta, T. Niikura, T. Kamoshida, H. Tsunoyama and A. Nakajima, *Physical Chemistry Chemical Physics*, 2018, **20**, 26273–26279.

[142] X.-Q. Liang, X.-J. Deng, S.-J. Lu, X.-M. Huang, J.-J. Zhao, H.-G. Xu, W.-J. Zheng and X. C. Zeng, *The Journal of Physical Chemistry C*, 2017, **121**, 7037–7046.

[143] M. F. Groh, U. Müller, A. Isaeva and M. Ruck, *Zeitschrift für anorganische und allgemeine Chemie*, 2019, **645**, 161–169.

[144] Y. Zhao and D. G. Truhlar, *The Journal of Chemical Physics*, 2006, **125**, 194101.

[145] M. Franchini, P. H. T. Philipsen and L. Visscher, *Journal of Computational Chemistry*, 2013, **34**, 1819–1827.

[146] B. Kesanli, J. Fettinger and B. Eichhorn, *Journal of the American Chemical Society*, 2003, **125**, 7367–7376.

[147] Z. Li, W. Wu and S. Li, *Journal of Molecular Structure: Theochem*, 2009, **908**, 73–78.

[148] H.-G. von Schnering, J. Wolf, D. Weber, R. Ramirez and T. Meyer, *Angewandte Chemie International Edition England*, 1986, **25**, 353–354.

[149] J. M. Goicoechea and J. E. McGrady, *Dalton Transactions*, 2015, **44**, 6755–6766.

[150] O. J. Scherer, *Angewandte Chemie International Edition England*, 1990, **29**, 1104–1122.

[151] R. S. P. Turbervill and J. M. Goicoechea, *Chemical Reviews*, 2014, **114**, 10807–10828.

[152] M. Zhang, W. Wang, Z. Sun, L. Meng and X. Li, *Computational and Theoretical Chemistry*, 2016, **1098**, 50–55.

[153] K. B. Dillon, F. Mathey and J. F. Nixon, *Phosphorus: The Carbon Copy*, Wiley, New York, 1st edn., 1998.

[154] M. C. Simpson and J. D. Protasiewicz, *Pure and Applied Chemistry*, 2013, **85**, 801–815.

[155] C. Heinl, E. Peresypkina, G. Balázs, E. Mädl, A. V. Virovets and M. Scheer, *Chemistry – A European Journal*, 2021, **27**, 7542–7548.

[156] I. Todorov and S. C. Sevov, *Inorganic Chemistry*, 2004, **43**, 6490–6494.

[157] H. G. von Schnering, R. Nesper, J. Curda and K.-F. Tebbe, *Angewandte Chemie International Edition England*, 1980, **19**, 1033–1034.

[158] R. Nesper, J. Curda and H. Von Schnering, *Journal of Solid State Chemistry*, 1986, **62**, 199–206.

[159] U. Frank and W. Müller, *Zeitschrift für Naturforschung B*, 1975, **30**, 313–315.

[160] L. Yong, S. D. Hoffmann, T. F. Fässler, S. Riedel and M. Kaupp, *Angewandte Chemie International Edition England*, 2005, **44**, 2092–2096.

[161] Y. Gholiee, S. Salehzadeh and S. Khodaveisi, *New Journal of Chemistry*, 2019, **43**, 7797–7805.

[162] F. Neese, *Wiley Interdisciplinary Reviews: Computational Molecular Science*, 2012, **2**, 73–78.

[163] F. Neese, *Wiley Interdisciplinary Reviews: Computational Molecular Science*, 2018, **8**, e1327.

[164] Y. Zhao and D. G. Truhlar, *Theoretical Chemistry Accounts*, 2008, **120**, 215–241.

[165] S. Grimme, *The Journal of Chemical Physics*, 2006, **124**, 034108.

[166] F. Neese, T. Schwabe and S. Grimme, *The Journal of Chemical Physics*, 2007, **126**, 124115.

[167] E. van Lenthe, E.-J. Baerends and J. G. Snijders, *The Journal of Chemical Physics*, 1993, **99**, 4597–4610.

[168] F. Weigend and R. Ahlrichs, *Physical Chemistry Chemical Physics*, 2005, **7**, 3297–3305.

[169] J. D. Rolfes, F. Neese and D. A. Pantazis, *Journal of Computational Chemistry*, 2020, **41**, 1842–1849.

[170] D. A. Pantazis and F. Neese, *Theoretical Chemistry Accounts*, 2012, **131**, 1–7.

[171] F. Weigend, *Physical Chemistry Chemical Physics*, 2006, **8**, 1057–1065.

[172] A. Klamt and G. Schüürmann, *Perkin Transactions 2*, 1993, 799–805.

[173] J. Andzelm, C. Kölmel and A. Klamt, *The Journal of Chemical Physics*, 1995, **103**, 9312–9320.

[174] V. Barone and M. Cossi, *The Journal of Physical Chemistry A*, 1998, **102**, 1995–2001.

[175] M. Cossi, N. Rega, G. Scalmani and V. Barone, *Journal of Computational Chemistry*, 2003, **24**, 669–681.

[176] T. Lu and F. Chen, *Journal of Computational Chemistry*, 2012, **33**, 580–592.

[177] C. Zhang, H. W. Morgan, Z.-C. Wang, C. Liu, Z.-M. Sun and J. E. McGrady, *Dalton Transactions*, 2019, **48**, 15888–15895.

[178] J. M. López-Plá, M. Obies, G. Zahariou, M. Pissas, Y. Sanakis, J. E. McGrady and R. G. Raptis, *Chemical Communications*, 2024, **60**, 14117–14120.

[179] L. B. Handy, J. K. Ruff and L. F. Dahl, *Journal of the American Chemical Society*, 1970, **92**, 7312–7326.

[180] J. C. Green, M. L. H. Green and G. Parkin, *Chemical Communications*, 2012, **48**, 11481–11503.

[181] J. A. Labinger, *Inorganica Chimica Acta*, 2015, **424**, 14–19.

[182] J. E. McGrady, *Molecular Metal-Metal Bonds: Compounds, Synthesis, Properties*, Wiley, New York, 1999.

[183] M. Spivak, V. Arcisauskaite, X. López, J. E. McGrady and C. de Graaf, *Dalton Transactions*, 2017, **46**, 6202–6211.

[184] N. Lichtenberger, Y. J. Franzke, W. Massa, F. Weigend and S. Dehnen, *Chemistry–A European Journal*, 2018, **24**, 12022–12030.

[185] S. Kaskel and J. D. Corbett, *Inorganic Chemistry*, 2000, **39**, 778–782.

[186] L. Y. Goh, R. C. S. Wong, C. K. Chu and T. W. Hambley, *Dalton Transactions*, 1990, 977–982.

[187] O. J. Scherer, J. Schwalb, G. Wolmershäuser, W. Kaim and R. Gross, *Angewandte Chemie International Edition England*, 1986, **25**, 363–364.

[188] W. Tremel, R. Hoffmann and M. Kertesz, *Journal of the American Chemical Society*, 1989, **111**, 2030–2039.

[189] C. Lepetit, P. Fau, K. Fajerwerg, M. L. Kahn and B. Silvi, *Coordination Chemistry Reviews*, 2017, **345**, 150–181.

[190] P. Macchi, D. M. Proserpio and A. Sironi, *Journal of the American Chemical Society*, 1998, **120**, 13429–13435.

[191] A. K. Ganguli, A. M. Guloy, E. A. Leon-Escamilla and J. D. Corbett, *Inorganic Chemistry*, 1993, **32**, 4349–4353.

[192] C. Ratnasamy and J. P. Wagner, *Catalysis Reviews*, 2009, **51**, 325–440.

[193] T. Montini, M. Melchionna, M. Monai and P. Fornasiero, *Chemical Reviews*, 2016, **116**, 5987–6041.

[194] C. Rhodes, G. Hutchings and A. Ward, *Catalysis Today*, 1995, **23**, 43–58.

[195] M. Maroño, E. Ruiz, J. Sánchez, C. Martos, J. Dufour and A. Ruiz, *International Journal of Hydrogen Energy*, 2009, **34**, 8921–8928.

[196] C. Rhodes, B. P. Williams, F. King and G. J. Hutchings, *Catalysis Communications*, 2002, **3**, 381–384.

[197] H. Topsøe, J. Dumesic and M. Boudart, *Journal of Catalysis*, 1973, **28**, 477–488.

[198] C. Rhodes, B. P. Williams, F. King and G. J. Hutchings, *Catalysis Communications*, 2002, **3**, 381–384.

[199] C. R. Lund and J. Dumesic, *Journal of Catalysis*, 1982, **76**, 93–100.

[200] Y. Lei, N. W. Cant and D. L. Trimm, *Journal of Catalysis*, 2006, **239**, 227–236.

[201] L. Zhang, X. Wang, J.-M. M. Millet, P. H. Matter and U. S. Ozkan, *Applied Catalysis A: General*, 2008, **351**, 1–8.

[202] T. Popa, G. Xu, T. F. Barton and M. D. Argyle, *Applied Catalysis A: General*, 2010, **379**, 15–23.

[203] D. S. Newsome, *Catalysis Reviews Science and Engineering*, 1980, **21**, 275–318.

[204] C. Callaghan, I. Fishtik, R. Datta, M. Carpenter, M. Chmielewski and A. Lugo, *Surface Science*, 2003, **541**, 21–30.

[205] D. C. Yeragi, N. C. Pradhan and A. K. Dalai, *Catalysis Letters*, 2006, **112**, 139–148.

[206] S. S. Maluf, P. A. d. P. Nascente, C. Afonso and E. M. Assaf, *Applied Catalysis A: General*, 2012, **413**, 85–93.

[207] R. Taha, D. Duprez, N. Mouaddib-Moral and C. Gauthier, *Studies in Surface Science and Catalysis*, 1998, **116**, 549–558.

[208] J. Paier, C. Penschke and J. Sauer, *Chemical Reviews*, 2013, **113**, 3949–3985.

[209] M. V. Ganduglia-Pirovano, J. L. Da Silva and J. Sauer, *Physical Review Letters*, 2009, **102**, 026101.

[210] H.-Y. Li, H.-F. Wang, X.-Q. Gong, Y.-L. Guo, Y. Guo, G. Lu and P. Hu, *Physical Review B—Condensed Matter and Materials Physics*, 2009, **79**, 193401.

[211] J. Kašpar, P. Fornasiero and N. Hickey, *Catalysis Today*, 2003, **77**, 419–449.

[212] M. Shelef and R. W. McCabe, *Catalysis Today*, 2000, **62**, 35–50.

[213] A. Bueno-López, *Applied Catalysis B: Environmental*, 2014, **146**, 1–11.

[214] S. Scirè and L. F. Liotta, *Applied Catalysis B: Environmental*, 2012, **125**, 222–246.

[215] C. Dong, X. Zong, W. Jiang, L. Niu, Z. Liu, D. Qu, X. Wang and Z. Sun, *Small Structures*, 2021, **2**, 2000081.

[216] M. Haruta, T. Kobayashi, H. Sano and N. Yamada, *Chemistry Letters*, 1987, **16**, 405–408.

[217] M. Valden, X. Lai and D. Goodman, *Science*, 1998, **281**, 1647–1650.

[218] Q. Fu, H. Saltsburg and M. Flytzani-Stephanopoulos, *Science*, 2003, **301**, 935–938.

[219] Z.-P. Liu, S. J. Jenkins and D. A. King, *Physical Review Letters*, 2005, **94**, 196102.

[220] C. Zhang, A. Michaelides and S. J. Jenkins, *Physical Chemistry Chemical Physics*, 2011, **13**, 22–33.

[221] H. Y. Kim, H. M. Lee and G. Henkelman, *Journal of the American Chemical Society*, 2012, **134**, 1560–1570.

[222] J. A. Rodriguez, S. Ma, P. Liu, J. Hrbek, J. Evans and M. Perez, *Science*, 2007, **318**, 1757–1760.

[223] H. Y. Kim and G. Henkelman, *The Journal of Physical Chemistry Letters*, 2012, **3**, 2194–2199.

[224] A. Bruix, K. M. Neyman and F. Illas, *The Journal of Physical Chemistry C*, 2010, **114**, 14202–14207.

[225] C. Xu, Y. Wu, S. Li, J. Zhou, J. Chen, M. Jiang, H. Zhao and G. Qin, *Journal of Materials Science & Technology*, 2020, **40**, 39–46.

[226] G. N. Vayssilov, Y. Lykhach, A. Migani, T. Staudt, G. P. Petrova, N. Tsud, T. Skála, A. Bruix, F. Illas, K. C. Prince *et al.*, *Nature Materials*, 2011, **10**, 310–315.

[227] A. Bruix, A. Migani, G. N. Vayssilov, K. M. Neyman, J. Libuda and F. Illas, *Physical Chemistry Chemical Physics*, 2011, **13**, 11384–11392.

[228] J. Vecchietti, A. Bonivardi, W. Xu, D. Stacchiola, J. J. Delgado, M. Calatayud and S. E. Collins, *ACS Catalysis*, 2014, **4**, 2088–2096.

[229] M. Cargnello, T. Montini, S. Polizzi, N. L. Wieder, R. J. Gorte, M. Graziani and P. Fornasiero, *Dalton Transactions*, 2010, **39**, 2122–2127.

[230] Z. Yang, Z. Lu, G. Luo and K. Hermansson, *Physics Letters A*, 2007, **369**, 132–139.

[231] T. Bunluesin, R. Gorte and G. Graham, *Applied Catalysis B: Environmental*, 1998, **15**, 107–114.

[232] F. Wang, L. Zhang, J. Zhu, B. Han, L. Zhao, H. Yu, Z. Deng and W. Shi, *Applied Catalysis A: General*, 2018, **564**, 226–233.

[233] J. Ashok, S. Pati, P. Hongmanorom, Z. Tianxi, C. Junmei and S. Kawi, *Catalysis Today*, 2020, **356**, 471–489.

[234] H.-L. Chen, W.-T. Peng, J.-J. Ho and H.-M. Hsieh, *Chemical Physics*, 2008, **348**, 161–168.

[235] Y.-Q. Su, G.-J. Xia, Y. Qin, S. Ding and Y.-G. Wang, *Chemical Science*, 2021, **12**, 8260–8267.

[236] Y. Li, Q. Fu and M. Flytzani-Stephanopoulos, *Applied Catalysis B: Environmental*, 2000, **27**, 179–191.

[237] S. Chang, M. Li, Q. Hua, L. Zhang, Y. Ma, B. Ye and W. Huang, *Journal of Catalysis*, 2012, **293**, 195–204.

[238] O. Thinon, F. Diehl, P. Avenier and Y. Schuurman, *Catalysis Today*, 2008, **137**, 29–35.

[239] G. A. Somorjai and Y. Li, *Introduction to Surface Chemistry and Catalysis*, John Wiley & Sons, 2010.

[240] Y. Park, S. K. Kim, D. Pradhan and Y. Sohn, *Chemical Engineering Journal*, 2014, **250**, 25–34.

[241] F. F. Tao, *Chemical Society Reviews*, 2012, **41**, 7977–7979.

[242] R. Mu, Q. Fu, H. Xu, H. Zhang, Y. Huang, Z. Jiang, S. Zhang, D. Tan and X. Bao, *Journal of the American Chemical Society*, 2011, **133**, 1978–1986.

[243] B. Liu, Z. Zhao, G. Henkelman and W. Song, *The Journal of Physical Chemistry C*, 2016, **120**, 5557–5564.

[244] W. Xu, R. Si, S. D. Senanayake, J. Llorca, H. Idriss, D. Stacchiola, J. C. Hanson and J. A. Rodriguez, *Journal of Catalysis*, 2012, **291**, 117–126.

[245] T. Utaka, T. Okanishi, T. Takeguchi, R. Kikuchi and K. Eguchi, *Applied Catalysis A: General*, 2003, **245**, 343–351.

[246] G. Kresse and J. Furthmüller, *Physical Review B*, 1996, **54**, 11169.

[247] G. Kresse and J. Furthmüller, *Computational Materials Science*, 1996, **6**, 15–50.

[248] P. E. Blöchl, *Physical Review B*, 1994, **50**, 17953.

[249] S. L. Dudarev, G. A. Botton, S. Y. Savrasov, C. Humphreys and A. P. Sutton, *Physical Review B*, 1998, **57**, 1505.

[250] M. Nolan, S. C. Parker and G. W. Watson, *Physical Chemistry Chemical Physics*, 2006, **8**, 216–218.

[251] Z. Yang, G. Luo, Z. Lu and K. Hermansson, *The Journal of Chemical Physics*, 2007, **127**, 074704.

[252] Y. Zhao, B. Teng, Z. Yang, Y. Zhao, L. Zhao and M. Luo, *The Journal of Physical Chemistry C*, 2011, **115**, 16461–16466.

[253] F. Hussain, M. Imran, A. M. Rana, R. A. Khalil, E. A. Khera, S. Kiran, M. A. Javid, M. A. Sattar and M. Ismail, *Applied Nanoscience*, 2018, **8**, 839–851.

[254] W. Song, Y. Su and E. J. Hensen, *The Journal of Physical Chemistry C*, 2015, **119**, 27505–27511.

[255] W. Luo, Y. Chen, Z. Du and C. Chen, *The Journal of Physical Chemistry C*, 2018, **122**, 28868–28883.

[256] G. Henkelman and H. Jónsson, *The Journal of Chemical Physics*, 2000, **113**, 9978–9985.

[257] G. Henkelman, B. P. Uberuaga and H. Jónsson, *The Journal of Chemical Physics*, 2000, **113**, 9901–9904.

[258] P. Luches, F. Pagliuca, S. Valeri, F. Illas, G. Preda and G. Pacchioni, *The Journal of Physical Chemistry C*, 2012, **116**, 1122–1132.

[259] L. Chen, I. A. Filot and E. J. Hensen, *ACS Catalysis*, 2023, **13**, 15230–15247.

[260] Z. Yang, Z. Lu and G. Luo, *Physical Review B—Condensed Matter and Materials Physics*, 2007, **76**, 075421.

[261] M. Zhu and I. E. Wachs, *ACS Catalysis*, 2016, **6**, 722–732.

[262] C. Ratnasamy and J. P. Wagner, *Catalysis Reviews*, 2009, **51**, 325–440.

[263] Y.-Y. Chen, M. Dong, J. Wang and H. Jiao, *The Journal of Physical Chemistry C*, 2010, **114**, 16669–16676.

[264] D. S. Newsome, *Catalysis Reviews Science and Engineering*, 1980, **21**, 275–318.

[265] M. Tinkle and J. Dumesic, *Journal of Catalysis*, 1987, **103**, 65–78.

[266] J. Nakamura, J. M. Campbell and C. T. Campbell, *Journal of the Chemical Society, Faraday Transactions*, 1990, **86**, 2725–2734.

[267] K. Sun, M. Kohyama, S. Tanaka and S. Takeda, *The Journal of Physical Chemistry C*, 2017, **121**, 12178–12187.

[268] P. Mars and D. W. Van Krevelen, *Chemical Engineering Science*, 1954, **3**, 41–59.

[269] E. F. Armstrong and T. P. Hilditch, *Proceedings of the Royal Society of London. Series A, Containing Papers of a Mathematical and Physical Character*, 1920, **97**, 265–273.

[270] T. Shido and Y. Iwasawa, *Journal of Catalysis*, 1993, **141**, 71–81.

[271] A. A. Gokhale, J. A. Dumesic and M. Mavrikakis, *Journal of the American Chemical Society*, 2008, **130**, 1402–1414.

[272] T.-Y. Shen, P. Yin, Y.-J. Lai, J.-M. Xu, J.-Y. Guo, W. Zhang, M. Pu, H. Yan and M. Wei, *International Journal of Hydrogen Energy*, 2023, **48**, 24951–24960.

[273] L. C. Grabow, A. A. Gokhale, S. T. Evans, J. A. Dumesic and M. Mavrikakis, *The Journal of Physical Chemistry C*, 2008, **112**, 4608–4617.

[274] J. Rodriguez, P. Liu, X. Wang, W. Wen, J. Hanson, J. Hrbek, M. Pérez and J. Evans, *Catalysis Today*, 2009, **143**, 45–50.

[275] A. Chutia, A. Thetford, M. Stamatakis and C. R. A. Catlow, *Physical Chemistry Chemical Physics*, 2020, **22**, 3620–3632.

[276] L. Chen, I. A. Filot and E. J. Hensen, *The Journal of Physical Chemistry C*, 2023, **127**, 20314–20324.

[277] W. L. Vrijburg, E. Moioli, W. Chen, M. Zhang, B. J. Terlingen, B. Zijlstra, I. A. Filot, A. Zuttel, E. A. Pidko and E. J. Hensen, *ACS Catalysis*, 2019, **9**, 7823–7839.

[278] S. Rönsch, J. Schneider, S. Matthischke, M. Schlüter, M. Götz, J. Lefebvre, P. Prabhakaran and S. Bajohr, *Fuel*, 2016, **166**, 276–296.

[279] A. Hatta, A. Jalil, N. Hassan, M. Hamid, M. Bahari, M. Aziz, M. Alhassan, N. Ibrahim, N. Jusoh and N. Hairom, *Materials Today Chemistry*, 2023, **33**, 101743.

[280] A. Hatta, A. Jalil, N. Hassan, M. Hamid, A. Rahman, L. Teh and D. Prasetyoko, *International Journal of Hydrogen Energy*, 2022, **47**, 30981–31002.

[281] I. Fechete, *Comptes Rendus Chimie*, 2016, **19**, 1374–1381.

[282] F. Fischer, H. Tropsch and P. Dilthey, *Brennst. Chem*, 1925, **6**, 265–271.

[283] M. Vannice, *Catalysis Reviews—Science and Engineering*, 1976, **14**, 153–191.

[284] G. A. Mills and F. W. Steffgen, *Catalysis Reviews*, 1974, **8**, 159–210.

[285] G. P. Van Der Laan and A. Beenackers, *Catalysis Reviews*, 1999, **41**, 255–318.

[286] M. Andersson, F. Abild-Pedersen, I. Remediakis, T. Bligaard, G. Jones, J. Engbæk, O. Lytken, S. Horch, J. H. Nielsen, J. Sehested *et al.*, *Journal of Catalysis*, 2008, **255**, 6–19.

[287] B. Miao, S. S. K. Ma, X. Wang, H. Su and S. H. Chan, *Catalysis Science & Technology*, 2016, **6**, 4048–4058.

[288] K. Werner, X. Weng, F. Calaza, M. Sterrer, T. Kropp, J. Paier, J. Sauer, M. Wilde, K. Fukutani, S. Shaikhutdinov *et al.*, *Journal of the American Chemical Society*, 2017, **139**, 17608–17616.

[289] O. Matz and M. Calatayud, *ACS Omega*, 2018, **3**, 16063–16073.

[290] S. Eckle, H.-G. Anfang and R. J. Behm, *The Journal of Physical Chemistry C*, 2011, **115**, 1361–1367.

[291] C. Zhi, Q. Wang, B. Wang, D. Li and R. Zhang, *RSC Advances*, 2015, **5**, 66742–66756.